

Extended PAM in the context of SmB_6
& Cold Atoms in optical lattices:
a DMFT/DCA + NRG study

Master thesis

Frederik Pfeiffer



Faculty of Physics

Chair of Theoretical Solid State Physics

Ludwig-Maximilians-Universität München

Supervisors:

Prof. Dr. Jan von Delft

Dr. Seung-Sup Lee

Munich, April 2021

Erweitertes PAM im Kontext von SmB_6 & Kalte Atome in optischen Gittern: eine DMFT/DCA + NRG Studie

Masterarbeit

Frederik Pfeiffer



Fakultät für Physik

Lehrstuhl für Theoretische Festkörperphysik

Ludwig-Maximilians-Universität München

Betreuer:

Prof. Dr. Jan von Delft

Dr. Seung-Sup Lee

München, April 2021

Abstract:

Experimentally, the Hamiltonian of a fermionic two-band model can be realized by a cold gas of fermionic Yb^{173} atoms trapped in state-dependent optical lattices. For experimental parameters provided by the Quantum Optics Group at LMU lead by Simon Fölling, we perform DMFT calculations with NRG as impurity solver. We find that the repulsive interaction between the two different atomic states leads to phases in which lattice sites are occupied exclusively by one of the atomic species.

Motivated by the proposal of the existence of a neutral Fermi surface in the mixed-valence compound SmB_6 , we study the extended periodic Anderson model (PAM) in the mixed-valence regime with DMFT and its cluster extension DCA, using NRG as impurity solver. We find a band insulator renormalized by interactions, which we tune between a metallic and insulating state. DCA calculations do not show signs of nonlocal correlations in the mixed-valence regime. Moreover, no evidence for the formation of a neutral Fermi surface is found. Furthermore, we calculate the temperature-dependent optical conductivity and resistivity, which show agreement with experimental data on SmB_6 .

Contents

1	Introduction	1
2	Dynamical mean-field theory (DMFT)	2
2.1	Definitions and Notation	2
2.2	The limit of infinite dimensions	4
2.3	Self-consistency and iteration scheme	6
3	Cluster extensions	9
3.1	Cellular DMFT (CDMFT)	10
3.2	Dynamical cluster approximation (DCA)	11
4	Numerical renormalization group (NRG)	14
4.1	Impurity models	14
4.2	Logarithmic discretization and discretized Hamiltonian	14
4.3	Iterative Diagonalization	15
4.4	Useful extensions	17
5	Cold atoms, a DMFT analysis	18
5.1	Method	19
5.2	Influence of repulsive interaction V	20
5.3	Local energy levels	23
5.4	Experimental parameter sets	24
6	Extended periodic Anderson model in the context of Samarium-Hexaboride	28
6.1	Non-interacting band structure	30
6.2	DMFT	31
6.2.1	Method	31
6.2.2	Mixed-valence regime, $U_{df} = 0$	34
6.2.3	Influence of the interaction U_{df}	35
6.2.4	Metal-insulator transition and dynamical susceptibilities	38
6.2.5	Transport properties	42
6.3	DCA	45
6.3.1	Method	45
6.3.2	Mixed-valence regime, $D_f = 0$	48
6.3.3	Mixed-valence regime, $U_{df} = 0$	49
6.3.4	Away from the mixed-valence regime	51
6.4	Conclusion	52
7	References	54

1 Introduction

Strongly correlated materials, in which electron-electron interactions are comparable to kinetic energy, show fascinating properties, e.g. high- T_c superconductivity or anomalies in thermodynamic quantities. A theoretical description is challenging, since the single-particle picture tends to fail, in the presence of strong interactions, and a many-body treatment is necessary. Many-body systems are in general not exactly solvable with a classical computer as the dimension of the Hilbert space grows exponentially with the number of constituents. Nevertheless, non-perturbative methods have been developed, which can tackle the many-body problem and provide controlled approximation schemes. In this thesis, we use the well-established Dynamical mean-field theory (DMFT) [1] and its cluster extension, the Dynamical cluster approximation (DCA) [2], to study two different many-body systems. In DMFT a quantum lattice model is mapped self-consistently on a quantum impurity model, which can be solved accurately. In our case, the numerical renormalization group (NRG) [3], a powerful real-frequency impurity solver, is used. The state of the art NRG code available in the group of Prof. Jan von Delft was developed by Andreas Weichselbaum and Seung-Sup Lee.

In the beginning, a short introduction to the core ideas of DMFT, DCA, and NRG is given. Subsequently, we present the analysis of two different many-body systems.

First of all, we study a system of Cold atoms trapped in optical lattices. Cold atoms offer a promising platform to study many-body quantum effects experimentally [4] and can be designed to mimic the Hamiltonian of a quantum lattice model. Recent experimental progress makes it possible to realize the Hamiltonian of a fermionic two-band model. Nelson Darkwah Oppong from the Quantum Optics group at LMU provided us with the Hamiltonian and parameters corresponding to their experimental setup. We perform DMFT calculations for different experimental parameter sets to possibly guide experimentalists to favorable parameter choices.

In the second part of this thesis, we study the periodic Anderson model (PAM) and possible extensions in the context of the mixed-valence compound Samarium-Hexaboride (SmB_6). SmB_6 shows controversial experimental signatures. On the one hand, an increasing resistivity with decreasing temperature indicates insulating behavior. On the other hand, experiments reveal quantum oscillations comparable to metallic LaB_6 . Chowdhury et. al, propose a mechanism for the formation of a neutral Fermi surface in the framework of the extended PAM to resolve the puzzling experimental situation [5]. We study the extended PAM with DMFT and DCA to look for signatures of the proposed mechanism and the general relevance of the extended PAM for experimental measurements on SmB_6 .

2 Dynamical mean-field theory (DMFT)

Dynamical mean-field theory (DMFT), originally derived by W. Metzner and D. Vollhardt in 1989 [6], has proven to be a valuable tool to investigate strongly interacting quantum lattice models in a non-perturbative fashion. While being exact in the limit of infinite dimensions, DMFT can be used as an approximation scheme in general dimensions. In infinite dimensions, the self-energy becomes purely local, which lays the foundation for a self-consistent mapping between a quantum lattice model and local theory, i.e. a quantum impurity model.

The Hubbard model in infinite dimensions is considered to derive the local nature of the self-energy from a diagrammatic perspective. Furthermore, the origin of the self-consistency equation and an iteration scheme to solve are presented.

2.1 Definitions and Notation

Before starting with the derivation of the DMFT equations, basic notation and definition of Green's function and self-energy are given. Moreover, the concept of the Luttinger-Ward functional is introduced, which is useful to show the consistency of the DMFT approximation. For more details, see standard textbooks e.g. [7].

Hubbard model

For demonstration purposes, the historical choice, the Hubbard model, is used. Later we will see that the DMFT equations easily translate to other lattice models. The Hamiltonian of the Hubbard model is given by:

$$\begin{aligned} H &= \sum_{\langle i,j \rangle} t_{ij} (c_{i,\sigma}^\dagger c_{j,\sigma} + h.c.) + U \sum_i n_{i,\uparrow} n_{i,\downarrow} \\ &= \sum_{k,\sigma} \epsilon_k c_{k,\sigma}^\dagger c_{k,\sigma} + U \sum_{k_1,k_2,q} c_{k_1+q,\sigma}^\dagger c_{k_2+q,\bar{\sigma}}^\dagger c_{k_2,\bar{\sigma}} c_{k_1,\sigma}. \end{aligned} \quad (2.1)$$

The fermionic operators $c_{k,\sigma}, c_{k,\sigma}^\dagger$ fulfill anti-commutation relations, $\{c_{k,\sigma}, c_{k',\sigma'}^\dagger\} = \delta_{k,k'} \delta_{\sigma,\sigma'}$. Electrons are itinerant, described by the nearest-neighbour hopping t_{ij} or the dispersion ϵ_k , and interact via the on-site interaction U .

Green's function and self-energy

For finite temperatures, the Green's function is usually formulated in imaginary time because of its anti-periodicity (periodicity) in $\beta = \frac{1}{k_B T}$ for fermions (bosons). The time and frequency representations read:

$$G_{ij}(\tau) = - \langle \mathcal{T} c_{i,\sigma}(\tau) c_{j,\sigma}^\dagger(0) \rangle, \quad (2.2)$$

$$G_{ij}(i\omega_n) = \int_0^\beta d\tau G_{ij}(\tau) e^{-i\omega_n \tau}. \quad (2.3)$$

Here $\omega_n = (2n+1)\pi\beta$ with $n \in \mathbb{Z}$ is the fermionic Matsubara frequency. The real-frequency retarded Green's function $G_{ij}^R(\omega + i0^+)$ is obtained by analytic continuation, i.e. by the replacement $i\omega_n \rightarrow \omega + i0^+$. In the following, we will denote it by $G_{ij}(\omega)$, in which the retarded nature and the infinitesimal imaginary part $i0^+$ are implied if not specifically mentioned. The DMFT calculations, done in this

thesis, only involve real-frequency objects, however for the derivation of the DMFT equations we stick to the analytically more convenient imaginary frequency representation of the Green's function. For a translationally invariant system the Green's function can be expressed as:

$$G(k, i\omega_n) = \frac{1}{i\omega_n + \mu - \epsilon_k - \Sigma(k, i\omega_n)} = \frac{1}{G_0(k, i\omega_n) - \Sigma(k, i\omega_n)}. \quad (2.4)$$

Here $G_0(k, i\omega_n)$ is the non-interacting Green's function and $\Sigma(k, i\omega_n)$ the self-energy, which includes all interaction effects. In Fig. 2.1 the self-energy skeleton expansion is sketched, i.e. a diagrammatic expansion of the self-energy using only the full interacting propagator.

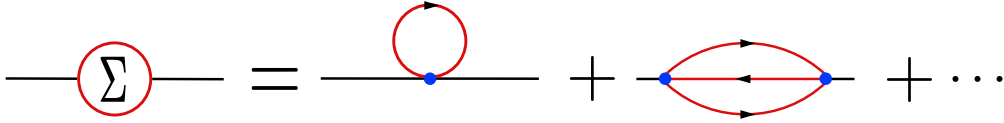


Fig. 2.1: Skeleton expansion of the self-energy. Red lines denote full propagators, blue dots bare vertices.

Luttinger-Ward functional

An exact calculation of $\Sigma(k, i\omega_n)$ is intractable. Within DMFT the self-energy is a central object, which has to be approximated. For the justification of the approximation, it is convenient to use the formalism of the Luttinger-Ward functional $\Phi_U[G]$. A closed-form of the functional does not exist, though it can be diagrammatically represented by the sum over all vacuum skeleton diagrams. The

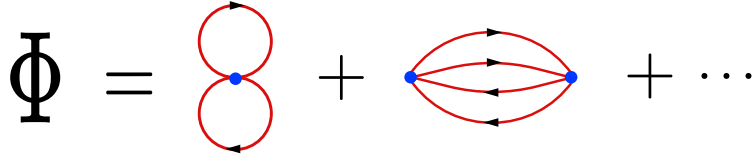


Fig. 2.2: Skeleton expansion of the Luttinger-Ward functional. Red lines denote full propagators, blue dots bare vertices.

self-energy can be derived from the Luttinger-Ward functional by taking the functional derivative in respect to the Green's function,

$$\Sigma(k, i\omega_n) = \frac{\delta \Phi_U[G(k, i\omega_n)]}{\delta G(k, i\omega_n)}. \quad (2.5)$$

Intuitively this can be seen by comparing the diagrammatic expansion of the self-energy with the diagrams involved in the LW-functional, as the functional derivative in respect to the Green's function stands for cutting one propagator line in the vacuum diagrams. The LW-functional is of importance since any approximation scheme involving a self-energy which can be derived from the LW-functional is thermodynamically consistent ([8],[9]).

2.2 The limit of infinite dimensions

The goal is to show that the self-energy becomes purely local in the limit of infinite dimension. As a starting point, the effect of the limit $d \rightarrow \infty$ on the Hubbard model, given by Hamiltonian in Eq. (2.1), is considered.[6]

Hubbard model in infinite dimensions

To perform the limit $d \rightarrow \infty$, the hopping amplitude t_{ij} must be rescaled to prevent diverging kinetic energy. The interaction term remains unaffected. The kinetic energy is finite as long as the non-interacting density of states (DOS)

$$D(\epsilon) = \int_{\vec{k}} d\vec{k} \delta(\epsilon - \epsilon_{\vec{k}}) \quad (2.6)$$

is independent of d . By rescaling $t_{ij} = \frac{t}{\sqrt{2d}}$ and using the central limit theorem it can be shown that $D(\epsilon)$ is a gaussian (see [1], p.113-115)

$$D(\epsilon) = \frac{1}{\sqrt{2\pi t^2}} e^{-\epsilon^2/2t^2}, \quad (2.7)$$

which is indeed independent of d . The scaling of the hopping amplitude has an important impact on diagrammatic expressions because it directly affects the scaling behavior of the Green's function.

Scaling of the Green's function

The Green's function inherits its scaling behavior in d from the rescaled hopping $t_{ij} \propto d^{-1/2}$. From the definition of the Green's function in eq. (2.2) the following scaling can be derived:

$$G_{ij}(\tau) = -\langle \mathcal{T} c_{i,\sigma}(\tau) c_{j,\sigma}^\dagger(0) \rangle \propto \mathcal{O}(d^{-\|i-j\|/2}), \quad (2.8)$$

since the Green's function G_{ij} propagates between the sites i and j , involves at least a factor of $d^{-\|i-j\|/2}$ from the rescaled hopping amplitudes. Here $R_{ij} = \|i-j\| = \sum_b |R_{i,b} - R_{j,b}|$ is the Manhattan distance between the lattice vectors $\vec{R}_{i/j} = \sum_b R_{i/j,b} \cdot \vec{a}_b$, i.e. the metric R_{ij} measures the distance only in discrete steps along the lattice directions given by the bravais lattice basis $\{\vec{a}_b\}$. Consequently, also $G_{ij}(i\omega_n) \propto d^{-R_{ij}/2}$ holds.

Implications on the self-energy

To reveal the effect of the limit $d \rightarrow \infty$ on the self-energy, a second-order diagram shown in Fig. 2.3 is used for illustration, which involves the connection of two internal vertices i and j . Fixing site i , the number of neighbours at distance R_{ij} scales as $d^{R_{ij}}$ for large d . Altogether the connection of the two vertices involves a factor $d^{R_{ij}} \cdot d^{-P_{ij}/2R_{ij}}$, in which P_{ij} is the number of paths by which the vertices are connected. For the second order diagram we have $P_{ij} = 3$, and therefore the diagram is of order $\mathcal{O}(d^{-R_{ij}/2})$, which goes to zero in the limit of $d \rightarrow \infty$ for $i \neq j$.

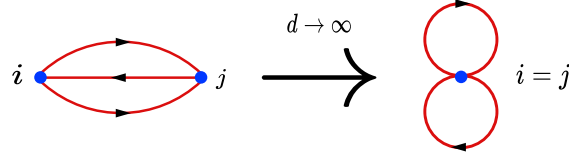


Fig. 2.3: Visualization of the limit $d \rightarrow \infty$. Diagrams connecting two vertices i and j with more than two propagators collapse to local diagrams in the limit $d \rightarrow \infty$, i.e. only contributions with $i = j$ remain non-zero.

In general, all diagrams in which vertices are connected by more than two lines, i.e. $P_{ij} > 2$, vanish in the limit $d \rightarrow \infty$, except for the case $i = j$. This holds for all diagrams involved in a skeleton expansion of self-energy. As a result, the self-energy becomes purely local:

$$\lim_{d \rightarrow \infty} \Sigma_{ij}(i\omega_n) = \Sigma(i\omega_n) \delta_{i,j}, \quad (2.9)$$

$$\lim_{d \rightarrow \infty} \Sigma(k, i\omega_n) = \Sigma(i\omega_n). \quad (2.10)$$

Moreover, as mentioned previously, the self-energy should be derivable from the Luttinger-Ward(LW) functional $\Phi[G_{ij}]$. Analogue to the scaling of the self-energy diagrams in the limit of infinite dimensions, only local diagrams involved in the expansion of the LW functional remain non-zero, s.t. $\lim_{d \rightarrow \infty} \Phi[G_{ij}] = \sum_i \phi[G_{ii}]$. Taking the functional derivative of the LW functional in respect to the Green's function yields the self-energy:

$$\lim_{d \rightarrow \infty} \Sigma_{ij}(i\omega_n) = \frac{\delta \sum_l \phi[G_{ll}(i\omega_n)]}{\delta G_{ij}(i\omega_n)} = \Sigma(i\omega_n) \delta_{i,j}. \quad (2.11)$$

Since the LW functional and the self-energy are local, they should be derivable from a local theory.

Relation to impurity model

The Hubbard model involving only local interactions can be described by a single-site action

$$S = - \int_0^\beta d\tau d\tau' c_\sigma^\dagger(\tau) G_0^{-1}(\tau - \tau') c_\sigma(\tau') + \int_0^\beta d\tau U n_{c,\uparrow} n_{c,\downarrow}. \quad (2.12)$$

An action of the same form can be derived from a quantum impurity model, such as the single Anderson impurity model (SIAM). More details on the model are discussed in section 4.1. Its Hamiltonian reads

$$H = H_{\text{imp}} + H_{\text{bath}} + H_{\text{hyb}} \quad (2.13)$$

$$H_{\text{imp}} = (E_c - \mu) \sum_\sigma c_\sigma^\dagger c_\sigma + U n_{c,\uparrow} n_{c,\downarrow} \quad (2.14)$$

$$H_{\text{bath}} = \sum_{k,\sigma} \epsilon_k a_{k,\sigma}^\dagger a_{k,\sigma} \quad (2.15)$$

$$H_{\text{hyb}} = \sum_{k,\sigma} V_{k,\sigma} (c_\sigma^\dagger a_{k,\sigma} + h.c.). \quad (2.16)$$

The SIAM has a local interacting site coupled to a non-interacting bath, fully described by the hybridization function

$$\Delta(i\omega_n) = \sum_k \frac{V_k^2}{i\omega_n - \epsilon_k}. \quad (2.17)$$

Integrating out the bath yields an action of the same form as the one given in Eq. (2.12), with

$$G_0^{-1}(i\omega_n) = i\omega_n + \mu - \Delta(i\omega_n). \quad (2.18)$$

Therefore in infinite dimension, the problem of solving a quantum lattice model reduces to solving a quantum impurity model, which is still a many-body problem and a difficult task itself. The remaining challenge is to find the hybridization function $\Delta(i\omega_n)$, which is done self-consistently as described in the following section. The relation between lattice and impurity model can also be seen in a similar way classical mean-field theory (MFT) is done. For example in the classical MFT for the Ising model, a lattice model is mapped onto a single-site model with an effective mean-field that fulfills a self-consistency constraint. In the case of the Ising model, the self-consistency condition can be derived from the requirement that the lattice and the single-site model yield the same local magnetization. Similarly, for quantum lattice models like the Hubbard model, the lattice problem is mapped onto an impurity model which involves an interacting impurity site coupled to a bath. In this case, the hybridization function $\Delta(i\omega_n)$, which characterizes the bath, represents the mean-field. In contrast to classical MFT, the mean-field is now a dynamic quantity, which coined the name dynamical mean-field theory (DMFT). In the limit of infinite dimensions, the mapping between lattice and impurity models is exact. For finite dimensions, it can be used to define an approximation scheme to solve the more complicated lattice model.

2.3 Self-consistency and iteration scheme

In this section, we switch to using the real-frequency notation as it is used in the numerical calculations involved in this thesis. Previously, the Hubbard model in infinite dimensions was related to an impurity model, the SIAM, with an effective hybridization $\Delta(\omega)$. The remaining problem is to determine the dynamic mean-field $\Delta(\omega)$ which fulfills a self-consistency equation.

Self consistency equation

The effective impurity model should reproduce the local dynamics of the lattice model. Therefore local quantities calculated from the lattice and impurity model should be identical. In DMFT the central object is the local Green's function. The self-consistency condition, therefore, requires the local lattice Green's function to be equal to the impurity Green's function:

$$G_{\text{latt}}(\omega) \stackrel{!}{=} G_{\text{imp}}(\omega). \quad (2.19)$$

The local lattice Green's function can be calculated via momentum integration

$$G_{\text{latt}}(\omega) = \int dk \frac{1}{G_0(k, \omega) - \Sigma_{\text{latt}}(k, \omega)}. \quad (2.20)$$

Furthermore, the impurity Green's function is given by

$$G_{\text{imp}}(\omega) = \frac{1}{\omega + \mu - \Delta(\omega) - \Sigma_{\text{imp}}(\omega)}. \quad (2.21)$$

Setting $\Sigma_{\text{latt}}(k, \omega) = \Sigma_{\text{imp}}(\omega)$, leads to a self consistency equation for $\Delta(\omega)$:

$$\int dk \frac{1}{G_0(k, \omega) - \Sigma_{\text{imp}}(\omega)} = \frac{1}{\omega + \mu - \Delta(\omega) - \Sigma_{\text{imp}}(\omega)}, \quad (2.22)$$

which can be solved iteratively. In the limit of infinite dimension, the momentum dependent lattice self-energy is local $\Sigma_{\text{latt}}(k, \omega) = \Sigma_{\text{latt}}(\omega)$, i.e. it can be generated from an impurity model and the self-consistency equation gives an exact solution. In general, the momentum dependence of $\Sigma_{\text{latt}}(k, \omega)$ cannot be neglected. However, the solution of the self-consistency equation can be seen as a viable approximation for the lattice problem. In the following an iterations scheme to derive the solution of the self-consistency equation is described, which is visualized in Fig. 2.4.

Iteration scheme

1. Initiate the hybridization function $\Delta(\omega)$, e.g. a constant box shaped hybridization.
2. Given $\Delta(\omega)$, solve the corresponding impurity model with a impurity solver, in our case NRG. This yields the impurity self-energy $\Sigma(\omega)$.
3. Approximate $\Sigma_{\text{latt}}(k, \omega) \approx \Sigma(\omega)$ and calculate the local lattice Green's function via numeric integration or analytically if possible.
4. Extract the new hybridization function from the self consistency equation

$$\Delta_{\text{new}}(\omega) = \omega + \mu - \Sigma(\omega) - G_{\text{latt}}^{-1}(\omega), \quad (2.23)$$

and use it as new input hybridization for the impurity model.

5. Repeat steps 2.) - 4.) until convergence is reached, i.e. until the input hybridization in step 2.) and the output hybridization in step 4.) match up to a desired accuracy.

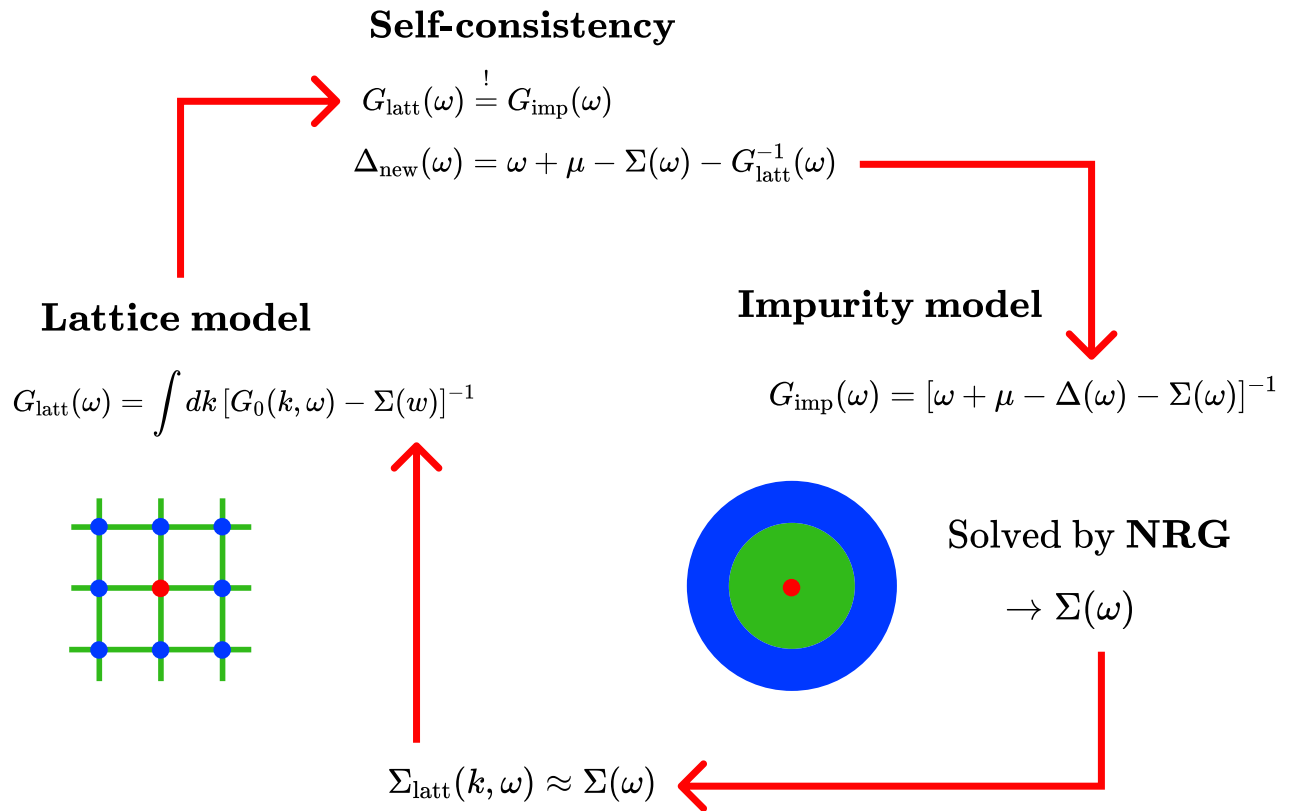


Fig. 2.4: Visualization of the DMFT self-consistency iteration.

3 Cluster extensions

A drawback of standard DMFT is the neglect of momentum dependence of the lattice self-energy. However, there exist extensions, which reintroduce nonlocal correlations. The basic idea is to enlarge the single interacting site of the self-consistent impurity model to a small cluster of interacting sites. Consequently, nonlocal correlations within the cluster can be captured and momentum dependence is introduced into the self-energy. Here the two most established approaches, cellular DMFT (CDMFT) and the dynamical cluster approximation (DCA) are discussed. In this thesis only DCA will be used, however, it is instructive to first introduce CDMFT as it has a lot of similarities with DCA. Firstly, the more intuitive CDMFT is introduced, in which clusterization is performed in real space. Subsequently, a connection to DCA is drawn, which is formulated in momentum space. In this section a rather practical introduction to DMFT cluster extensions is given, focusing on how the self-consistency equation is constructed. The basic concepts presented are inspired by the reviews ([2],[10]), which are recommended for more details and a rigorous derivation. In our calculations, only two-site clusters will be used. Therefore we follow the example of the Hubbard model on a square lattice with clusters containing two sites.

Before going into detail, basic notation for labeling sites and momenta in the clusterized lattice is introduced, see Fig. 3.1. In real space, the lattice is tiled into a superlattice of cells containing N_c sites. The cell position within the superlattice is labeled by \tilde{x} , the position within a cell by X . Similarly, the corresponding momentum space to the cluster site X is labeled by K , while the momenta \tilde{k} labels the superlattice momentum space.

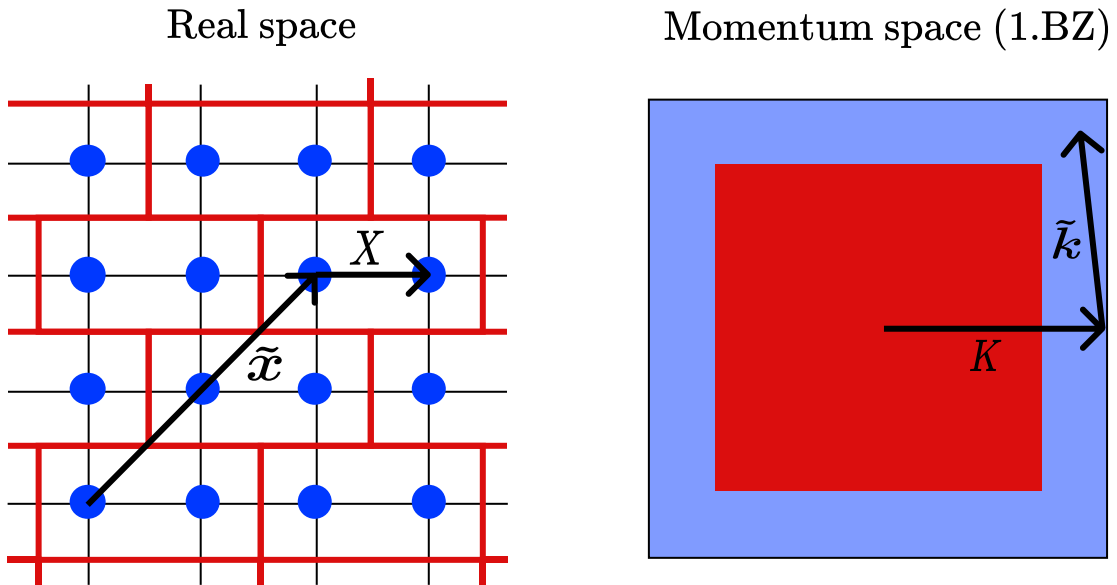


Fig. 3.1: Clusterization of a square lattice into clusters containing $N_c = 2$ sites. The left side shows the tiling of the lattice into a superlattice of two-site clusters in real space. \tilde{x} denotes the position within the superlattice, X the position within the cluster. The right side illustrates the clusterization in momentum space. The first Brillouin zone (1.BZ) is split up into two patches. Each patch corresponds to the momentum space of the cluster site X and is labeled by K . \tilde{k} label the wave vectors of the superlattice.

3.1 Cellular DMFT (CDMFT)

CDMFT is constructed from a real-space perspective. The lattice is tiled into a superlattice of cells containing N_c sites, as illustrated in Fig. 3.1. Whereas translation invariance is retained in the superlattice, it is violated within a cell. Therefore in CDMFT, Green's function and self-energy are formulated as $N_c \times N_c$ matrices in the cluster space (denoted by bold symbols) and can be labeled by the superlattice momenta \tilde{k} :

$$\mathbf{G}(\tilde{k}, \omega) = [\mathbf{G}_0^{-1}(\tilde{k}, \omega) - \mathbf{\Sigma}(\tilde{k}, \omega)]^{-1}, \quad (3.1)$$

$$\mathbf{G}_0(\tilde{k}, \omega) = [(\omega + \mu)\mathbf{1} - \mathbf{t}(\tilde{k})]^{-1}. \quad (3.2)$$

$$(3.3)$$

Here the hopping matrix $\mathbf{t}(\tilde{k})$ can be represented by the intracluster Fourier transformation,

$$t(\tilde{k})_{X_i, X_j} = \frac{1}{N_c} \sum_K \exp(i(\tilde{k} + K)(X_i - X_j)) t(\tilde{k} + K), \quad (3.4)$$

with $t(\tilde{k} + K) = \epsilon_k$ being the dispersion of the lattice. For the example of the two-site cluster, $X_1 = \mathbf{0}$, $X_2 = \mathbf{e}_x$, $K_{i,x} = \frac{2\pi}{L_c} n_i = \pi n_i$ with integer $n_i = 0, 1$, yield

$$\mathbf{t}(\tilde{k}) = \begin{pmatrix} 0 & e^{i\tilde{k}_x \epsilon_{\tilde{k}}} \\ e^{-i\tilde{k}_x \epsilon_{\tilde{k}}} & 0 \end{pmatrix}. \quad (3.5)$$

Here one can clearly see that the factor $e^{i\tilde{k}(X_i - X_j)}$ leads to a violation of translation invariance. Altogether the local lattice Green's function in cluster space is given by

$$\mathbf{G}_{\text{latt}}(\omega) = \int d\tilde{k} [\mathbf{G}_0(\tilde{k}, \omega) - \mathbf{\Sigma}(\tilde{k}, \omega)]^{-1}. \quad (3.6)$$

As in standard DMFT, the self-energy $\mathbf{\Sigma}(\tilde{k}, \omega)$ is intractable to calculate exactly. It has to be approximated by a self-energy, calculated from a self-consistent impurity model. The self-energy of the impurity model is independent of \tilde{k} , preserving correlations within the cluster and neglecting correlations between different clusters, i.e. $\mathbf{\Sigma}(\tilde{k}, \omega) \approx \mathbf{\Sigma}(\omega)$. For a two-site cluster, the corresponding impurity model is the two impurity Anderson model (2IAM). Its Hamiltonian reads

$$H = H_{\text{cl}} + H_{\text{bath}} + H_{\text{hyb}} \quad (3.7)$$

$$H_{\text{cl}} = -t \sum_{\sigma} (c_{1,\sigma}^{\dagger} c_{2,\sigma} + h.c.) + U \sum_{\alpha} n_{\alpha,\uparrow} n_{\alpha,\downarrow} - \mu \sum_{\alpha,\sigma} n_{\alpha,\sigma} \quad (3.8)$$

$$H_{\text{bath}} = \sum_{\alpha,\lambda,\sigma} \epsilon_{\alpha,\lambda} a_{\alpha,\lambda,\sigma}^{\dagger} a_{\alpha,\lambda,\sigma} \quad (3.9)$$

$$H_{\text{hyb}} = \sum_{\alpha,\beta,\lambda,\sigma} (V_{\alpha,\beta,\lambda} c_{\alpha,\sigma}^{\dagger} a_{\beta,\lambda,\sigma} + h.c.), \quad (3.10)$$

with the cluster indices $\alpha, \beta = 1, 2$. The bath parameters are characterized through the hybridization function

$$\Delta_{\alpha, \beta}(\omega) = \sum_{\gamma, \lambda} \frac{V_{\alpha, \gamma, \lambda} \bar{V}_{\beta, \gamma, \lambda}}{\omega - \epsilon_{\gamma, \lambda}}. \quad (3.11)$$

Solving the impurity model yields the self-energy $\Sigma(\omega)$ and the cluster Green's function

$$\mathbf{G}_{\text{cl}}(\omega) = [(\omega + \mu)\mathbf{1} - t \cdot \sigma_x - \mathbf{\Delta}(\omega) - \Sigma(\omega)]^{-1}. \quad (3.12)$$

Identical to standard DMFT the self consistency condition, relating the impurity model to the lattice model, requires the local Green's function of both models to be equal

$$\mathbf{G}_{\text{latt}}(\omega) \stackrel{!}{=} \mathbf{G}_{\text{cl}}(\omega). \quad (3.13)$$

The iteration scheme to find the self-consistent hybridization function is analogous to the one defined in section 2.3, except that now all objects are $N_c \times N_c$ matrices. The new hybridization function in each iteration loop is extracted from the self consistency equation via

$$\mathbf{\Delta}(\omega) = (\omega + \mu)\mathbf{1} - t \cdot \sigma_x - \Sigma(\omega) - \mathbf{G}_{\text{latt}}^{-1}(\omega). \quad (3.14)$$

After a self-consistent solution is found, the obtained self-energy is not diagonal in k -space. To resolve this issue, the self-energy has to be reperiodized ([11],[12],[13]). The reperiodization scheme has to preserve causality, i.e. $\text{Im}[\Sigma(k, \omega)] < 0$. However, there exist different schemes, which introduce some arbitrariness.

3.2 Dynamical cluster approximation (DCA)

Previously we showed the violation of translation invariance in CDMFT manifests in the hopping matrix $\mathbf{t}(\tilde{k})$ through the factor $e^{i\tilde{k}(X_i - X_j)}$ in the intra-cluster Fourier transformation, see Eq. (3.4). In DCA translation invariance is restored by simply dropping this factor. Consequently, the hopping matrix simplifies to

$$\mathbf{t}(\tilde{k}) = \begin{pmatrix} 0 & \epsilon_{\tilde{k}} \\ \epsilon_{\tilde{k}} & 0 \end{pmatrix}, \quad (3.15)$$

for the example of a two-site cluster. In general, this enables us to diagonalize the lattice Green's function by Fourier transforming to K -space:

$$G(\tilde{k}, K, \omega) = \sum_{i, j} \exp(-i(\tilde{k} + K)(X_i - X_j)) G_{X_i, X_j}(\tilde{k}, \omega). \quad (3.16)$$

In contrast to CDMFT, the lattice Green's function is now diagonal in the cluster momentum K by construction. Omitting the factor $e^{i\tilde{k}(X_i - X_j)}$ in the intracluster Fourier transformation can be seen as having a cluster with periodic boundary conditions in real space. Consequently, the case of a two-site

cluster is special, because each cluster site “sees” its neighbor twice. Thus nonlocal correlations are expected to be enhanced in DCA compared to CDMFT for $N_c = 2$.

The local lattice Green’s function for each K_i is defined as

$$G_{\text{latt}}(K_i, \omega) = \int_{\mathcal{P}_i} \frac{dk}{\mathcal{V}_{\mathcal{P}_i}} [G_0(k, \omega) - \Sigma(k, K_i, \omega)]^{-1}, \quad (3.17)$$

with $i = 1 \dots N_c$. Here \mathcal{P}_i denotes a momentum patch in the first Brillouin zone (BZ), which corresponds to the cluster momentum K_i . Thus in DCA the first BZ is split into N_c patches. The right side of Fig. 3.1 visualizes, a possible momentum space patching for $N_c = 2$. However, this introduces some arbitrariness since the shape of the patches can be chosen freely as long as its extent takes up $1/N_c$ of the full BZ.

As in CDMFT, the self-energy has to be approximated by a self-consistent cluster impurity model. In DCA, the Hamiltonian of the impurity model is formulated in momentum space representation:

$$H = H_{\text{cl}} + H_{\text{bath}} + H_{\text{hyb}} \quad (3.18)$$

$$H_{\text{cl}} = \sum_{i, \sigma} (\epsilon_{K_i} - \mu) c_{K_i, \sigma}^\dagger c_{K_i, \sigma} + U \sum_{i, j, l} c_{K_i + Q_l, \sigma}^\dagger c_{K_j + Q_l, \bar{\sigma}}^\dagger c_{K_j, \bar{\sigma}} c_{K_i, \sigma} \quad (3.19)$$

$$H_{\text{bath}} = \sum_{i, \lambda, \sigma} \epsilon_{i, \lambda, \sigma} a_{i, \lambda, \sigma}^\dagger a_{i, \lambda, \sigma} \quad (3.20)$$

$$H_{\text{hyb}} = \sum_{i, \lambda} V_{i, \lambda} (c_{K_i, \sigma}^\dagger a_{i, \lambda, \sigma} + h.c.) \quad (3.21)$$

$$\epsilon_{K_i} = \frac{1}{\mathcal{V}(\mathcal{P}_i)} \sum_k \chi_{\mathcal{P}_i}(k) \epsilon_k. \quad (3.22)$$

Here χ is the indicator function, i.e. $\chi_{\mathcal{P}_i}(k) = 1$ if $k \in \mathcal{P}_i$ and $\chi_{\mathcal{P}_i}(k) = 0$ if $k \notin \mathcal{P}_i$. Moreover, the hybridization function is now diagonal in the cluster momentum

$$\Delta(K_i, \omega) = \sum_{i, \lambda} \frac{V_{i, \lambda} \bar{V}_{i, \lambda}}{\omega - \epsilon_{i, \lambda}}. \quad (3.23)$$

Solving the cluster impurity model yields the self-energy $\Sigma(K_i, \omega)$ and the cluster Green’s function

$$G_{\text{cl}}(K_i, \omega) = [\omega + \mu - \epsilon_{K_i} - \Delta(K_i, \omega) - \Sigma(K_i, \omega)]^{-1}. \quad (3.24)$$

Altogether, one obtains a self-consistency equation for each of the N_c cluster momenta K_i

$$G_{\text{latt}}(K_i, \omega) \stackrel{!}{=} G_{\text{cl}}(K_i, \omega). \quad (3.25)$$

It can be solved following the iteration scheme described in section 2.3. The hybridization function is extracted from the self-consistency equation via

$$\Delta(K_i, \omega) = \omega + \mu - \epsilon_{K_i} - \Sigma(K_i, \omega) - G_{\text{latt}}^{-1}(K_i, \omega). \quad (3.26)$$

In contrast to CDMFT, the self-energy is already diagonal in momentum space by the construction of DCA. Though, it is discontinuous between the different momentum patches of the cluster momenta K_i . This issue can be cured by interpolating the self-energy between different patches. Nevertheless,

the choice of interpolation scheme is not unique and arbitrary to some extent. However, for momentum independent quantities no interpolation is necessary and the self-energy, obtained from DCA, can be used without post-processing.

4 Numerical renormalization group (NRG)

Originally developed by K. Wilson to solve the Kondo problem [14] NRG has become a powerful impurity model solver, which forms the backbone for our DMFT calculations. Within NRG real-frequency objects, such as the self-energy, can be calculated directly without the need for ill-posed numeric analytic continuation. Moreover, arbitrarily low temperatures can be resolved. One drawback of NRG is that it is only applicable to systems with a few orbitals, due to the exponential scaling of the computational complexity. The NRG routines used in this thesis, have been developed by Andreas Weichselbaum and Seung-Sup Lee. This section follows the review [3] to describe the main ideas behind NRG, using the example of the single impurity Anderson model (SIAM). Furthermore, useful extensions to the basic NRG scheme are briefly mentioned.

4.1 Impurity models

Impurity models involve a small number of interacting degrees of freedom coupled to a non-interacting bath. For the sake of simplicity, this section follows the SIAM to explain the basic structure of a quantum impurity model. The SIAM Hamiltonian consists of three constituents, impurity, bath, and hybridization.

$$H = H_{\text{imp}} + H_{\text{bath}} + H_{\text{hyb}} \quad (4.1)$$

$$H_{\text{imp}} = (E_f - \mu) \sum_{\sigma} f_{\sigma}^{\dagger} f_{\sigma} + U n_{f,\uparrow} n_{f,\downarrow} \quad (4.2)$$

$$H_{\text{bath}} = \sum_{k,\sigma} \epsilon_k d_{k,\sigma}^{\dagger} d_{k,\sigma} \quad (4.3)$$

$$H_{\text{hyb}} = \sum_{k,\sigma} V_{k,\sigma} (f_{\sigma}^{\dagger} d_{k,\sigma} + h.c.) \quad (4.4)$$

Here operators $d_{k,\sigma}$ and f_{σ} fulfill fermionic anti-commutation relations: $\{f_{\sigma}, f_{\sigma'}^{\dagger}\} = \delta_{\sigma,\sigma'}$, $\{d_{k,\sigma}, d_{k',\sigma'}^{\dagger}\} = \delta_{k,k'} \delta_{\sigma,\sigma'}$. The interacting impurity site couples via the hybridization term to a non-interacting bath with dispersion ϵ_k . It turns out that the parameters of the bath are fully determined by the hybridization function:

$$\Delta(\omega) = \sum_k \frac{V_k^2}{\omega - \epsilon_k}. \quad (4.5)$$

The treatment of the SIAM with NRG involves discretization of the Hamiltonian. For this reason, it is helpful to introduce an energy-representation with dispersion $g(\epsilon)$ and hybridization $h(\epsilon)$.

$$H = H_{\text{imp}} + \sum_{\sigma} \int_{-1}^1 d\epsilon g(\epsilon) a_{\epsilon,\sigma}^{\dagger} a_{\epsilon,\sigma} + \sum_{\sigma} \int_{-1}^1 d\epsilon h(\epsilon) (f_{\sigma}^{\dagger} a_{\epsilon,\sigma} + h.c.) \quad (4.6)$$

Here it is assumed that the support of $\Delta(\omega)$ lies within the interval $[-D, D]$, in which D is the half bandwidth. Without loss of generality, we set $D = 1$ as the scale of energy in the following sections.

4.2 Logarithmic discretization and discretized Hamiltonian

One of the core ingredients of NRG is logarithmic discretization. The band is split up into a set of intervals $I_{n,\pm} = [\pm\Lambda^{-(n+1)}, \pm\Lambda^{-n}]$ of width $d_n = \Lambda^{-n}(1 - \Lambda^{-1})$, with the discretization parameter

$\Lambda > 1$. In each of the intervals an orthonormal and complete set of functions can be introduced:

$$\Psi_{np}^{\pm}(\epsilon) = \begin{cases} \frac{1}{\sqrt{d_n}} \exp(\pm \omega_n p \epsilon) & \text{for } \pm \epsilon \in I_{n,\pm}, \\ 0 & \text{otherwise.} \end{cases} \quad (4.7)$$

Here, with $p \in \mathbb{Z}$, the description is still exact. In NRG usually only the $p = 0$ contribution will be kept. Motivation for this approximation is that the $p \neq 0$ states couple only indirectly via the $p = 0$ state to the impurity. Moreover the coupling between $p \neq 0$ and $p = 0$ has a prefactor $(1 - \Lambda^{-1})$. In the limit $\Lambda \rightarrow 1$, the exact solution is recovered. After dropping the $p \neq 0$ contributions the Hamiltonian (4.6) can be written in its approximate discretized form:

$$H = H_{\text{imp}} + \sum_{\sigma} \sum_n \xi_n^+ a_{n,\sigma}^{\dagger} a_{n,\sigma} + \xi_n^- b_{n,\sigma}^{\dagger} b_{n,\sigma} + \frac{1}{\sqrt{\pi}} \sum_{\sigma} \sum_n (\gamma_n^+ f_{\sigma}^{\dagger} a_{n,\sigma} + \gamma_n^- f_{\sigma}^{\dagger} b_{n,\sigma} + h.c.). \quad (4.8)$$

The hopping amplitudes γ_n^{\pm} and on-site energies ξ_n^{\pm} are fully determined by the hybridization function through

$$(\gamma_n^{\pm})^2 = \int_{I_{n,\pm}} d\epsilon \Delta(\epsilon), \quad (4.9)$$

$$\xi_n^{\pm} = \frac{\int_{I_{n,\pm}} d\epsilon \Delta(\epsilon) \epsilon}{\int_{I_{n,\pm}} d\epsilon \Delta(\epsilon)}. \quad (4.10)$$

In the Hamiltonian (4.8) the impurity site couples to each of the bath sites. This star-like geometry can be mapped onto a semi-infinite chain using the Lanczos method:

$$H = H_{\text{imp}} + \sum_{\sigma} \frac{\sqrt{\xi_{\sigma}}}{\pi} (f_{\sigma}^{\dagger} c_{0,\sigma} + h.c.) + \sum_{\sigma} \sum_{n=0}^{\infty} [\epsilon_n c_{n,\sigma}^{\dagger} c_{n,\sigma} + t_n (c_{n,\sigma}^{\dagger} c_{n+1,\sigma} + h.c.)]. \quad (4.11)$$

The operators $c_{n,\sigma}$ are linear combinations of $a_{n,\sigma}$, $b_{n,\sigma}$ and form an orthonormal set. In the resulting Hamiltonian the impurity only couples to the first bath site. In general, the on-site energies ϵ_n and hopping amplitudes t_n are determined through a recursion relation. For the special case of constant hybridization $\Delta(\omega) = \Delta_0$ with support in $[-1, 1]$, Wilson derived a analytic formula for the hopping amplitudes [14]:

$$t_n = \frac{(1 + \Lambda^{-1})(1 - \Lambda^{-n-1})}{2\sqrt{1 - \Lambda^{-2n-1}}\sqrt{1 - \Lambda^{-2n-3}}} \Lambda^{n/2} \stackrel{n \gg 1}{\sim} \frac{1}{2}(1 + \Lambda^{-1})\Lambda^{-n/2}. \quad (4.12)$$

For large n the hopping amplitudes t_n fall off exponentially. In DMFT the hybridization function can take arbitrary form, however, the exponential scaling of the hopping amplitudes is always fulfilled for large n . This originates from the logarithmic discretization chosen at the beginning and will be of importance for the NRG scheme to work. For more details on the discretization of the Hamiltonian and the mapping onto the semi-infinite chain see Ref. [3], section B, C.

4.3 Iterative Diagonalization

Starting from the Hamiltonian (4.11) the NRG scheme can be defined. Ultimately, the goal is to calculate the energy eigenstates of the chain Hamiltonian. Since exact diagonalization is computa-

tionally only possible for short chain lengths, an iterative diagonalization scheme is used. The basic idea is to start at the impurity site, diagonalize the Hamiltonian, extend the Hamiltonian by adding one bath site and diagonalize again. Repeating this procedure, the so-called Wilson chain is formed. By iteratively adding more bath sites to the chain the Hilbert space grows exponentially and thus it has to be truncated at some point to make diagonalization feasible. This is achieved by only keeping the lowest energy eigenstates up to some threshold after each iteration. The truncation is meaningful since each added bath site perturbs the Hamiltonian only weakly due to the energy scale separation introduced by the exponentially decaying hopping amplitudes (see Eq. (4.12)). Therefore the low energy spectrum at later iterations is not affected by the high energy spectrum at previous iterations. Furthermore, it is advantageous to rescale the Hamiltonian at each iteration step N by $\Lambda^{(N-1)/2}$. Consequently the finite chain Hamiltonian at iteration N reads

$$H_N = \Lambda^{(N-1)/2} [H_{\text{imp}} + \frac{\xi_0}{\pi} \sum_{\sigma} (f_{\sigma}^{\dagger} c_{0,\sigma} + h.c.) + \sum_{\sigma} \sum_{n=0}^N \epsilon_n c_{n,\sigma}^{\dagger} c_{n,\sigma} + \sum_{\sigma} \sum_{n=0}^{N-1} t_n (c_{n,\sigma}^{\dagger} c_{n+1,\sigma} + h.c.)]. \quad (4.13)$$

The factor $\Lambda^{(N-1)/2}$ is useful since it cancels the N -dependence of the hopping amplitude t_{N-1} which will be important for fixed points of the energy spectrum. The semi-infinite chain Hamiltonian is recovered in the limit $H = \lim_{N \rightarrow \infty} \Lambda^{-(N-1)/2} H_N$. Moreover, H_{N+1} can be related to its predecessor H_N by

$$H_{N+1} = \sqrt{\Lambda} H_N + \Lambda^{N/2} \sum_{\sigma} \epsilon_{N+1} c_{N+1,\sigma}^{\dagger} c_{N+1,\sigma} + \lambda^{N/2} \sum_{\sigma} t_N (c_{N,\sigma}^{\dagger} c_{N+1,\sigma} + h.c.). \quad (4.14)$$

Each Hamiltonian H_N is characterized by its eigenstates and eigenvalues $|r\rangle_N, E_N(r)$. Combining the iterative diagonalization procedure described in the beginning with the smart formulation of the series of Hamiltonians H_N , the NRG scheme is defined as:

1. Assuming the energy-eigenstates $|r\rangle_N$ and the corresponding eigenvalues $E_N(r)$ of the Hamiltonian H_N are known, i.e. $H_N |r\rangle_N = E_N(r) |r\rangle_N$. The Hilbert space of the subsequent Hamiltonian H_{N+1} is spanned by $\{|r\rangle \otimes |s\rangle\}$, in which the states $|s\rangle$ form the Hilbert space of the added bath-site. Note, this operation enlarges the Hilbert space by a factor of the dimension of bath-sites Hilbert space.
2. Diagonalize the constructed Hamiltonian H_{N+1} , yielding new eigenstates and eigenvalues $|r'\rangle_{N+1}, E_{N+1}(r')$. However, with an increasing dimension of the Hilbert space diagonalization becomes infeasible quickly. Therefore the Hilbert space has to be truncated by introducing a cutoff N_k , s.t. the lowest N_k states are kept, while the rest is discarded. As mentioned before, this truncation is meaningful due to the exponentially decaying hopping amplitudes. Each added chain site can be viewed as a perturbation of order $\Lambda^{-1/2}$ to the Hamiltonian H_N . Therefore the high energy eigenstates of H_N have negligible impact on the low energy behavior of H_{N+1} .
3. Repeat step 1.) & 2.) until the desired energy resolution is reached.

The transformation $H_{N+1} = \mathcal{T}(H_N)$, can be seen as a RG transformation. It takes the Hamiltonian H_N , rescales it by $\sqrt{\Lambda}$ and extends it by an additional bath site. Moreover, in every iteration, the energy spectrum is truncated and high energy states are discarded, which is similar to successively

integrating out high energy degrees of freedom in common RG schemes. Reiterating \mathcal{T} lets the system flow to a fixed point, which is manifest in the flow of the energy spectrum through the NRG iterations. More specifically \mathcal{T}^2 , i.e. even and odd iterations show fixed-point behavior. The flow of the energy spectrum and its fixed points throughout the iterations can be useful for analyzing the numeric results, as we will see later. Note that the runtime of the described iterative scheme scales linearly in the chain length. Therefore it is possible to reach arbitrary low energy resolution, which is a powerful aspect of NRG.

4.4 Useful extensions

There are many important extensions to the basic NRG scheme. In the following, some of them are mentioned briefly.

Exploiting symmetries:

To reduce computational cost it is useful to exploit all symmetries of the model of interest. A symmetry of a system is described by its symmetry group. The symmetry is obeyed if the Hamiltonian commutes with the generators of the symmetry group. In return, this means that the eigenstates of the Hamiltonian can be labeled by the eigenvalues of the Casimir operators of the symmetry groups. For example in the SIAM, if one focuses on states with $U(1)$ charge and $SU(2)$ spin rotation symmetry, states can be labeled by charge Q and spin S , i.e. the Hamiltonian is diagonal in each sector described by $[Q, S]$. This is of great benefit because the full Hamiltonian takes a block diagonal form, which makes diagonalization more efficient by simply diagonalizing each block. In the QSpace library [15], developed by A. Weichselbaum, NRG is formulated in the framework of matrix product states (MPS) in which discrete, abelian, and non-abelian symmetries can be exploited.

Full density matrix NRG (fDMNRG):

Dynamical quantities such as spectral functions, represented through the Lehmann representation, require a sum over a complete many-body basis. The approximate low energy eigenstates obtained by NRG do not span the full Hilbert space. F. Anders and A. Schiller had the insight to use the discarded states at each NRG iteration to construct a complete many-body basis [16]. Utilizing the complete many-body basis a scheme to calculate spectral functions of impurity models can be formulated, without introducing further approximations [17].

Interleaved NRG (iNRG):

Multi-band models consisting of orbitals with n flavors of dimension d , increase the size of the Hilbert space by a factor of $d \cdot n$, at each NRG iteration. Thus diagonalization becomes infeasible quickly. The idea of iNRG is to add the flavors of the full orbital successively to the Wilson chain and truncate the Hilbert space at each step, reducing the growth factor to d and increasing the chain length by n . Though an artificial energy scale separation between the flavors is introduced and if present, symmetries between flavors are broken. Nevertheless, if used appropriately iNRG performs similarly as standard NRG at lower computational cost ([18],[19]).

5 Cold atoms, a DMFT analysis

Cold atoms trapped in optical lattices offer an interesting platform to study many-body quantum systems [4]. Recent experiments propose to use Alkaline-earth atoms such as Ytterbium to model two orbital fermionic systems. The lowest-lying states in the electronic configuration of fermionic ^{173}Yb are a singlet 1S_0 and a triplet 3P_0 . In the following, the singlet will be referred to as the ground state “g” and the triplet as an excited state “e”. Experimentally each state can be controlled in a state-dependent optical lattice. For more details on the experimental realization see [20]. Altogether this makes Ytterbium-based cold atom experiments a suitable candidate as an “analog quantum simulator” for two-orbital models such as the Kondo lattice, where hybridization between localized and itinerant electrons is crucial.

The Quantum optics group at LMU lead by Simon Fölling has experimentally realized a Kondo lattice-like system. It is designed to model the following Hamiltonian.

$$H = H_g^{\text{hop}} + H_e^{\text{hop}} + H_{gg}^{\text{int}} + H_{ee}^{\text{int}} + H_{ge}^{\text{int}} \quad (5.1)$$

$$H_g^{\text{hop}} = -t_g \sum_{\langle i,j \rangle, \sigma} (g_{i,\sigma}^\dagger g_{j,\sigma} + h.c.) \quad (5.2)$$

$$H_e^{\text{hop}} = -t_e \sum_{\langle i,j \rangle, \sigma} (e_{i,\sigma}^\dagger e_{j,\sigma} + h.c.) \quad (5.3)$$

$$H_{gg}^{\text{int}} = \frac{U_{gg}}{2} \sum_i n_{g,i} (n_{g,i} - 1) \quad (5.4)$$

$$H_{ee}^{\text{int}} = \frac{U_{ee}}{2} \sum_i n_{e,i} (n_{e,i} - 1) \quad (5.5)$$

$$\begin{aligned} H_{ge}^{\text{int}} &= V \sum_i n_{e,i} n_{g,i} + J \sum_{i,\sigma',\sigma} g_{i,\sigma}^\dagger e_{i,\sigma'}^\dagger g_{j,\sigma'} e_{j,\sigma} \\ &= (V - \frac{J}{2}) \sum_i n_{e,i} n_{g,i} - 2J \sum_i \vec{S}_{g,i} \cdot \vec{S}_{e,i} \end{aligned} \quad (5.6)$$

Each atom species, represented by the fermionic operators $g_{\sigma,i}, e_{\sigma,i}$, has a finite hopping amplitude $t_{g/e}$ and an on-site repulsion given by $U_{gg/ee}$. Moreover, the two different atomic states interact via an antiferromagnetic coupling J ($J < 0$, following the experimental convention) and a density-density repulsion proportional to $(V - J/2)$. Experimentally accessible parameter sets are given in Tab. 5.1. They are labeled by the state-dependent optical lattice depth $s_{g/e}$, measured in recoil energy E_r for ground-state atoms. Note that the tight-binding limit is not valid for lattice depths $s_g/E_r < 3$ and the next-nearest neighbor hopping amplitude for ground-state atoms is not negligible anymore, but it still might be helpful to explore favorable parameter sets. The parameter sets and information about their experimental relevance are provided by Nelson Darkwah Oppong.

s_g/E_r	s_e/E_r	U_s/t_g	U_t/t_g	V/t_g	J/t_g	U_{ee}/t_g	U_{gg}/t_g	t_e/t_g	D/t_g	$t_g/(hxHz)$
1	3.3	2.75	1.7	2.22	-0.53	1.06	-0.02	0.54	4	502.78
2	6.6	5.25	3.24	4.24	-1	2.21	-0.03	0.29	4	385.09
3	9.9	8.87	5.47	7.17	-1.7	3.77	-0.05	0.17	4	293.75
4	13.2	14.01	8.64	11.33	-2.68	5.89	-0.07	0.11	4	224.19
5	16.5	21.14	13.04	17.09	-4.05	8.77	-0.11	0.07	4	171.75
6	19.8	30.87	19.05	24.96	-5.91	12.65	-0.16	0.05	4	132.32

Tab. 5.1: Experimental accessible parameter sets.

By adjusting the state-dependent optical lattice depth $s_{g/e}$, the singlet and triplet interaction U_s and U_t can be tuned, which define the interaction parameters in the Hamiltonian:

$$J = \frac{U_t - U_s}{2}, \quad V = \frac{U_t + U_s}{2}. \quad (5.7)$$

In the following analysis, the on-site interaction U_{gg} will be omitted, since it is negligibly small compared to all other interaction parameters.

We are interested in studying the model described by the Hamiltonian (5.1) in the framework of DMFT, to investigate the different experimental parameter sets and possible guide experimentalists to interesting parameter regimes. Our analysis is separated into two parts. First, we take a more in-depth look at the parameter set $s_g/E_r = 3$ and demonstrate the influence of the repulsive interaction V between g and e states and how it affects the existence of different phases. Afterward, the different experimental parameter sets are compared.

5.1 Method

Within DMFT the lattice model described by the Hamiltonian (5.1) is solved through a self-consistent mapping onto an impurity model. Its Hamiltonian reads

$$H = H_{\text{imp}} + H_{\text{bath}} \quad (5.8)$$

$$H_{\text{imp}} = \frac{U_{ee}}{2} n_e (n_e - 1) - \mu_e \sum_{\sigma} e_{\sigma}^{\dagger} e_{\sigma} - \mu_g \sum_{\sigma} g_{\sigma}^{\dagger} g_{\sigma} + (V - \frac{J}{2}) n_e n_g - 2J \vec{S}_g \cdot \vec{S}_e \quad (5.9)$$

$$H_{\text{bath}} = \sum_{\lambda=e,g} \sum_{\lambda,k,\sigma} E_{\lambda,k} b_{\lambda,k,\sigma}^{\dagger} b_{\lambda,k,\sigma} + \sum_{k,\sigma} V_{e,k} (b_{e,k,\sigma}^{\dagger} e_{k,\sigma} + h.c.) + \sum_{k,\sigma} V_{g,k} (b_{g,k,\sigma}^{\dagger} g_{k,\sigma} + h.c.). \quad (5.10)$$

Here the operators g_{σ}, e_{σ} , correspond to the two different types of fermionic atoms and fulfill fermionic anti-commutation relations. Furthermore, the bath parameters $E_{\lambda,k}, V_{e/g,k}$ are fully determined by the hybridization function

$$\Delta_{e/g} = \sum_k \frac{V_{e/g,k}^2}{\omega - E_{e/g,k}}. \quad (5.11)$$

The impurity model is solved by interleaved NRG, which does not show meaningful deviations to results obtained from standard NRG, but reduces the computational cost. We focus only on the paramagnetic phases, as a constraint, in which the rotational spin symmetry (i.e $SU(2)$ spin symmetry) is not broken. This enables us to exploit $U(1)_{\text{charge}} \otimes SU(2)_{\text{spin}}$ symmetry in the NRG calculations, further reducing the computational cost. As discretization parameter $\Lambda = 4$ is used and $N_k = 3000$ multiplets are kept each NRG iteration. Moreover, $n_z = 2$ z-shifts are performed. Using smaller Λ or higher N_k does not improve the results significantly.

The self-consistent mapping between the lattice and impurity model is done as described in section 2.3. The semi-elliptic density of states of the infinite dimensional Bethe lattice is used for the lattice model:

$$\rho_{g/e}(\epsilon) = \frac{1}{\pi} \sqrt{1 - \left(\frac{\epsilon}{t_{g/e}}\right)^2}. \quad (5.12)$$

It is a common convenient choice because it leads to an analytic self-consistency equation

$$G_{\text{latt}}(\omega) = \frac{1}{2t_{g/e}^2} \left(\xi - \sqrt{\xi^2 - 4t_{g/e}^2} \right), \quad (5.13)$$

$$\xi = \omega + \mu_{g/e} - \Sigma_{g/e}(\omega), \quad (5.14)$$

which makes it possible to avoid numerical integration. Note, it is possible to use the DOS of e.g. a cubic lattice with suitable integration routines, but it does not affect the results qualitatively. For the following, calculations we will set $t_g \equiv 1$ as a unit of energy.

5.2 Influence of repulsive interaction V

Crucial for the stability of the DMFT solution is the magnitude of the interaction parameter V since it leads to a large repulsion between the two bands. For the following analysis the parameter set with $s_g/E_r = 3$ in Tab. 5.1 is used. All parameters, except for V , are kept as they are given. For increasing V we scan over the chemical potentials μ_e, μ_g , to adjust the filling n_g, n_e of the corresponding bands. The averaged fillings are calculated from the converged DMFT solution by integrating the spectral functions. Two different temperatures $T/t_g = 10^{-8}$ and $T/t_g = 0.1$ are considered.

$T = 0$ phase diagram:

First, the phase diagram for $T/t_g = 10^{-8}$ will be calculated. The chemical potential of the g-band is fixed to $\mu_g = U_{ee}/2 = 1.885$, we vary $\mu_e \in [0,6]$, $V \in [-0.85 - 7.15]$, with step sizes of $\Delta\mu_e = 0.25$, $\Delta V = 0.5$. Our strategy of scanning the chemical potential is motivated by the local energy level structure, which will be discussed later. Different strategies to scan over the chemical potentials μ_e, μ_g do not lead to superior results. For each pair V, μ_e the average fillings $\langle n_g \rangle, \langle n_e \rangle$ are calculated. Fig. 5.1 shows the results of the calculations. There exist mainly four different regimes: $(n_g, n_e) = (2, 0)$; $(n_g, n_e) = (0, 1)$; $(n_g, n_e) = (0, 2)$ and $(n_g, n_e) \simeq (1, 1)$. The latter is the only interesting regime, since both bands have simultaneous non-zero occupation. This interesting regime is represented by the turquoise region in Fig. 5.1 and its boundaries. For small V the transitions $(n_g, n_e) = (2, 0) \rightarrow (n_g, n_e) \simeq (1, 1)$ and $(n_g, n_e) \simeq (1, 1) \rightarrow (n_g, n_e) = (0, 2)$ can be observed by increasing μ_e . However, with increasing V the turquoise region narrows and at approximately

$V \approx 4$ it breaks down completely and a direct transition $(n_g, n_e) = (2, 0) \rightarrow (n_g, n_e) = (0, 2)$ or $(n_g, n_e) = (2, 0) \rightarrow (n_g, n_e) = (0, 1)$ occurs when μ_e is increased. It is not possible to fine-tune μ_e to reach intermediate fillings. It always appears a jump in the occupation. This discontinuity is smeared out at higher temperatures and the transition becomes continuous, see Fig. 5.3.

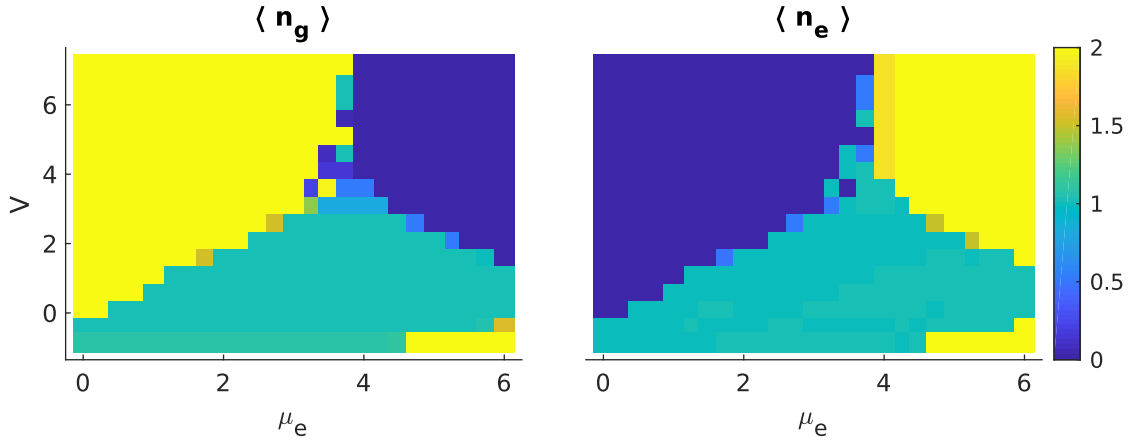


Fig. 5.1: Dependence of the average occupancies $\langle n_g \rangle, \langle n_e \rangle$ on interaction strength V and chemical potential μ_e for temperature $T/t_g = 10^{-8}$. The data points where fractional fillings of $\langle n_e \rangle$ occur in the transition regions are unfortunately all unstable DMFT solutions and therefore not representative.

It turns out, that the general structure of the phase diagram and the influence of the repulsive interaction V , can be understood from the local energy levels, which will be discussed later in section 5.3.

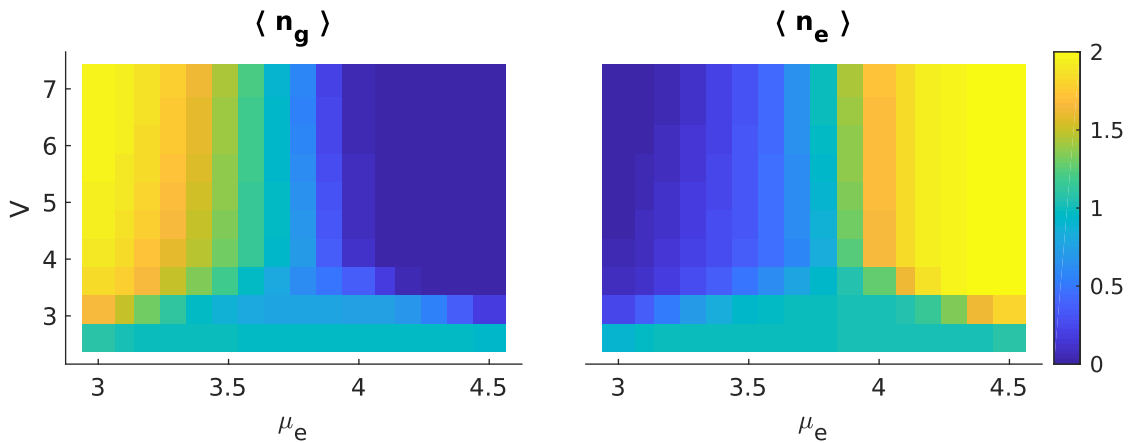


Fig. 5.2: Dependence of average occupancies $\langle n_g \rangle, \langle n_e \rangle$ on interaction strength V and chemical potential μ_g for temperature $T/t_g = 0.1$.

$T/t_g = 0.1$, phase diagram:

The phase diagram for a temperature of $T/t_g = 0.1$ is calculated the same way as for $T/t_g = 10^{-8}$, $\mu_g = U_{ee}/2$ is fixed and μ_e is varied. To resolve the transition region μ more precisely, we focus on the

region $\mu_e \in [3, 4.5]$, $V \in [2.65, 7.15]$ with step sizes $\Delta\mu_e = 0.1$, $V = 0.5$. The results are presented in Fig. 5.2. Contrary to the $T = 10^{-8}$ phase diagram in Fig. 5.1, the transition between the different regimes is now continuous and fractional fillings can be observed in the transition region. Fig. 5.3 illustrates the filling transition for the different temperatures $T = 0.1, 10^{-8}$. For $T = 10^{-8}$ the transition exhibits a sharp jump and there exists a region where the DMFT solution is not stable. In contrast, for $T/t_g = 0.1$ the transition becomes smooth and fractional fillings can be observed.

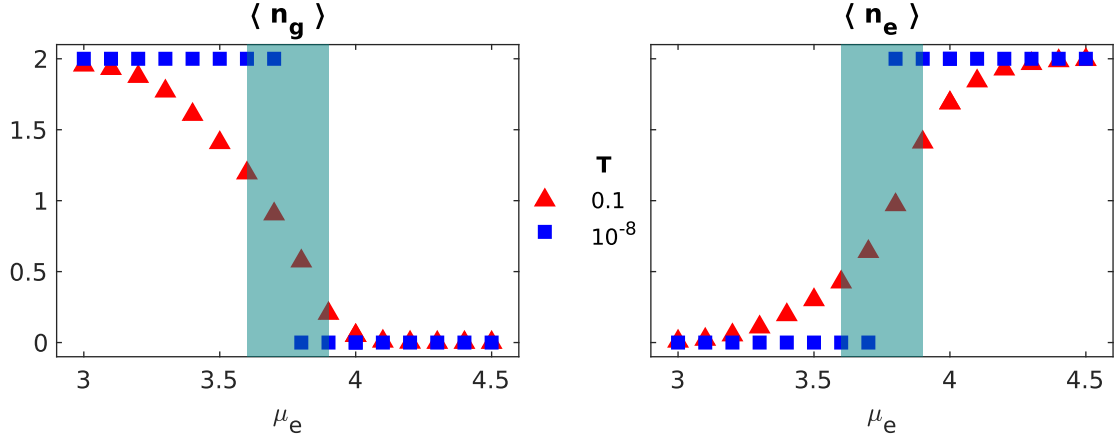


Fig. 5.3: Temperature dependence of filling transition for $V = 7.15$ for $T/t_g = 0.1, 10^{-8}$. The shaded region indicates a region of instability of the DMFT solution for $T/t_g = 10^{-8}$.

Moreover, results for the spin-spin correlation $\langle S_g \cdot S_e \rangle$ and charge-charge correlation $\langle n_g \cdot n_e \rangle$ of g and e atoms are presented in Fig. 5.4.

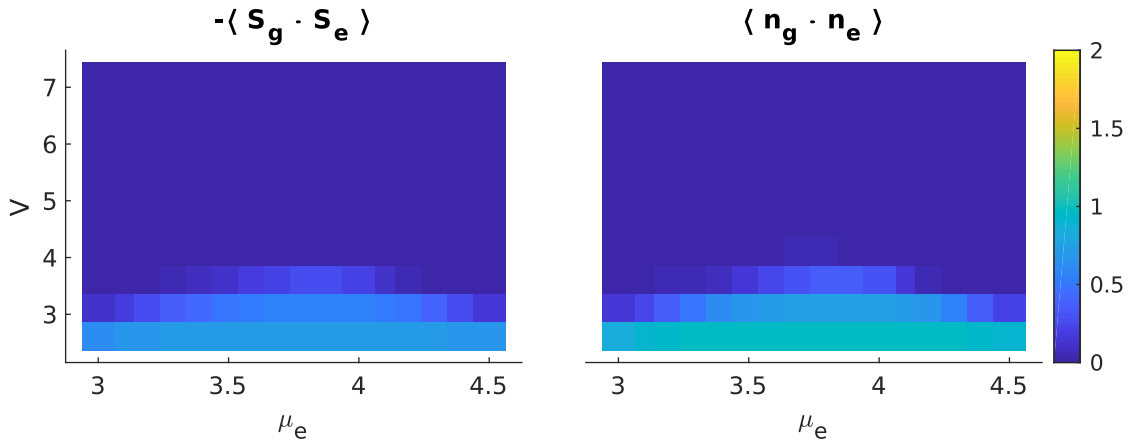


Fig. 5.4: Dependence of spin-spin correlation $\langle S_g \cdot S_e \rangle$ and charge-charge correlation $\langle n_g \cdot n_e \rangle$ on interaction strength V and chemical potential μ_e for temperature $T/t_g = 0.1$

We only find a non-zero spin-spin and charge-charge correlation up to $V \approx 4$. The spin-spin correlation being negative reveals singlet formation in the regime $(n_g, n_e) \simeq (1, 1)$. For larger values of V there exists a regime of $(n_g, n_e) \simeq (1, 1)$ in the transition region between $(n_g, n_e) = (0, 2)$ and $(n_g, n_e) = (2, 0)$. However, spins and charge of the different atomic states remain uncorrelated,

indicating the existence of a mixture of states where either n_g or n_e is zero. Later more details on this phase are discussed by looking at the local spectral functions. But first we will review the local energy level structure which turns out to be insightful for the phase diagram and the local spectral functions.

5.3 Local energy levels

In the phase diagrams, presented in the previous section, the following regimes appear: $(n_g, n_e) = (2, 0)$; $(n_g, n_e) = (0, 1)$; $(n_g, n_e) = (0, 2)$; $(n_g, n_e) = (1, 1)$. These can be understood from looking at the local energy levels. In Tab. 5.2 the ground state energies E_g in dependence of the occupation numbers n_g, n_e and the total spin S are displayed.

	n_g	n_e	S	E_g
1.	2	0	0	$-2\mu_g$
2.	0	1	$\frac{1}{2}$	$-\mu_e$
3.	0	2	0	$-2\mu_e + U_{ee}$
4.	1	1	0	$-\mu_g - \mu_e + J + V$
5.	1	1	1	$-\mu_g - \mu_e - J + V$

Tab. 5.2: Ground state energies E_g of local energy levels for different occupation numbers n_g, n_e and total spin S .

To understand under which circumstances simultaneous occupation is energetically favorable, we compare the ground-state energies. This will give constraints for μ_e, μ_g to reach the desired regime. We only consider the case where $(n_g, n_e) = (1, 1)$ forms a singlet (i.e. $S = 0$), which gives rise to an energy gain of $3/2J$ originating from the spin-spin interaction $-2J\vec{S}_e \cdot \vec{S}_g$. Ground state energies are indexed by the rows in Tab. 5.2.

1.) $E_{g,4} < E_{g,1}$:

$$-\mu_e - \mu_g + V + J < -2\mu_g \iff V + J < \mu_e - \mu_g \quad (5.15)$$

2.) $E_{g,4} < E_{g,2}$:

$$-\mu_e - \mu_g + V + J < -\mu_e \iff V + J < \mu_g \quad (5.16)$$

3.) $E_{g,4} < E_{g,3}$:

$$-\mu_e - \mu_g + V + J < -2\mu_e + U_{ee} \iff \mu_e - \mu_g < +U_{ee} - J - V \quad (5.17)$$

Altogether the interesting state $(n_g, n_e) = (1, 1)$, where both orbitals are filled, is restricted in the following way:

If $V > \mu_g - J$ it is never energetically favourable against $(n_g, n_e) = (0, 1)$.

If $V < \mu_g - J$ it is favorable in the regime constrained by the inequalities 1.) and 3.):

$$V + J < \mu_e - \mu_g < U_{ee} - J - V. \quad (5.18)$$

Consequently, the critical V_c where the upper and lower bound of the inequality match, which is independent of the chemical potentials, is given by:

$$V_c + J = U_{ee} - J - V_c, \quad (5.19)$$

$$V_c = U_{ee}/2 - J = 3.585. \quad (5.20)$$

If V exceeds this critical value there is no stable regime where both orbitals are filled (from a local energy level perspective). Concluding, to possibly further increase V_c one would have to increase U_{ee} or J . Moreover, $\mu_g \geq J + V_c = U_{ee}/2$ should be satisfied. Even though we only consider the local energy levels here, this analysis shows agreement with the DMFT results presented in Fig. 5.1 and Fig. 5.2. It is visible that the turquoise region narrows in agreement with Eq. (5.18).

5.4 Experimental parameter sets

Now we turn our attention to the different experimental parameter sets, given in Tab. 5.1. We start with comparing the phase diagram of the different parameter sets for $T = 0.1$. Afterward, local spectral functions are analyzed for one particular parameter sets, justified by the fact that the overall behavior is qualitatively the same throughout all different parameter sets.

$T = 0.1/t_g$, phase diagram:

For each set, the goal is to reach the regime where both bands have a simultaneous non-zero occupation. For this purpose we calculate n_e, n_g on a suitable grid of μ_e, μ_g . From the local energy level perspective we know it is beneficial to satisfy $\mu_g \geq U_{ee}/2$. Moreover, the experimentally realizable combinations of V, J, U_{ee} , are in the regime $V > V_c = U_{ee}/2 - J$. Therefore only observable transition is between the regimes $(n_g, n_e) = (0, 2)$ and $(n_g, n_e) = (2, 0)$, which indicates $\mu_e = \mu_g + U_{ee}/2$ at the transition interface. Altogether, this motivates a (μ_g, μ_e) -grid around $(\mu_g, \mu_e) = (U_{ee}/2, U_{ee})$. Therefore a grid of $\mu_g \in [U_{ee}/2 - 0.4, U_{ee}/2 + 0.4]$ and $\mu_e \in [U_{ee} - 0.4, U_{ee} + 0.4]$ with a step size of $\Delta\mu_g = \Delta\mu_e = 0.1$ is used for the following calculations. All calculations are performed at $T = 0.1/t_g$. In Fig. 5.5 the results for the average occupations $\langle n_g \rangle, \langle n_e \rangle$ are displayed. For a better overview where both bands could be partially filled, we also plot the product $\langle n_g \rangle \cdot \langle n_e \rangle$. There it is visible that the (μ_g, μ_e) -grid is well chosen. The region of possible simultaneous occupation of both bands follows the line $\mu_e = \mu_g + U_{ee}/2$. For $(\mu_g, \mu_e) \geq (U_{ee}/2, U_{ee})$ the product $\langle n_g \rangle \cdot \langle n_e \rangle$ is the largest. Increasing the size of the (μ_g, μ_e) -grid in the direction with $(\mu_g, \mu_e) \geq (U_{ee}/2, U_{ee})$, does not lead to an enhancement of $\langle n_g \rangle \cdot \langle n_e \rangle$. The overall behavior is pretty similar throughout the six different parameter sets. Only the results for $s_g/E_r = 1$ displayed in Fig. 5.5 shows a slightly smaller $\langle n_g \rangle \cdot \langle n_e \rangle$ in the crossover region.

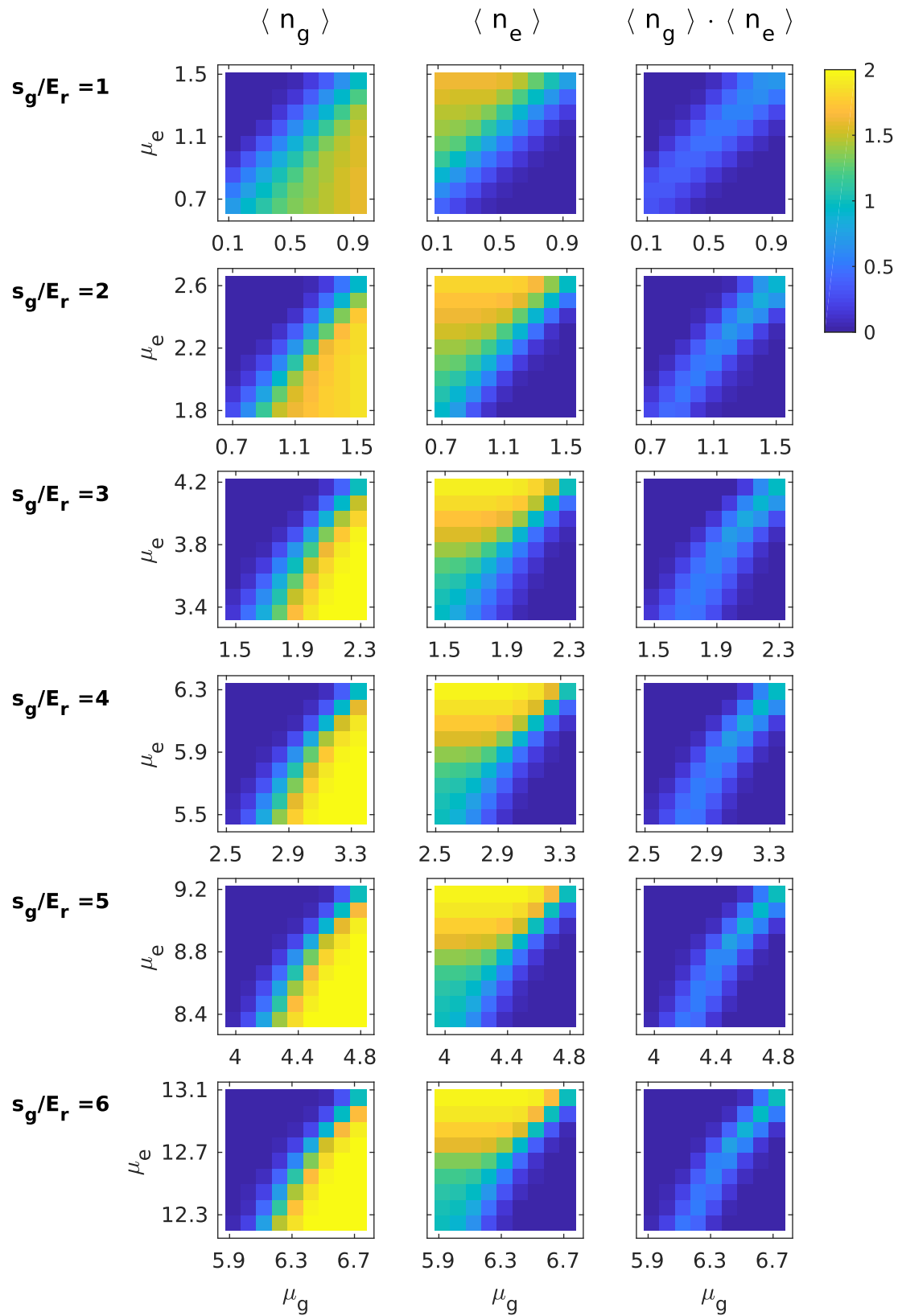


Fig. 5.5: Average densities $\langle n_g \rangle$, $\langle n_e \rangle$ and its product $\langle n_g \rangle \cdot \langle n_e \rangle$ plotted against the chemical potentials μ_g, μ_e for temperature $T = 0.1/t_g$. Each row labeled by s_g/E_r corresponds to one of the experimental parameter sets given in Tab. 5.1.

To get further insights into the configuration of the atoms, we look at the local spectral functions, which provide information about possible excitations and the configuration of the atoms.

Local spectral functions:

Having found regions where both bands have a non-zero average occupation, we study the physics of this configuration by looking at the local lattice spectral function. It turns out that the qualitative structure of the spectral functions is the same for the six different parameter sets. Therefore we choose the parameter set with $V = 7.17$, $U_{ee} = 3.77$, $J = -1.7$ to explain the basic structure of the spectral functions. Out of the phase diagram shown in Fig. 5.5 with $s_g/E_r = 3$, the data point $(\mu_g, \mu_e) = (U_{ee}/2, U_{ee})$ is chosen. The excitations in the spectral function are compared to the local energy levels, to check if there appear any interesting many-body effects. However, it turns out the excitation spectrum matches the local energy level structure, where the ground state is a mixture of the states $(n_g, n_e) = (0, 1)$, $(n_g, n_e) = (0, 2)$, $(n_g, n_e) = (2, 0)$. In Tab. 5.3 all possible transitions from these states are listed. In Fig. 5.6 the spectral functions along with the atomic transition energies are displayed.

Transition	ΔE
$(n_g, n_e, S) = (0, 1, 1/2) \rightarrow (1, 1, 0)$	$-\mu_g + V + J$
$(n_g, n_e, S) = (0, 1, 1/2) \rightarrow (1, 1, 1)$	$-\mu_g + V - J$
$(n_g, n_e, S) = (0, 2, 0) \rightarrow (1, 2, 1/2)$	$-\mu_g + 2V - J$
$(n_g, n_e, S) = (2, 0, 0) \rightarrow (1, 0, 1/2)$	$+\mu_g$
$(n_g, n_e, S) = (2, 0, 0) \rightarrow (2, 1, 1/2)$	$-\mu_e + 2V - J$
$(n_g, n_e, S) = (0, 1, 1/2) \rightarrow (0, 0, 0)$	$+\mu_e$
$(n_g, n_e, S) = (0, 1, 1/2) \rightarrow (0, 2, 0)$	$-\mu_e + U_{ee}$

Tab. 5.3: Energy cost ΔE for all possible local energy level transitions, assuming the ground state consists of a mixture of the states $(n_g, n_e) = (0, 1)$, $(n_g, n_e) = (0, 2)$ and $(n_g, n_e) = (2, 0)$.

A surprising feature of the spectral functions is that the e-band is metallic and the g-band is insulating. Since, $t_e/t_g = 0.17$, one would expect the g-band to be metallic because of the larger hopping amplitude. However, the large interaction strength V gives rise to a mixture of the states $(n_g, n_e) = (0, 1)$, $(n_g, n_e) = (0, 2)$, $(n_g, n_e) = (2, 0)$. While in the g-band the atoms are in a doubly occupied ground state, the e atoms double occupation is suppressed by the on-site repulsion U . The chemical potential $\mu_e = U_{ee}$ leads to a mixture of single and double occupation of the e-band and allows gapless excitations, which gives rise to the metallic state. Concluding, from a DMFT point of view it seems like the interaction strength V is simply too large compared to J and therefore suppresses any kind of state which is dominated by spin-spin-interaction and could potentially show many-body effects. However, this is not an easy problem to solve experimentally, since V and J can so far not be tuned independently.

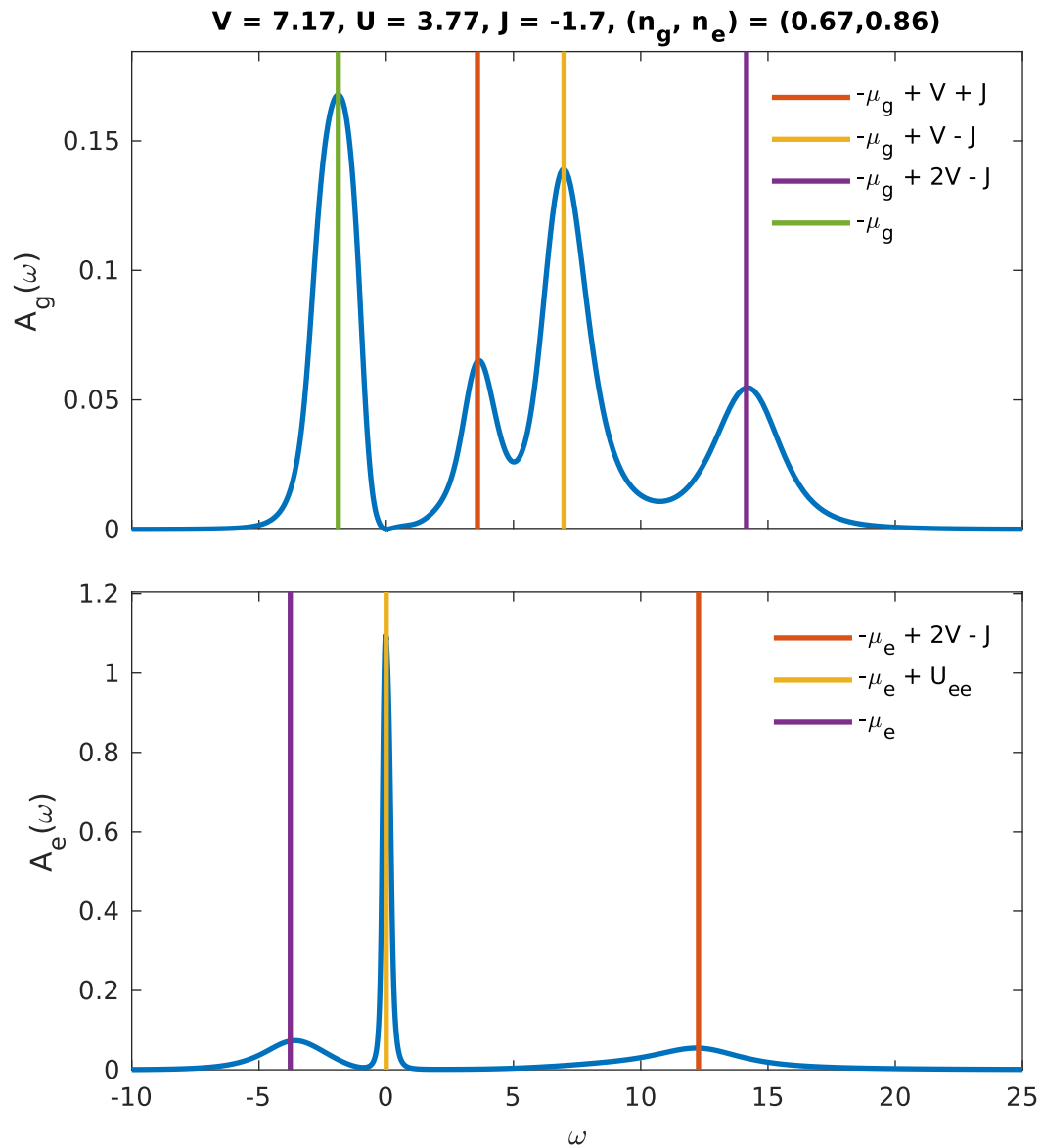


Fig. 5.6: Local spectral functions of g and e atoms for $(\mu_g, \mu_e) = (U_{ee}/2, U_{ee})$ and $s_g/E_r = 3$, i.e. interaction parameters $V = 7.17, U_{ee} = 3.77, J = -1.7$. The spectral functions are compared against the local energy level excitation energies, marked by the vertical lines. See Tab. 5.3 for more information on possible excitations.

6 Extended periodic Anderson model in the context of Samarium-Hexaboride

In mixed-valence (MV) compounds, ions exhibit valence fluctuations between different valence configurations. One such example is Samarium-Hexaboride (SmB_6). The electronic configuration of Samarium (Sm) is $[\text{Xe}]4f^65d^0s^2$. In rare-earth hexaborides the rare-earth ions are known to form a simple Cs-Cl type structure with B_6 forming an octahedron. Molecular cluster calculations [21] show that the configuration of the B_6 octahedra requires 20 electrons. Therefore divalent rare-earth hexaborides, such as EuB_6 , are assumed to be semiconductors, whereas trivalent compounds like LaB_6 , are expected to be metallic. SmB_6 however falls in neither of these categories. X-ray absorption measurements [22] show that the valence of Sm fluctuates between divalent Sm^{2+} and trivalent Sm^{3+} with an average valence of 2.6 at room temperature, which decreases to 2.5 at lower temperatures. Samarium-Hexaboride has been intensively studied experimentally since the 1970s and various anomalies in thermodynamic quantities, such as resistivity [23] and optical conductivity ([24],[25]), have been discovered. For instance, measurements of the DC electrical resistivity show an increasing resistivity with decreasing temperature, which saturates in a plateau at very low temperatures. Such observations have been used to argue that SmB_6 is an insulator at low temperatures with a bandgap originating from hybridization effects between d and f electrons ([26],[27]). Recent experiments show that SmB_6 exhibits quantum oscillations (QO), which seems to contradict the insulating behavior since QO are usually associated with a Fermi surface. It has been proposed [28] that SmB_6 is a topological insulator hosting topologically protected metallic surface states, which has been supported by many experiments, e.g. ([29],[29],[29]). Metallic surface states are used to explain the measured QO and thermodynamic anomalies, like the resistivity plateau. However, new experimental measurements of QO ([30], [31]), show similar angular dependence as measurements performed on metallic LaB_6 . The quantum oscillations are termed anomalous, as they deviate from the standard QO theory derived by Lifshitz and Kosevich [32], which is based on Fermi liquid theory. Moreover, they are found to be independent of the surface properties. For more details and an overview of experimental surface and bulk properties of SmB_6 , we refer the reader to the review [33].

Altogether, this indicates that the quantum oscillations originate from the bulk, which motivates us to focus on the bulk properties of SmB_6 . Nevertheless, this leaves us in a controversial situation. On the one hand, thermodynamic quantities such as the electric resistivity show insulating behavior. On the other hand, the measurement of quantum oscillations, point to the existence of a Fermi surface. However, it has been shown that even band insulators with small gaps at the order of the cyclotron frequency can exhibit anomalous quantum oscillations ([34], [35]), without hosting a Fermi surface. A different development suggests that the formation of a neutral Fermi surface [5], proposed by D. Chowdhury, I. Sodeman, and T. Senthil, can resolve the controversial experimental situation. They present a mechanism for the formation of “composite excitons”, which form the neutral Fermi surface. This has been the main motivation for our work and hence we quickly summarize the core ideas in the following.

Experiments on the electronic structure [36] reveal that the degenerate $4f^5$, $J = 5/2$ multiplet of Sm^{3+} splits into a low lying quartet (Γ_8) and a doublet (Γ_7). The ground state of the Sm ions is

therefore assumed to be fluctuating between:

$$4f^5(\Gamma_8) + 5d^1 \longleftrightarrow 4f^6. \quad (6.1)$$

As a minimal model, the quartet is replaced by a doublet, which makes it possible to model the electronic structure of SmB₆ by a two-band model, in which the occupation of the f and d electrons fluctuates between $(n_f, n_d) = (1,1) \leftrightarrow (2,0)$. The hybridization between f and d electrons and the Coulomb interaction between the more localized f electrons are taken into account by the periodic Anderson model (PAM). For the recipe of the ‘‘composite exciton’’ Chowdhury *et. al* extend the standard PAM by an additional Coulomb interaction between the f and d electrons and a finite electron hopping. The Hamiltonian reads

$$H = H_d + H_f + H_{df} \quad (6.2)$$

$$H_d = -\mu \sum_i d_{i,\sigma}^\dagger d_{i,\sigma} - t_d \sum_{\langle i,j \rangle, \sigma} (d_{i,\sigma}^\dagger d_{j,\sigma} + h.c.) \quad (6.3)$$

$$H_f = (E_f - \mu) \sum_i f_{i,\sigma}^\dagger f_{i,\sigma} - t_f \sum_{\langle i,j \rangle, \sigma} (f_{i,\sigma}^\dagger f_{j,\sigma} + h.c.) + \frac{U}{2} \sum_i n_{f,i} (n_{f,i} - 1) \quad (6.4)$$

$$H_{df} = V \sum_{i,\sigma} (f_{i,\sigma}^\dagger d_{i,\sigma} + h.c.) + U_{df} \sum_i n_{f,i} n_{d,i}. \quad (6.5)$$

They perform a particle hole transformation on the f electrons $f_{i,\sigma} = \tilde{f}_{i,\sigma'} \epsilon_{\sigma,\sigma'}$, here $\epsilon_{\sigma,\sigma'}$ is the fully anti-symmetric tensor. Moreover, a slave-boson representation $\tilde{f}_{i,\sigma} = b_i \chi_{i,\sigma}$, which factorizes the f-hole into a positive charged ‘‘holon’’ b and a neutral ‘‘spinon’’ $\chi_{i,\sigma}$, is used. The key idea for the formation of the composite exciton is that the repulsive interaction U_{df} between the d and f electrons acts as an attractive interaction between d electrons and f-holes, which leads to a bonding of the d electrons and the holon. Thus, the composite exciton is described by $\psi_{k,\sigma} = b_k d_{k,\sigma}$ and hybridizes with the leftover spinon. Altogether the composite exciton is electrically neutral by construction and can form a neutral Fermi surface. Consequently, the composite exciton has a insulating response to DC electric fields, but can exhibit quantum oscillations.

Our goal is to investigate whether such a formation of a neutral Fermi surface indeed occurs by performing DMFT and DCA calculations for the model described by the Hamiltonian given in Eq. (6.2). We will focus on the mixed-valence (MV) regime, which is given by $\langle n_f \rangle \approx 1.5$, $\langle n_d \rangle \approx 0.5$ and mimics the electronic configuration of SmB₆. Only paramagnetic phases are considered, in which the rotational spin symmetry (i.e $SU(2)$ spin symmetry) is not broken. This enables us to exploit $U(1)_{\text{charge}} \otimes SU(2)_{\text{spin}}$ symmetry in the NRG calculations.

Due to the high computational cost of multi-band models, we are restricted to solving impurity models with a maximum of two bands. Hence we can not include finite U_{df} and t_f in two-patch DCA calculations at the same time, since this would result in a four-band model. Therefore the analysis is split into two main parts. Firstly, we study the full Hamiltonian in the framework of standard DMFT. Secondly, we perform DCA calculations for the special cases $U_{df} \neq 0$, $t_f = 0$ and $U_{df} = 0$, $t_f \neq 0$. However, in our two-patch DCA calculations, it turns out that no nonlocal correlations are present in the mixed-valence regime.

Model parameters:

In the following analysis we choose $U = 10$, $V = 0.4$, ensuring $U > U_{df}, V$. Furthermore, the d-hopping

is set to $t_d = 1/6$, such that $D_d = 1$ is used as the unit of energy. Different values of U, V have been tested, however, readjusting of μ, E_f leads to qualitatively similar results. Thus, we will stick to the above-stated parameter choice if not specifically mentioned.

6.1 Non-interacting band structure

Since SmB_6 has a cubic lattice structure, a cubic dispersion is chosen:

$$\epsilon_{k,d} = -2t_d \sum_{i=x,y,z} \cos(k_i), \quad \epsilon_{k,f} = \frac{t_f}{t_d} \epsilon_{k,d}. \quad (6.6)$$

The non-interacting Hamiltonian can be diagonalized, giving rise to two bands with dispersions

$$E_{k,\pm} = \frac{(\tilde{\epsilon}_{k,d} + \tilde{\epsilon}_{k,f})}{2} \pm \sqrt{\frac{(\tilde{\epsilon}_{k,d} - \tilde{\epsilon}_{k,f})}{2} + V^2}, \quad (6.7)$$

in which $\tilde{\epsilon}_{k,d} = -\mu + \epsilon_{k,d}$ and $\tilde{\epsilon}_{k,f} = E_f - \mu + \epsilon_{k,f}$. We set $t_d = 1/6$, such that the half bandwidth is $D_d = 1$. Crucial parameters influencing the band structure are the half bandwidth of the f electrons D_f and the hybridization strength V between d and f electrons. In Fig. 6.1 the dispersions given in Eq. (6.7) is compared for different values of V and D_f .

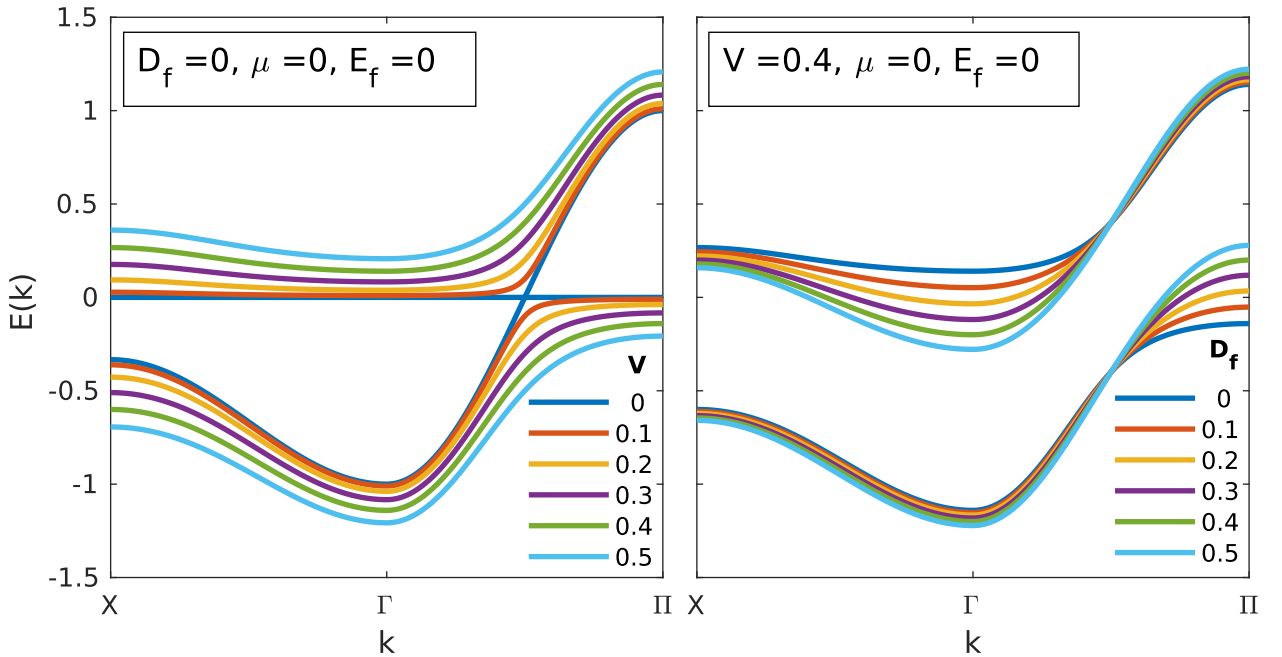


Fig. 6.1: Non-interacting band structure of the PAM with finite f electron dispersion. The upper band corresponds to $E_{k,+}$, the lower band to $E_{k,-}$, given in Eq. (6.7). The left (right) panel illustrates the V (D_f) - dependence of the band structure.

On the left panel the the V -dependence is displayed for $D_f = 0$. The dispersive d-band hybridizes with the flat f-band, which leads to an avoided crossing and the formation of a band-gap with increasing V . Consequently, if the chemical potential lies within the gap, the system is insulating. The right panel illustrates the D_f -dependence for fixed $V = 0.4$. By increasing D_f , the upper band lowers at the

Γ -point, while the lower band rises at the Π -point. Therefore the band gap narrows with increasing D_f and vanishes entirely around $D_f \approx 0.2 - 0.3$.

6.2 DMFT

6.2.1 Method

In DMFT, the lattice Hamiltonian in Eq. (6.2) is mapped self-consistently onto a impurity model. The impurity model includes a local site, containing interacting d and f electrons, which are coupled to two non-interacting baths. Its Hamiltonian is given by:

$$H = H_{\text{imp}} + H_{\text{bath}} + H_{\text{hyb}} \quad (6.8)$$

$$\begin{aligned} H_{\text{imp}} = & (E_f - \mu) \sum_{\sigma} f_{\sigma}^{\dagger} f_{\sigma} + \frac{U}{2} n_f (n_f - 1) - \mu \sum_{\sigma} d_{\sigma}^{\dagger} d_{\sigma} \\ & + U_{df} n_f n_d + \sum_{\sigma} V (f_{\sigma}^{\dagger} d_{\sigma} + h.c.) \end{aligned} \quad (6.9)$$

$$H_{\text{bath}} = \sum_{\alpha, k, \sigma} E_{\alpha, k} b_{\alpha, k, \sigma}^{\dagger} b_{\alpha, k, \sigma} \quad (6.10)$$

$$H_{\text{hyb}} = \sum_{k, \sigma} V_k^{\alpha, \beta} (c_{\beta, \sigma}^{\dagger} b_{\alpha, \sigma, k} + h.c.). \quad (6.11)$$

Here $\alpha, \beta = d, f$ and $c_{d, \sigma} \equiv d_{\sigma}, c_{f, \sigma} \equiv f_{\sigma}$. The hybridization function

$$\Delta_{\alpha, \beta}(\omega) = \sum_{\gamma, k} \frac{V_k^{\alpha, \gamma} \bar{V}_k^{\beta, \gamma}}{\omega - E_{\gamma, k}} \quad (6.12)$$

is a matrix, which can not be diagonalized independently of ω because d and f electrons are not equivalent. Therefore, the DMFT self-consistency equations take matrix form. Solving the impurity model yields the self-energy matrix $\Sigma(\omega)$. The impurity and lattice Green's functions are given by:

$$\mathbf{G}_{\text{imp}}(\omega) = [\mathbf{G}_0^{-1}(\omega) - \mathbf{\Delta}(\omega) - \mathbf{\Sigma}(\omega)]^{-1}, \quad (6.13)$$

$$\mathbf{G}_{\text{latt}}(k, \omega) = [\mathbf{G}_0^{-1}(k, \omega) - \mathbf{\Sigma}(k, \omega)]^{-1}, \quad (6.14)$$

in which the non-interacting Green's functions read

$$\mathbf{G}_0(k, \omega) = \begin{pmatrix} \omega + \mu - \epsilon_{k, d} & -V \\ -V & \omega + \mu - E_f - \epsilon_{k, f} \end{pmatrix}^{-1}, \quad \mathbf{G}_0(\omega) = \begin{pmatrix} \omega + \mu & -V \\ -V & \omega + \mu - E_f \end{pmatrix}^{-1}. \quad (6.15)$$

It is convenient to define

$$M_d(\omega, k) = [\omega + \mu - \epsilon_{k, f} - \Sigma_d]^{-1}, \quad (6.16)$$

$$M_f(\omega, k) = [\omega + \mu - E_f - \epsilon_{k, f} - \Sigma_f]^{-1}. \quad (6.17)$$

Here the components of the self energy matrix

$$\mathbf{\Sigma}(k, \omega) = \begin{pmatrix} \Sigma_d(k, \omega) & \Sigma_{df}(k, \omega) \\ \Sigma_{fd}(k, \omega) & \Sigma_f(k, \omega) \end{pmatrix} \quad (6.18)$$

are used. Consequently, the momentum dependent lattice Greens function can be expressed as:

$$\begin{aligned} \mathbf{G}_{\text{latt}}(k, \omega) &= \begin{pmatrix} M_d^{-1} & -V - \Sigma_{df} \\ -V - \Sigma_{fd} & M_f^{-1} \end{pmatrix}^{-1} \\ &= \frac{1}{M_d^{-1}M_f^{-1} - (V + \Sigma_{df})(V + \Sigma_{fd})} \cdot \begin{pmatrix} M_f^{-1} & V + \Sigma_{df} \\ V + \Sigma_{fd} & M_d^{-1} \end{pmatrix} \\ &= \begin{pmatrix} [M_d^{-1} - (V + \Sigma_{df})(V + \Sigma_{fd})M_f]^{-1} & [M_d^{-1}M_f^{-1}(V + \Sigma_{df})^{-1} - (V + \Sigma_{fd})]^{-1} \\ [M_d^{-1}M_f^{-1}(V + \Sigma_{fd})^{-1} - (V + \Sigma_{df})]^{-1} & [M_f^{-1} - (V + \Sigma_{df})(V + \Sigma_{fd})M_d]^{-1} \end{pmatrix}. \end{aligned} \quad (6.19)$$

The k, ω dependence of $M_{d/f}(k, \omega) \equiv M_{d/f}$ and $\mathbf{\Sigma}(k, \omega) \equiv \mathbf{\Sigma}$ is not displayed explicitly for a less bulky expression. To obtain the local lattice Green's function, $\mathbf{G}_{\text{latt}}(k, \omega)$ is numerically integrated. The k -integration can be reduced to a one-dimensional energy integration with the DOS $\rho(\epsilon)$ of the cubic lattice:

$$\mathbf{G}_{\text{latt}}(\omega) = \int d\epsilon \rho(\epsilon) \mathbf{G}_{\text{latt}}(\epsilon, \omega). \quad (6.20)$$

Integrations are performed using the Tetrahedron method ([37][38][39]), which is implemented by Andreas Gleis. From the self-consistency equation $\mathbf{G}_{\text{latt}}(\omega) \stackrel{!}{=} \mathbf{G}_{\text{imp}}(\omega)$, the new hybridization function each DMFT iteration is extracted via:

$$\mathbf{\Delta}(\omega) = \mathbf{G}_0^{-1}(\omega) - \mathbf{\Sigma}(\omega) - \mathbf{G}_{\text{latt}}^{-1}(\omega). \quad (6.21)$$

We start our analysis by looking at the special cases in which either $t_f = 0$ or $U_{df} = 0$. For this purpose, simplifications can be made to reduce the computational cost.

Case $U_{df} = 0$:

Because the d electrons are non-interacting, they can be integrated out. Consequently, the SIAM can be used as a self-consistent impurity model, and the DMFT equation is solely formulated for the f-band. The f-component of lattice and impurity Green's function simplifies to:

$$G_{f,\text{latt}}(k, \omega) = \omega + \mu - E_f - \epsilon_{k,f} - \Sigma_f(k, \omega) - V^2(\omega + \mu - \epsilon_{k,d})^{-1}, \quad (6.22)$$

$$G_{f,\text{imp}}(\omega) = [\omega + \mu - E_f - \Delta_f(\omega) - \Sigma_f(\omega)]^{-1}. \quad (6.23)$$

Case $t_f = 0$:

If f electrons are not itinerant, only d electrons hybridize. As a result, the impurity model becomes

a single-band model. Furthermore, d- and f- components of lattice and impurity Green's function reduce to:

$$G_{f,\text{latt}}(k,\omega) = [\omega + \mu - E_f - \Sigma_f - (V + \Sigma_{df})(V + \Sigma_{fd})(\omega - \mu - \epsilon_k - \Sigma_d)^{-1}]^{-1}, \quad (6.24)$$

$$G_{d,\text{latt}}(k,\omega) = [\omega + \mu - \epsilon_k - \Sigma_d - (V + \Sigma_{df})(V + \Sigma_{fd})(\omega + \mu - E_f - \Sigma_f)^{-1}]^{-1}, \quad (6.25)$$

$$G_{f,\text{imp}} = [\omega + \mu - E_f - \Sigma_f - (V + \Sigma_{df})(V + \Sigma_{fd})(\omega + \mu - \Sigma_d - \Delta_d)^{-1}]^{-1}, \quad (6.26)$$

$$G_{d,\text{imp}} = [\omega + \mu - \Sigma_d - \Delta_d - (V + \Sigma_{df})(V + \Sigma_{fd})(\omega + \mu - E_f - \Sigma_f)^{-1}]^{-1}. \quad (6.27)$$

The self-consistency is only performed for the d-component, yielding the hybridization

$$\Delta_d(\omega) = \omega + \mu - \Sigma_d - (V + \Sigma_{df})(V + \Sigma_{fd})(\omega + \mu - E_f - \Sigma_f)^{-1} - G_{d,\text{loc}}^{-1}(\omega). \quad (6.28)$$

Numerical parameters:

For our NRG calculations we use $\Lambda = 4$ as discretization parameter. Single-band calculations (i.e. for $t_f = 0$) are performed keeping $N_k = 5000$ multiplets each NRG iteration. In two-band calculations $N_k = 4000$ multiplets are kept.

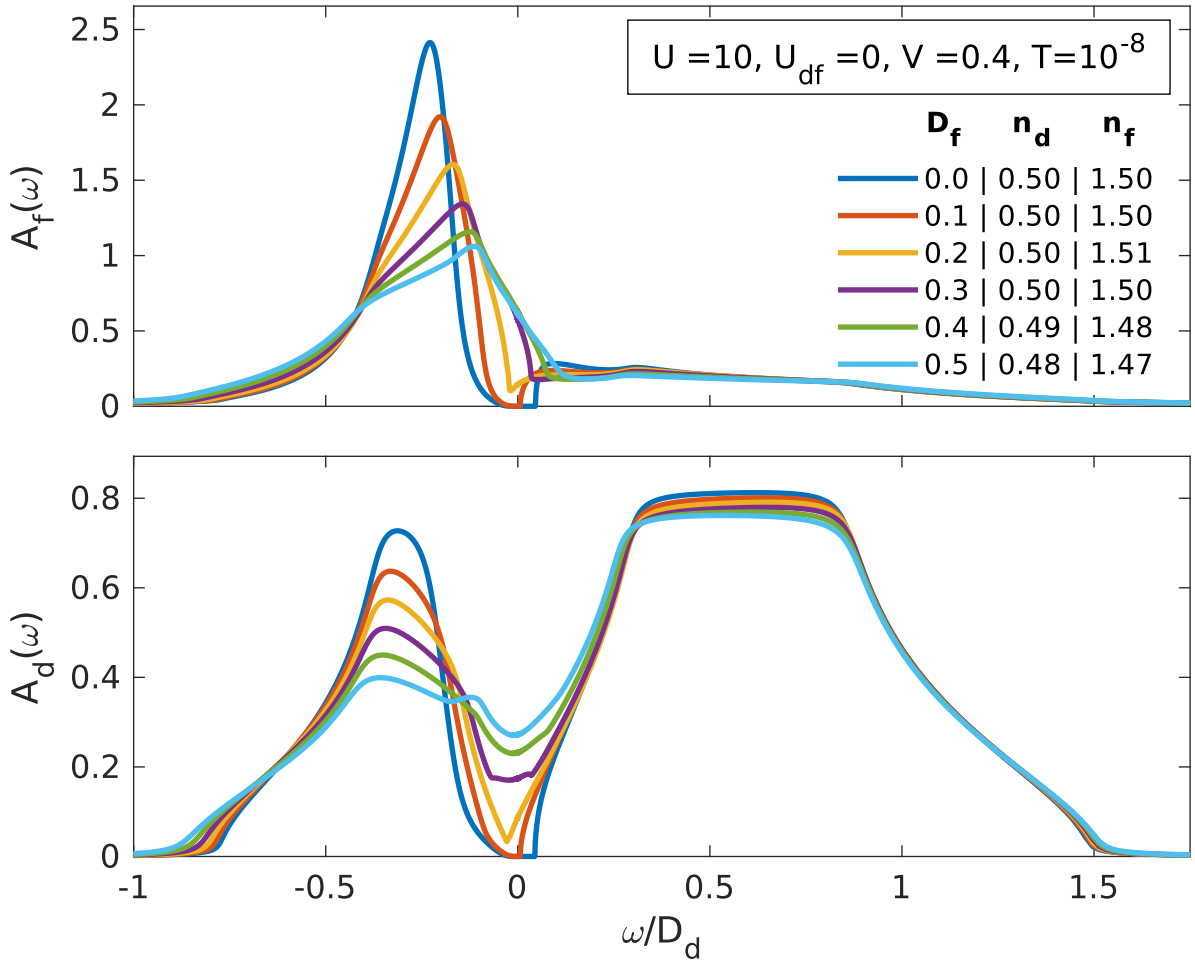


Fig. 6.2: Spectral functions $A_f(\omega)$ and $A_d(\omega)$ for $D_f \in [0, 0.5]$. Interaction parameters, chemical potentials and temperature are fixed to $U = 10$, $V = 0.4$, $E_f = 10.2$, $\mu = -0.4$, $T = 10^{-8}$. Moreover, the legend shows the d- and f-band occupation for each different D_f .

6.2.2 Mixed-valence regime, $U_{df} = 0$

First of all, we take a look at the edge case $U_{df} = 0$ and inspect the influence of the f-bandwidth D_f . We adjust the occupations to the mixed-valence regime $(n_d, n_f) \approx (0.5, 1.5)$ by setting $\mu = -0.4$, $E_f = -10.2$. In the following, spectral functions of d and f electrons, obtained from the converged DMFT solution, are analyzed. In Fig. 6.2, $A_f(\omega)$ and $A_d(\omega)$ are plotted for different values of D_f . At $D_f = 0$ the spectral functions are gapped at $\omega = 0$. Increasing D_f lifts the spectral gap, in accordance with the non-interacting bandstructure, discussed in Sec. 6.1. Note, $A_f(\omega)$ has a side peak around $\omega \approx E_f - \mu$, which we choose not to show.

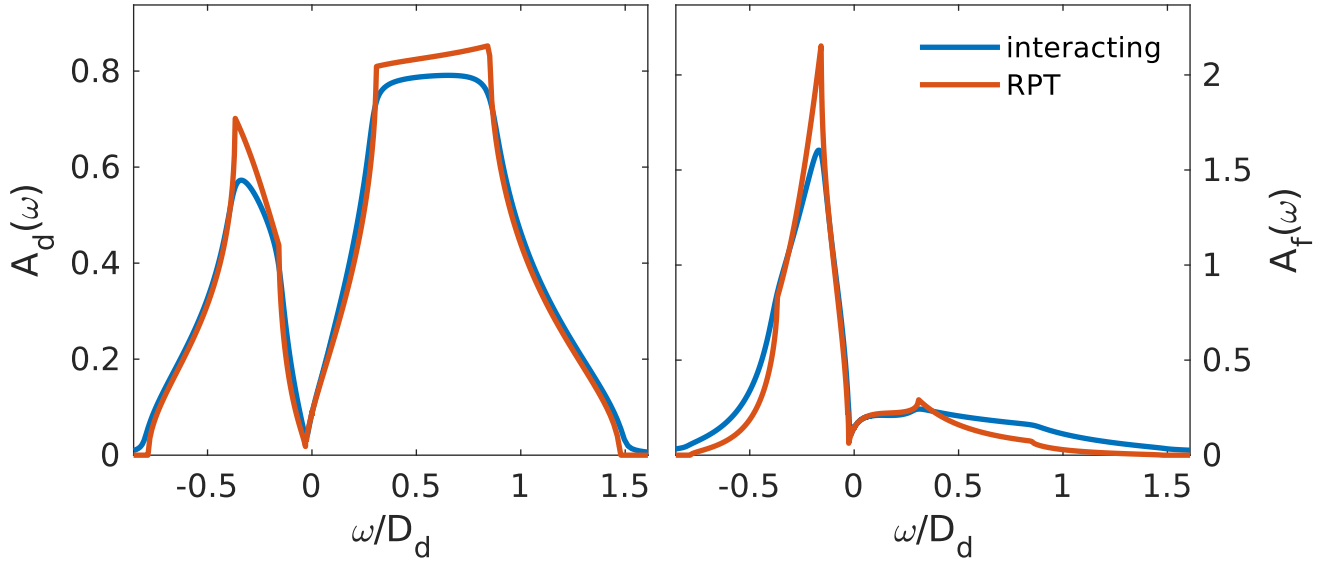


Fig. 6.3: Interacting spectral functions for $U = 10$, $V = 0.4$, $D_f = 0.2$, $T = 10^{-8}$, compared to non-interacting spectral functions with renormalized parameters, obtained by RPT.

To further investigate the effect of the interaction U , a renormalized perturbation theory (RPT) ([40],[41]) analysis is performed. RPT aims to model the low energy physics of impurity models such as the Anderson impurity model. In RPT the low energy physics is described by a weakly interacting quasi-particle Hamiltonian with renormalized parameters. From the finite size spectrum of the Fermi liquid fixed point of the NRG flow, one can calculate the renormalized parameters. In RPT the self-energy at $T = 0$ is written as:

$$\Sigma(\omega) = \Sigma(0) + \omega\Sigma'(0) + \Sigma^{\text{rem}}(\omega). \quad (6.29)$$

Resulting, the f-Green's function, given in Eq. (6.23), reads:

$$G_{f,\text{imp}}(\omega)^{-1} = z^{-1}[\omega + z(\mu - E_f - \Sigma(0)) - z\Delta(\omega) - z\Sigma^{\text{rem}}(\omega)]. \quad (6.30)$$

Neglecting $\Sigma^{\text{rem}}(\omega)$ yields the non-interacting Green's function with renormalized parameters, in which $z^{-1} = 1 - \Sigma'(0)$ is the quasi particle weight. The f-level is renormalized to $\mu - \tilde{E}_f = z(\mu - E_f - \Sigma(0))$. In the same spirit, we can also rewrite the renormalized lattice Greens function of the f electrons:

$$G_{f,\text{latt}}^{-1}(k, \omega) = z^{-1}[\omega + \mu - \tilde{E}_f - z\epsilon_{k,f} - zV^2(\omega + \mu - \epsilon_{k,d})^{-1}]. \quad (6.31)$$

The renormalization of $\Delta(\omega)$ corresponds to a renormalization of V and the f-dispersion $\epsilon_{k,f}$.

$D_f = 0.2$ is used to demonstrate the results of the RPT analysis. We find the quasi-particle weight $z = 0.654$ and $\mu - \tilde{E}_f = 0.08369$. In Fig. 6.3 the interacting spectral functions are compared to the non-interacting spectral functions with renormalized parameters.

In the low energy region around $\omega = 0$, the renormalized non-interacting solution follows the interacting solution precisely. Consequently, the Fermi liquid description of RPT is valid in the given parameter regime and the interaction U only renormalizes V, D_f and E_f .

6.2.3 Influence of the interaction U_{df}

The full Hamiltonian (6.2) is now considered using single-site DMFT and the effect of the interaction U_{df} is analyzed. We fix $D_f = 0.2$ and tune the interaction $U_{df} \in [0,1]$. The chemical potential μ and f-level E_f are adjusted with U_{df} , such that $\mu - U_{df} = -0.4$ and $-\mu + E_f = -9.8$. Consequently, the occupation numbers remain in the MV-regime $(n_d, n_f) \approx (0.5, 1.5)$. Fig. 6.4 shows the U_{df} -dependence of the spectral functions $A_f(\omega)$ and $A_d(\omega)$.

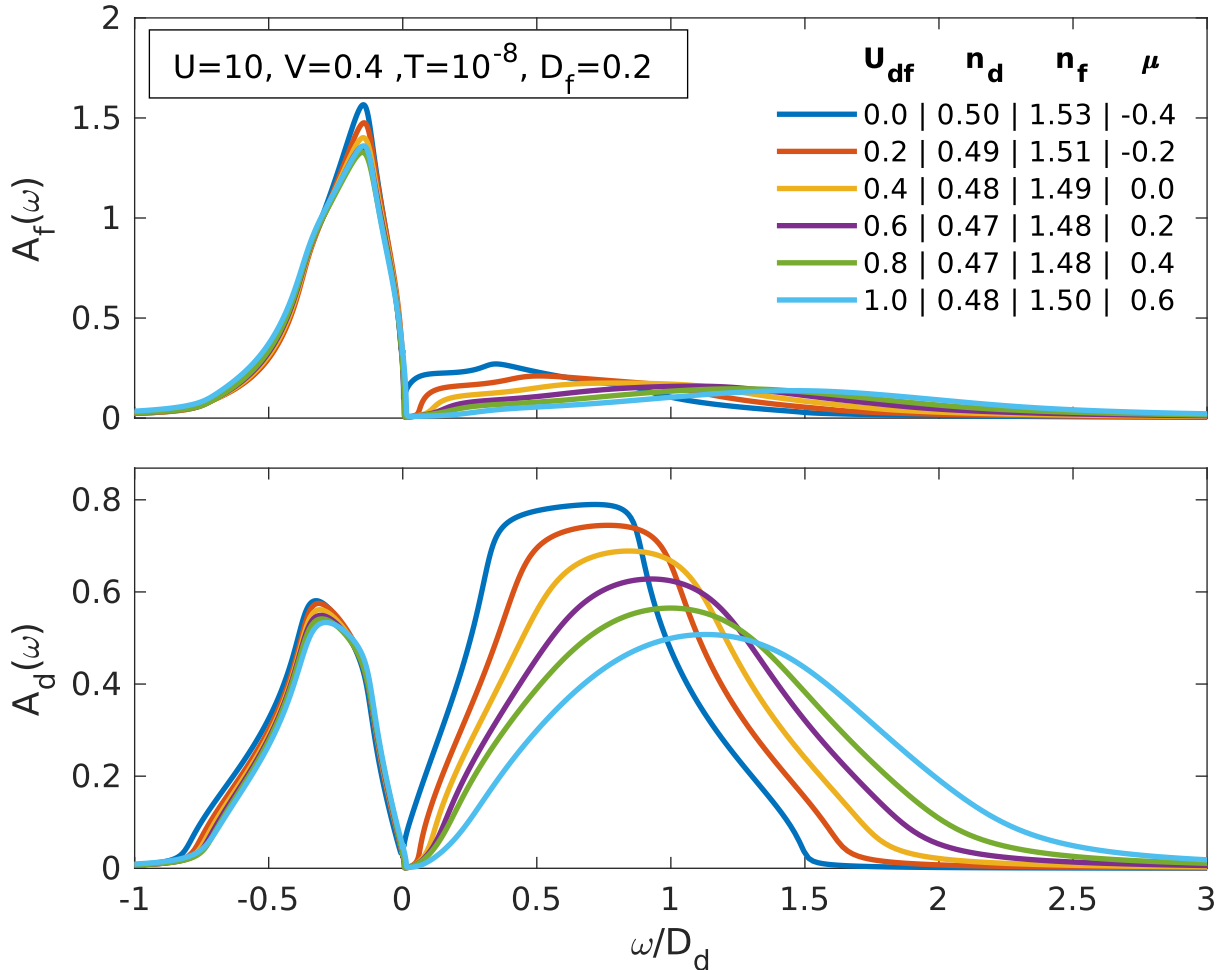


Fig. 6.4: Spectral functions $A_f(\omega)$ and $A_d(\omega)$ for $U_{df} \in [0, 1]$. The remaining parameters are fixed to $U = 10, V = 0.4, D_f = 0.2, T = 10^{-8}$. In addition, the legend shows the occupations and that the chemical potential is shifted with U_{df} . Note, we also tune E_f , s.t. $-\mu + E_f = -9.8$ is constant.

The finite spectral weight around $\omega = 0$ for $U_{df} = 0$ vanishes with increasing U_{df} and a spectral gap forms at positive ω in the f- and d-spectral function. Furthermore, the side peak position at positive ω shifts to the right. To analyze the shift in the peak position we decompose the annihilation operator of the d electrons d_σ into projections onto different charge quantum number sectors of f electrons. Analogously, we decompose f_σ into different d electron charge sectors. The decomposition is given by

$$d_\sigma = d_\sigma P_{n_f=0} + d_\sigma P_{n_f=1} + d_\sigma P_{n_f=2}, \quad (6.32)$$

$$f_\sigma = f_\sigma P_{n_d=0} + f_\sigma P_{n_d=1} + f_\sigma P_{n_d=2}, \quad (6.33)$$

in which $P_{n_{d/f}=q}$ indicates the projection on the states with occupation $n_{d/f} = q$, and $q = 0, 1, 2$. Using the decomposed operators, the spectral functions for d and f electrons is split into the different charge sectors, i.e. $A_{d,n_f=q}(\omega)$ and $A_{f,n_d=q}(\omega)$. The results for the decomposed spectral functions are shown in Fig. 6.5 (left) for $U_{df} = 1$ along with the side peak position of the decomposed spectral functions for $U_{df} \in [0, 1]$ (right).

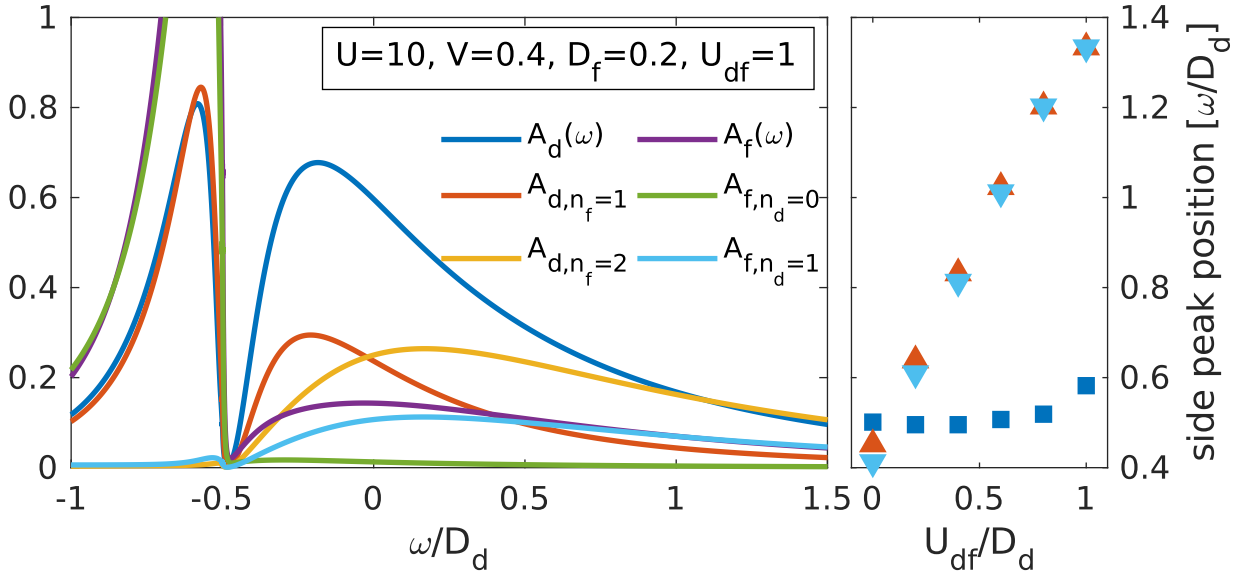


Fig. 6.5: Decomposition of spectral functions $A_d(\omega)$, $A_f(\omega)$ into different charge quantum number sectors $A_{d,n_f=q}(\omega)$, $A_{f,n_d=q}(\omega)$ ($q = 0, 1, 2$). On the left the decomposition of the spectral functions is shown. $A_{d,n_f=0}(\omega)$ and $A_{f,n_d=2}(\omega)$ are negligible small and therefore not presented. On the right side the U_{df} -dependence of the side peak position of $A_{d,n_f=1}(\omega)$, $A_{d,n_f=2}(\omega)$ and $A_{f,n_d=2}(\omega)$ are displayed, in which colors correspond to the spectral functions.

Hole excitations of $A_d(\omega)$ lie mainly in the sector of $n_f = 1$, while particle excitations consist out of two peaks for the sectors $n_f = 1, 2$. Note, the sector $n_f = 0$ is negligible small and therefore not displayed. On the right side of Fig. 6.5 the U_{df} -dependence of the peak position is displayed. The particle excitation peak for the $n_f = 1$ sector does not shift with U_{df} because μ is shifted by U_{df} , i.e. $-\mu + U_{df}$ remains constant. On the contrary, the peak in the $n_f = 2$ sector shifts linear in U_{df} because of the repulsive interaction $2U_{df}$ originating from the two present f electrons. On the other hand, $A_f(\omega)$ shows particle excitations mainly in the sector $n_d = 1$, which shift linearly with U_{df} , because $-\mu + E_f$ is kept constant. Altogether the decomposition indicates configurations, in which the impurity site is either occupied by a d and f electron or doubly occupied by only f electrons.

Moreover, the interaction U_{df} shifts excitations in $A_{d,n_f=2}(\omega)$ and $A_{f,n_d=1}(\omega)$ similar to a chemical potential.

Further insights into the gap formation can be obtained from the momentum dependent spectral function $A_{d+f}(k,\omega)$, which is displayed in Fig. 6.6. In the case $U_{df} = 0$, $A_{d+f}(k,\omega)$ shows two bands, as expected, since the interaction U only renormalizes the non-interacting bandstructure, as discussed in Sec. 6.2.2. The lower band at the Π -point overlaps with the upper band at the Γ -point. Increasing U_{df} shifts the upper band upwards, while the lower band position is unaffected. Resulting, a spectral gap is formed. Moreover, the upper band broadens with increasing U_{df} . The broadening originates from the imaginary part of the self-energy, which increases with increasing U_{df} , see Fig. 6.7. Because the spectral weight around the X - and Π -point originate from $A_d(k,\omega)$ and the spectral weight at the Γ -point has contributions from $A_f(k,\omega)$ and $A_d(k,\omega)$, the broadening width varies.

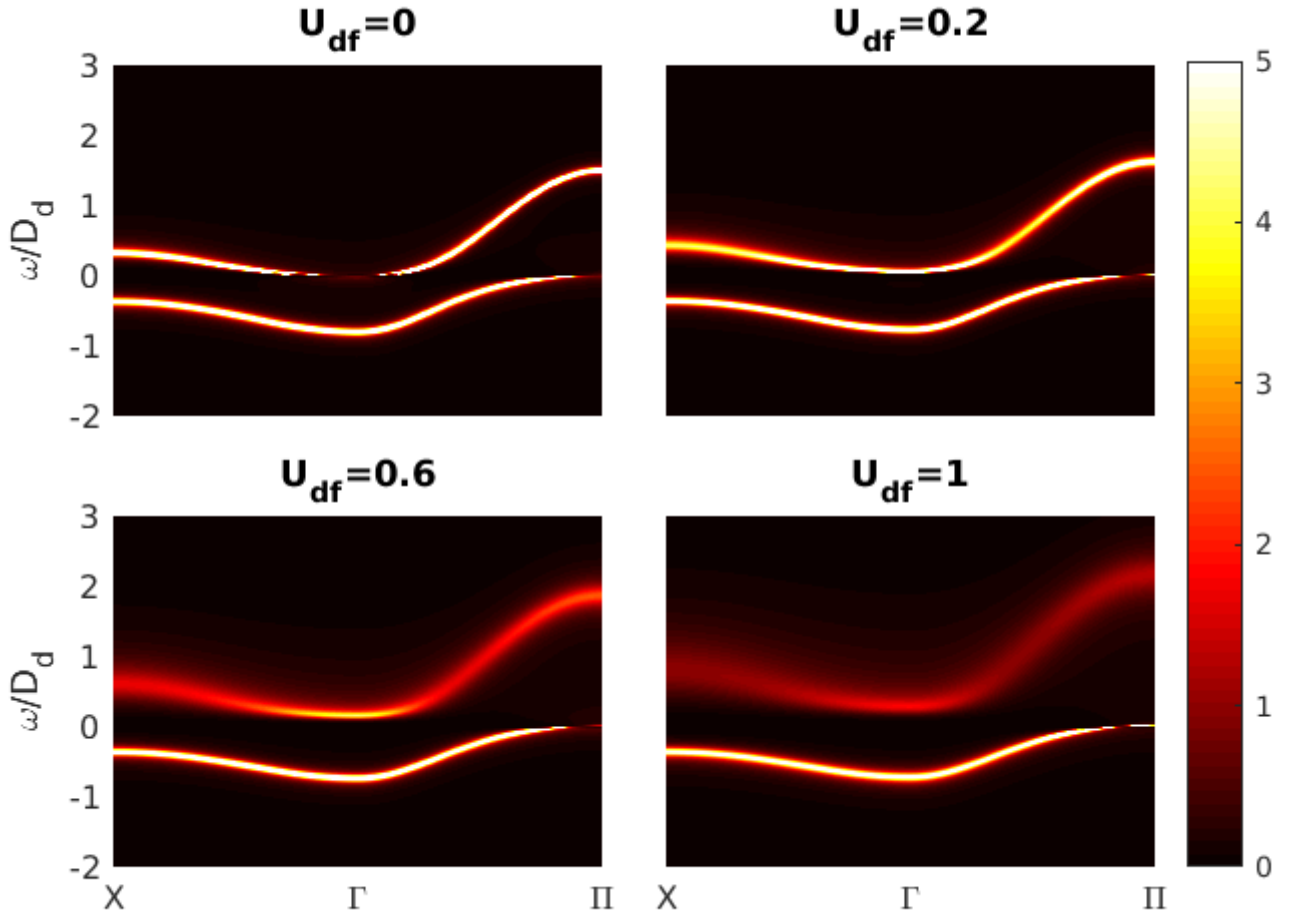


Fig. 6.6: Momentum dependent spectral function $A_{d+f}(k,\omega)$ for different values of U_{df} . The remaining parameters are fixed to $U = 10, V = 0.4, D_f = 0.2, T = 10^{-8}$.

Fig. 6.7, shows the imaginary part of the self-energies $\Sigma_f(\omega)$ and $\Sigma_d(\omega)$ corresponding to the spectral functions shown in Fig. 6.4. In general, the self-energies show only features at the position of the sidebands of the corresponding spectral functions and decay to zero for low energies. The f-band self-energy shows a peak at negative $\omega \approx -E_f$ corresponding to the single f electron bound state. A smaller peak at positive $\omega \approx 1$ is visible, related to the double occupied f-state, which increases with

increasing U_{df} . $\text{Im}[\Sigma_d(\omega)]$ is relatively small compared to $\text{Im}[\Sigma_f(\omega)]$ and shows some numerical error at $U_{df} = 0$, as it should be zero in this case. However, the magnitude of the error is small compared to $\text{Im}[\Sigma_d(\omega)]$ and should not affect the overall results. The height of the right side peak increases with increasing U_{df} , in accordance with the broadening of $A_{d+f}(k, \omega)$ in Fig. 6.6. Note, $\Sigma_{df}(\omega)$, shows similar behavior as $\Sigma_f(\omega)$ and $\Sigma_d(\omega)$ and is therefore not presented.

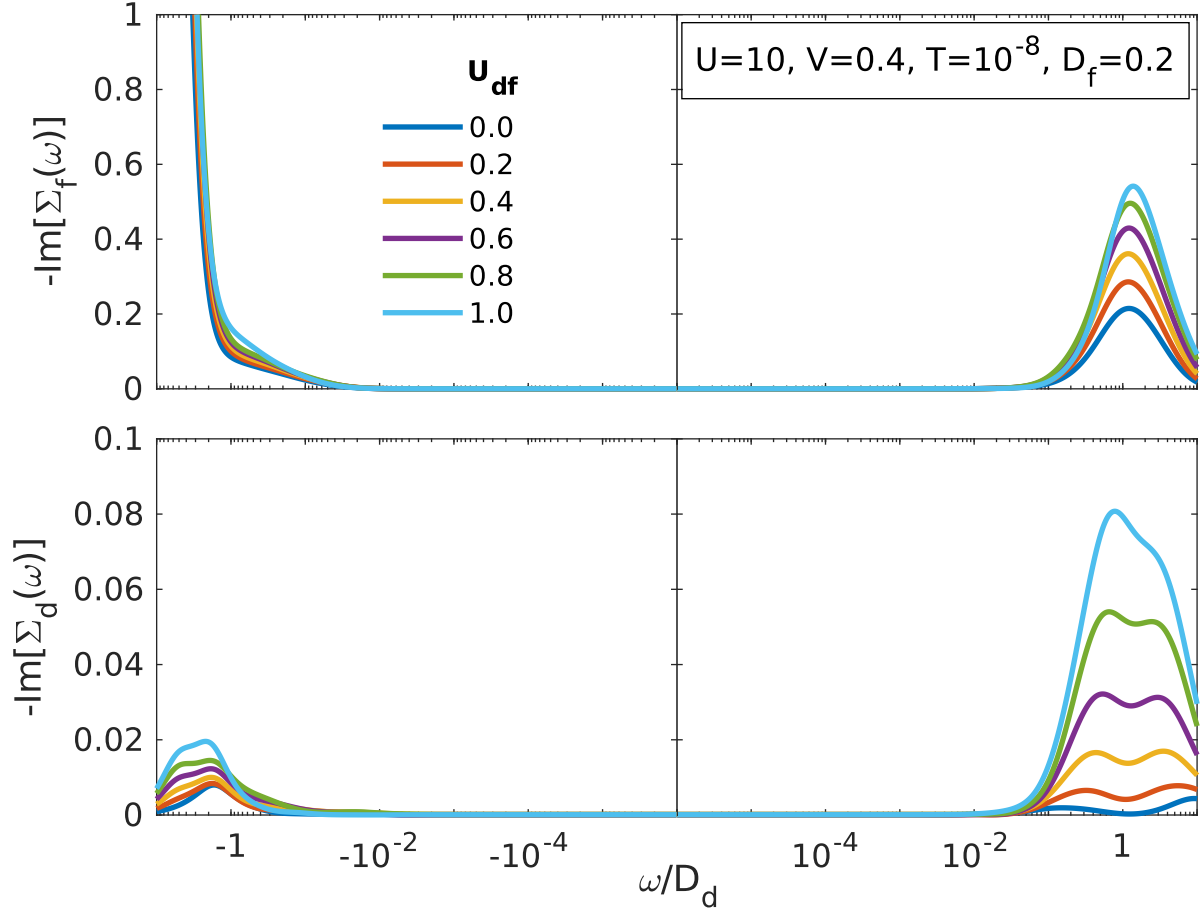


Fig. 6.7: Imaginary parts of d- and f-band self-energies and their U_{df} -dependence. The remaining parameters are fixed to $U = 10, V = 0.4, D_f = 0.2, T = 10^{-8}$.

6.2.4 Metal-insulator transition and dynamical susceptibilities

In the following we consider a small deviation from the case with $U_{df} = 1$ and tune the metallic state to an insulating state, in which the spectral gap is centered around $\omega = 0$. By keeping $\mu = 0.6$ and $\mu - E_f = -9.8$ constant and decreasing U_{df} , the gap position shifts towards $\omega = 0$. For $U_{df} \approx 0.945 - 0.955$, the transition between metallic and insulating state can be observed. In Fig. 6.8 spectral functions in the transition region are displayed. The spectral gap at $U_{df} = 0.955$ shifts to $\omega = 0$ for $U_{df} = 0.945$.

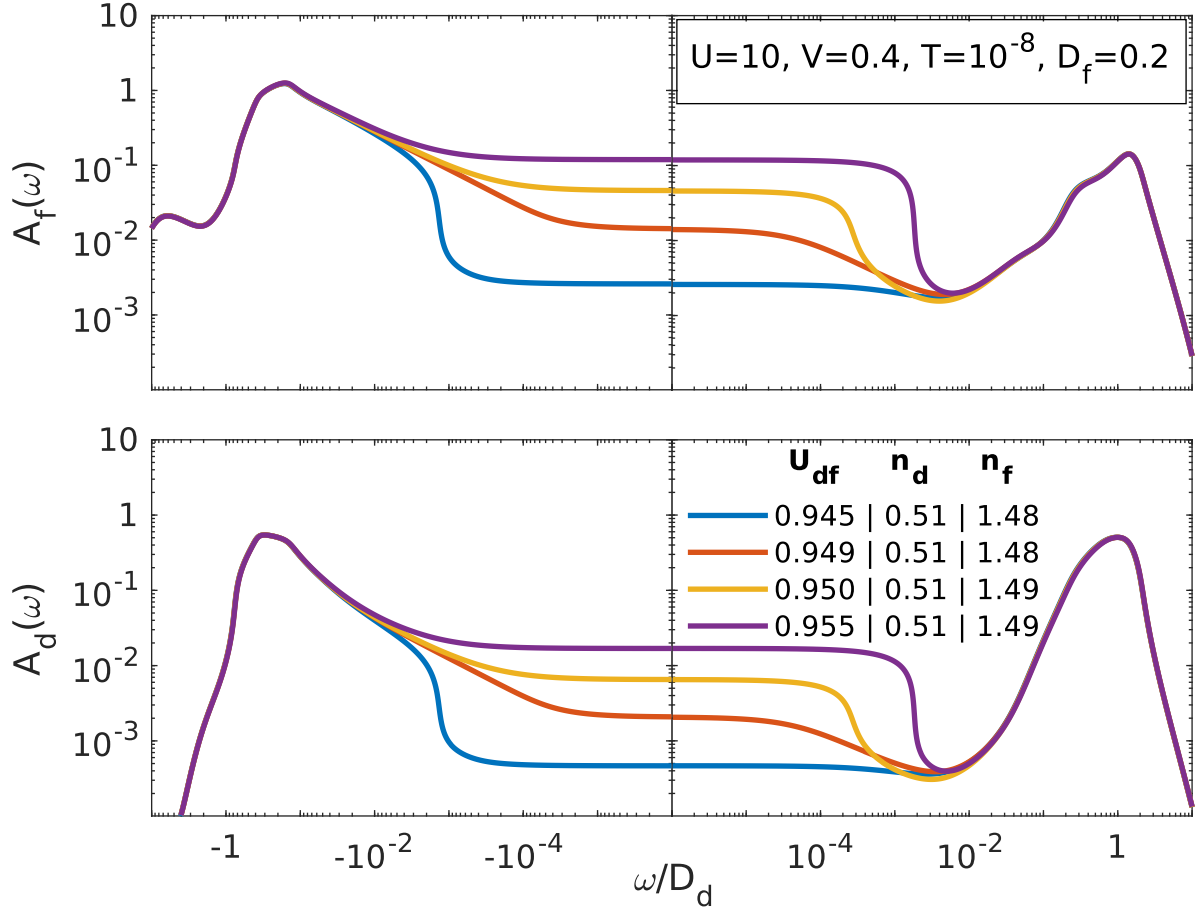


Fig. 6.8: Spectral functions for $U_{df} = 0.945 - 0.955$ in log-log scale. Chemical potentials are fixed to $\mu = 0.6, E_f = 9.2$ and the remaining parameters are set to $U = 10, V = 0.4, D_f = 0.2, T = 10^{-8}$. The legend shows the fillings corresponding to the different values of U_{df} .

To check if the different occurring states show signs for the formation of composite neutral fermions dynamical susceptibilities are calculated. Dynamical susceptibilities $\chi''_{A,B}(\omega)$ are defined via:

$$\langle A||B \rangle_t = -\theta(t)\langle [A(t), B^\dagger] \rangle, \quad (6.34)$$

$$\langle A||B \rangle_\omega = \int d\omega \langle A||B \rangle_t e^{-i\omega t}, \quad (6.35)$$

$$\chi''_{A,B}(\omega) = -\frac{1}{\pi} \text{Im}(\langle A||B \rangle_\omega). \quad (6.36)$$

In Fig. 6.9 charge- and spin-susceptibilities are shown, corresponding to the spectral functions plotted in Fig.6.8. The overall structure is similar throughout the different susceptibilities, featuring a broad peak around $\omega \approx 10^{-1}$, followed by a rapid decay as the gap in the spectral function opens. Between $\omega \approx 10^{-4} - 10^{-2}$, a cross-over to a linear decay is visible. For smaller values of U_{df} , the slope of the cross-over is larger and the susceptibilities decay faster, following the shift of the spectral gap towards $\omega = 0$ for decreasing U_{df} . The linear decay from $\omega \approx 10^{-4}$ on, indicates Fermi liquid behavior.

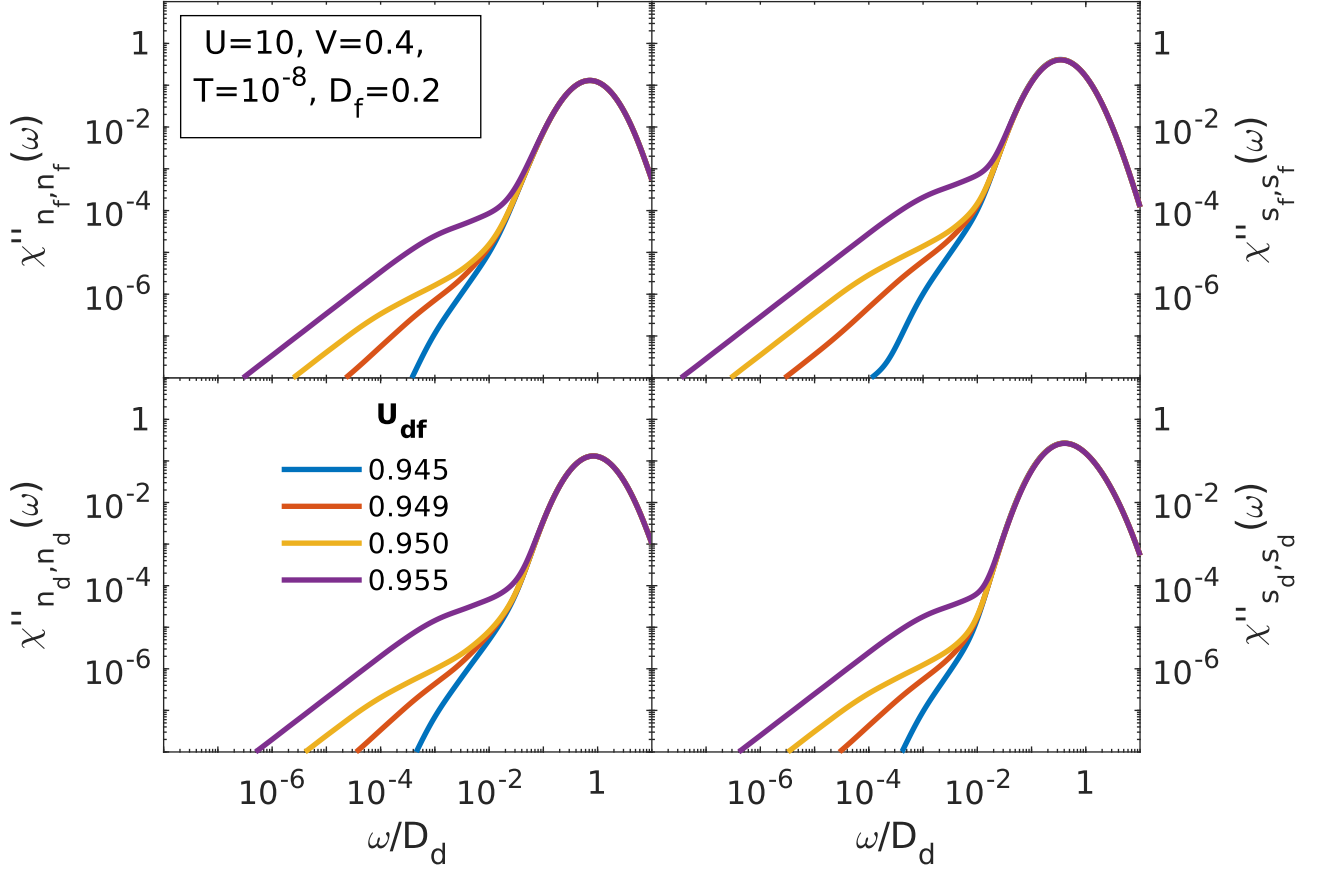


Fig. 6.9: Dynamical charge- and spin-susceptibilities $\chi''_{n_f, n_f}(\omega)$, $\chi''_{n_d, n_d}(\omega)$, $\chi''_{s_f, s_f}(\omega)$, $\chi''_{s_d, s_d}(\omega)$ for $U_{df} = 0.945 - 0.955$ in log-log scale. Chemical potentials are fixed to $\mu = 0.6$, $E_f = 9.2$ and the remaining parameters are set to $U = 10$, $V = 0.4$, $D_f = 0.2$, $T = 10^{-8}$.

Moreover, we calculate correlation functions between d- and f-charge and spin, $\chi''_{n_d, n_f}(\omega)$, $\chi''_{s_d, s_f}(\omega)$. Motivated by the composite exciton operator $\psi_{k, \sigma} = b_k d_{k, \sigma}$, we further calculate $\chi''_{d^\dagger, f}^{[Q, S]}(\omega)$, in which the operators are restricted to the quantum number sectors $[Q, S] = [0, 0]; [0, 2]$, whereat Q denotes the total charge and S the total spin quantum number. A comparison of the above mentioned susceptibilities is presented in Fig. 6.10 along with d- and f-spectral function for $U_{df} = 0.95$. The general structure of $\chi''_{d^\dagger, f}^{[Q, S]}(\omega)$ is similar to the charge- and spin-susceptibilities discussed earlier in Fig. 6.9. The direct comparison with $A_f(\omega)$, $A_d(\omega)$ shows again that the suppression of the susceptibilities is associated with the opening of the spectral gap and the cross-over region to a linear decay spans over the region of the gap. Furthermore, $\chi''_{s_d, s_f}(\omega)$ shows anti-correlation between d- and f-spins, whereat the anti-correlation of d- and f-charge changes sign when the spectral gap opens, illustrated by $\chi''_{n_d, n_f}(\omega)$.

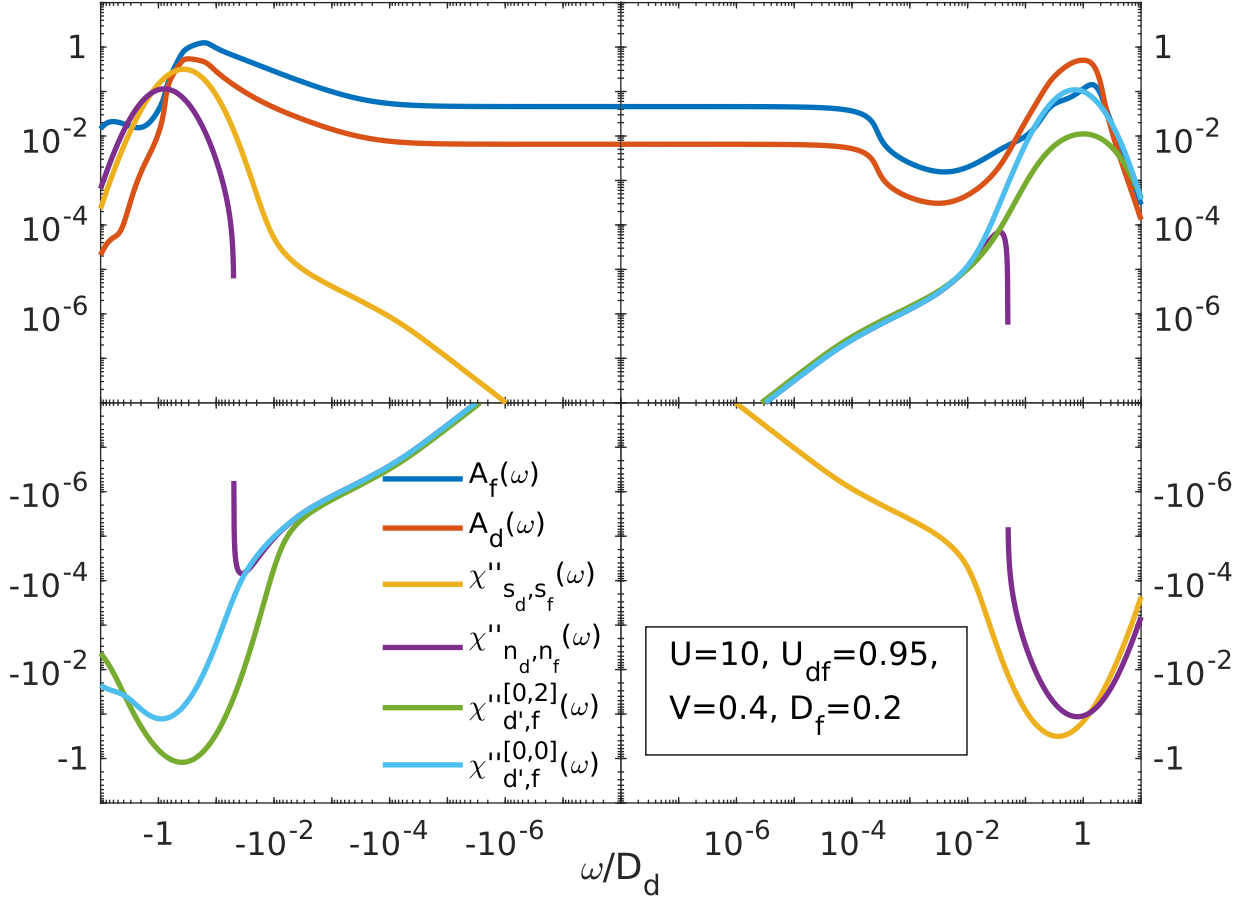


Fig. 6.10: Dynamical susceptibilities $\chi_{d,f}^{[Q,S]}(\omega)$, χ_{n_d, n_f}'' , χ_{s_d, s_f}'' and spectral functions $A_d(\omega)$, $A_f(\omega)$ for $U_{df} = 0.95$. Chemical potentials are fixed to $\mu = 0.6$, $E_f = 9.2$ and the remaining parameters are set to $U = 10$, $V = 0.4$, $D_f = 0.2$, $T = 10^{-8}$.

Altogether, the various calculated susceptibilities inherit their overall behavior from the formation of the spectral gap and show no further signatures of a bound state between d electron and f-holon. If a bonding between d electrons and f-holons were present, the general structure of $\chi_{n_d, n_f}''(\omega)$ would deviate from $\chi_{s_d, s_f}''(\omega)$, as the charge degree of freedom would decouple and bond with the d electron.

Furthermore, our previously discussed results for the U_{df} -dependence of the spectral functions, do not show signs for a composite exciton either. The decomposition of the spectral functions and the momentum-dependent spectral function indicates that the upper band of the renormalized bandstructure at $U_{df} = 0$ is simply shifted by the repulsive interaction U_{df} . Moreover, the self-energy does not show any special features, which could indicate a bound state between d electron and f-hole. We conclude that our DMFT calculations support a rather simple picture of a non-interacting bandstructure renormalized by the interactions U and U_{df} . Possible electronic configurations are hybridized d and f electrons or sites doubly occupied by f electrons without d electrons, resulting in an average occupation of $(n_d, n_f) \approx (0.5, 1.5)$. On the lattice level, both of these configurations can coexist and possibly form an alternating pattern.

6.2.5 Transport properties

In the following, we calculate the optical conductivity $\sigma(\omega)$ and DC resistivity ρ_{xx} based on our DMFT results. We consider four different values of U_{df} , corresponding to the different phases in the metal-insulator transition. Furthermore, we make a comparison to experimental measurements on SmB₆. Formulas for the optical conductivity and resistivity are adapted from ([42], [43]) and given by

$$\sigma_{\alpha,\beta}(\omega) = 2\pi e^2 \int d\omega' \int d\epsilon \Phi_{xx,\alpha,\beta}(\epsilon) \left[\frac{f(\omega',T) - f(\omega' + \omega,T)}{\omega} \right] A_{\alpha,\beta}(\epsilon,\omega') A_{\alpha,\beta}(\epsilon,\omega' + \omega), \quad (6.37)$$

$$\Phi_{xx,\alpha,\beta}(\epsilon) = \int \frac{dk}{(2\pi)^3} (\partial_{k_x} \epsilon_{k,\alpha}) (\partial_{k_x} \epsilon_{k,\beta}) \delta(\epsilon - \epsilon_{k,\alpha}), \quad (6.38)$$

$$\sigma(\omega) = \sigma_{d,d}(\omega) + \sigma_{f,f}(\omega) + \sigma_{d,f}(\omega), \quad (6.39)$$

$$\sigma_{xx} = \lim_{\omega \rightarrow 0} \sigma(\omega), \quad \rho_{xx} = 1/\sigma_{xx}, \quad (6.40)$$

in which $\alpha,\beta = d, f$. Temperature dependence is introduced through the Fermi function $f(\omega,T) = 1/(1+e^{\omega/T})$ and the self-energy, whose imaginary part is shown for $U_{df} = 0.945$ in Fig. 6.11. The height of $-\text{Im}[\Sigma_{d/f}(\omega)]$ at the Fermi level decreases with decreasing temperature until it saturates around $T \approx 0.0046$. Note, $\Sigma_{df}(\omega)$ shows similar temperature dependence and is therefore not displayed here.

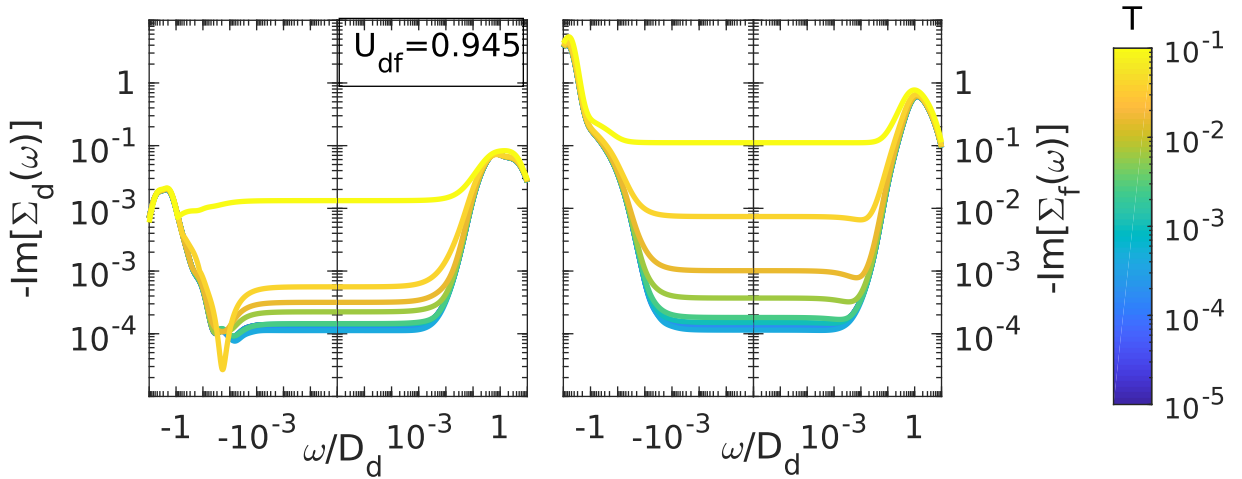


Fig. 6.11: Temperature dependence of $\text{Im}[\Sigma_d(\omega)]$, $\text{Im}[\Sigma_f(\omega)]$ for $T = 10^{-5} - 10^{-1}$ and $U_{df} = 0.945$.

In Fig. 6.12 results of the temperature dependent resistivity are compared to experimental data. In experiments, the resistivity exhibits an increase with decreasing temperature and saturates in a plateau. Our calculations show an decreasing resistivity for $T/D_d = 0.0464 \searrow 0.0046$ for all four values of U_{df} . Afterward, for $T = 0.0046 \searrow 10^{-4}$ the resistivity saturates for $U_{df} = 0.955$, whereas for $U_{df} = 0.945, 0.949, 0.95$ it increases with decreasing temperature, and saturates below $T < 10^{-4}$. The slope is much higher for $U_{df} = 0.945$, which agrees with the metal-insulator transition observed in Fig. 6.8, since for lower U_{df} the insulating state is reached, and therefore the resistivity should increase. Overall, the increase of resistivity for $T/D_d = 0.0046 \searrow 10^{-4}$, which saturates at low T , agrees with experimental observations.

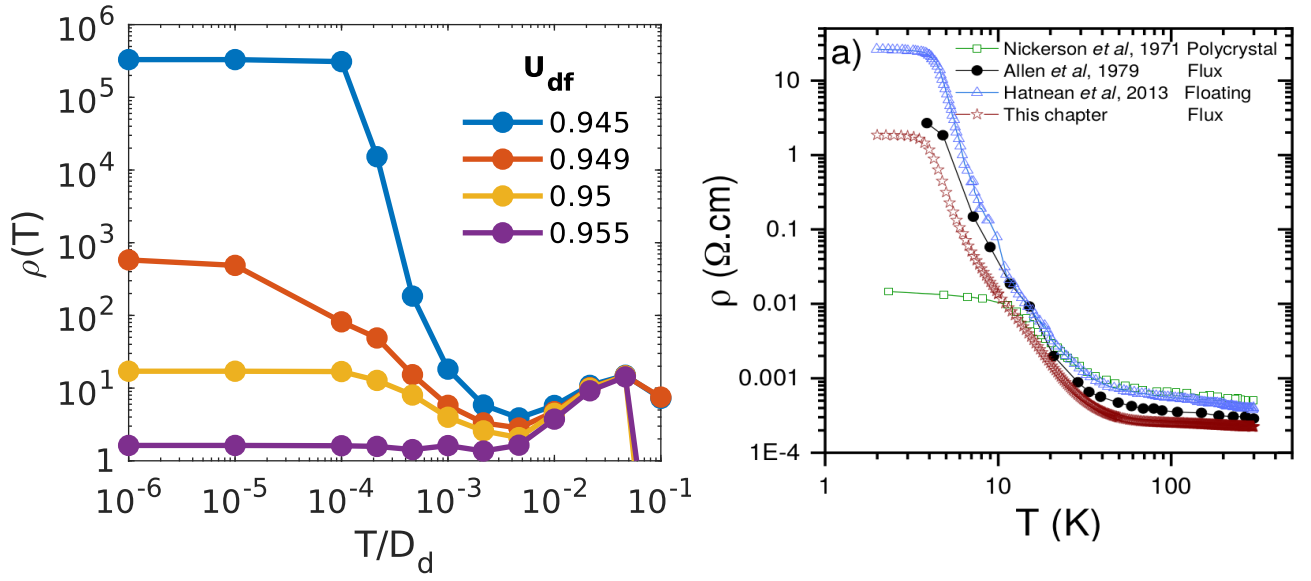


Fig. 6.12: Comparison of temperature dependent resistivity from DMFT calculations (left) and experimental measurements (right). The left panel displays the resistivity for different values of U_{df} . The right panel is taken from [33] and shows experimental results of the resistivity.

At low temperatures ($T < 5K$) measurements on SmB_6 ([24],[25]) indicate a substantial optical conductivity at finite frequencies, larger than the DC conductivity. Increasing temperature to $T \approx 20K$, leads to a cross-over to a metallic Drude-like response, i.e. $\sigma(\omega)$ decreases for decreasing ω . For reference see Fig. 3 & 4 in [24] and Fig. 2 (c) in [25].

Fig. 6.13 displays our results for the optical conductivity $\sigma(\omega)$ for each value of U_{df} and the temperatures $T = 10^{-4} - 0.046$. Interestingly for $U_{df} = 0.945$ and $T = 10^{-4}$, $\sigma(\omega)$ starts to increase at $\omega \approx 10^{-3}$, followed by a short plateau. Subsequently, the optical conductivity increases rapidly again. This can be qualitatively understood from the formula for the optical conductivity given in Eq. (6.37) and the spectral functions (for $T = 10^{-8}$) displayed in Fig. 6.8 as a reference for the gap position. The self-energy is almost temperature independent below $T \approx 0.0046$, hence the temperature dependence is governed solely by $f(\omega, T)$ for smaller T . The difference quotient of the Fermi function $\tilde{f}(\omega, \omega', T) = \frac{f(\omega', T) - f(\omega' + \omega, T)}{\omega}$ defines the frequency region in which the product $A_{\alpha, \beta}(\epsilon, \omega') A_{\alpha, \beta}(\epsilon, \omega' + \omega)$ contributes to the conductivity. For $\omega \lesssim 10^{-3}$, $\tilde{f}(\omega, \omega', T)$ only picks up contributions inside the spectral gap, resulting in a minimum at low frequencies. This is also the reason for the resistivity saturation for $U_{df} = 0.945$ below $T = 10^{-4}$. Increasing ω further, $\tilde{f}(\omega, \omega', T)$ extends into the band and products of $A_{\alpha, \beta}(\epsilon, \omega') A_{\alpha, \beta}(\epsilon, \omega' + \omega)$ contribute, in which ω' lies in the band, while $\omega' + \omega$ is positioned in the gap. Consequently a plateau is formed, followed by a rapid increase as soon as frequencies $\omega' + \omega$ also lie in the band.

At intermediate temperatures the low-frequency behavior changes into a maximum at $\omega = 0$ and a decrease with increasing ω , saturating in the same previously mentioned plateau. Reason being that $\tilde{f}(\omega = 10^{-6}, \omega', T)$ extends into the band for higher temperatures. The plateau turns into a minimum for larger values of T which has a similar origin as the plateau for $T = 10^{-4}$.

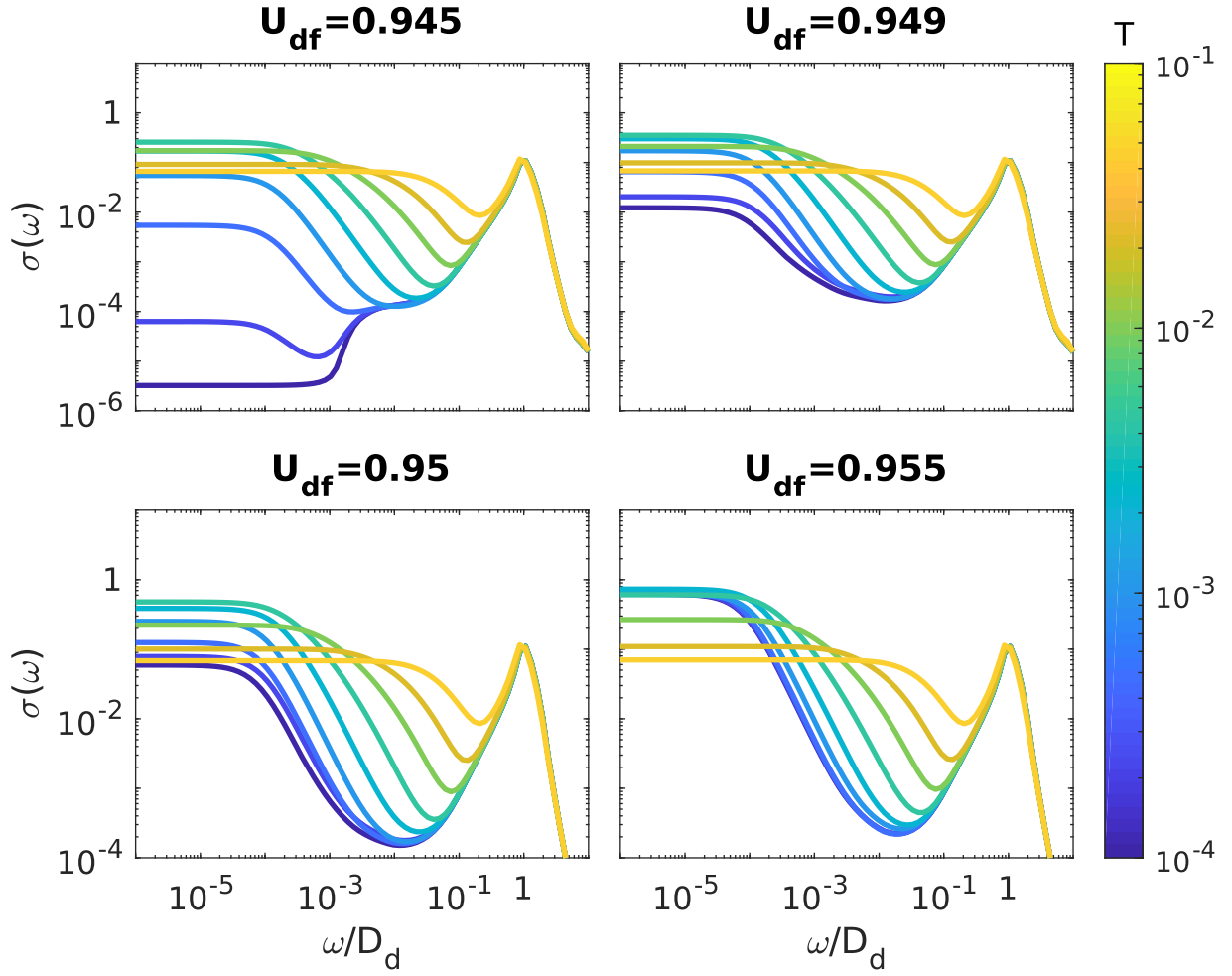


Fig. 6.13: Optical conductivity $\sigma(\omega)$ for temperatures $T = 10^{-4} - 0.0464$, calculated via Eq. (6.37). Each panel represents a different value of U_{df} .

For larger values of $U_{df} = 0.949, 0.95, 0.955$ the above-mentioned cross-over from low to high temperatures does not occur, since the spectral gap is located at finite frequencies and does not extend to $\omega = 0$. The overall behavior is similar throughout the three values of U_{df} . $\sigma(\omega)$ is maximal at $\omega = 0$ and decreases into a minimum, associated with the bandgap at finite frequencies. Solely the magnitude of the $\sigma(\omega = 0)$ varies, as displayed in Fig. 6.12 for the resistivity $\rho = 1/\sigma(\omega = 0)$.

Concluding, the optical conductivity for $U_{df} = 0.945$ at $T = 10^{-4}$ exhibits an insulating response with enhanced conductivity for finite ω . Increasing temperature leads to a cross-over to a Drude-like response, which shows qualitative similarities to experimental results on SmB_6 .

6.3 DCA

6.3.1 Method

Since DCA is carried out in momentum space, the Hamiltonian (6.2) is given in its momentum space representation:

$$\begin{aligned}
H = & \sum_{k,\sigma} [(\epsilon_{k,d} - \mu) d_{k,\sigma}^\dagger d_{k,\sigma} + (\epsilon_{k,f} + E_f - \mu) f_{k,\sigma}^\dagger f_{k,\sigma} + V(f_{k,\sigma}^\dagger d_{k,\sigma} + h.c.)] \\
& + U \sum_{k_1, k_2, q} f_{k_1+q, \sigma}^\dagger f_{k_2+q, \bar{\sigma}}^\dagger f_{k_2, \bar{\sigma}} f_{k_1, \sigma} \\
& + U_{df} \sum_{k_1, k_2, q, \sigma, \sigma'} f_{k_1+q, \sigma}^\dagger d_{k_2+q, \sigma'}^\dagger d_{k_2, \sigma'} f_{k_1, \sigma}.
\end{aligned} \tag{6.41}$$

In the following, the DCA self-consistency equations are presented for the cases $U_{df} \neq 0, t_f = 0$ and $U_{df} = 0, t_f \neq 0$. The Brillouin zone is split into N_c momentum patches \mathcal{P}_i , with $i = 1, \dots, N_c$. For our analysis $N_c = 2$ patches are used.

Cluster and lattice Green's functions, used in the self-consistency equations, are calculated. Because the Green's functions are diagonal in the cluster momenta K_i , their structure is similar to DMFT equations presented in Sec. 6.2.1, except that the self-energy and hybridization function now depends on K_i .

Case $U_{df} \neq 0, t_f = 0$:

In case of $t_f = 0$ only the d electrons couple to the bath. The corresponding cluster Hamiltonian reads:

$$H = H_{\text{cl}} + H_{\text{bath}} + H_{\text{hyb}} \tag{6.42}$$

$$\begin{aligned}
H_{\text{cl}} = & \sum_{i,\sigma} [(\epsilon_{K_i} - \mu) d_{K_i,\sigma}^\dagger d_{K_i,\sigma} + (E_f - \mu) f_{K_i,\sigma}^\dagger f_{K_i,\sigma} + V(f_{K_i,\sigma}^\dagger d_{K_i,\sigma} + h.c.)] \\
& + U \sum_{i,j,l} f_{K_i+Q_l, \sigma}^\dagger f_{K_j+Q_l, \bar{\sigma}}^\dagger f_{K_j, \bar{\sigma}} f_{K_i, \sigma} \\
& + U_{df} \sum_{i,j,l,\sigma,\sigma'} f_{K_i+Q_l, \sigma}^\dagger d_{K_j+Q_l, \sigma'}^\dagger d_{K_j, \sigma'} f_{K_i, \sigma}
\end{aligned} \tag{6.43}$$

$$H_{\text{bath}} = \sum_{i,\lambda,\sigma} \epsilon_{i,\lambda} b_{i,\lambda,\sigma}^\dagger b_{i,\lambda,\sigma} \tag{6.44}$$

$$H_{\text{hyb}} = \sum_{i,\lambda,\sigma} V_{i,\lambda} (d_{K_i,\sigma}^\dagger b_{i,\lambda,\sigma} + h.c.) \tag{6.45}$$

$$\epsilon_{K_i} = \frac{1}{\mathcal{V}(\mathcal{P}_i)} \sum_k \chi_{\mathcal{P}_i}(k) \epsilon_{k,d}. \tag{6.46}$$

Here χ is the indicator function, i.e. $\chi_{\mathcal{P}_i}(k) = 1$ if $k \in \mathcal{P}_i$ and $\chi_{\mathcal{P}_i}(k) = 0$ if $k \notin \mathcal{P}_i$. The cluster Green's functions reads:

$$\mathbf{G}_{\text{cl}}(K_i, \omega) = \begin{pmatrix} \omega + \mu - E_f - \Sigma_f(K_i, \omega) & -V - \Sigma_{df}(K_i, \omega) \\ -V - \Sigma_{fd}(K_i, \omega) & \omega + \mu - \epsilon_{K_i} - \Delta_d(K_i, \omega) - \Sigma_d(K_i, \omega) \end{pmatrix}^{-1}. \tag{6.47}$$

Inverting the matrix yields the d- and f- components of the Green's function:

$$G_{f,\text{cl}}(K_i, \omega) = [\omega + \mu - E_f - \Sigma_f - (V + \Sigma_{df})(V + \Sigma_{fd})(\omega + \mu - \epsilon_{K_i} - \Sigma_d - \Delta_d)^{-1}]^{-1}, \quad (6.48)$$

$$G_{d,\text{cl}}(K_i, \omega) = [\omega + \mu - \epsilon_{K_i} - \Sigma_d - \Delta_d - (V + \Sigma_{df})(V + \Sigma_{fd})(\omega + \mu - E_f - \Sigma_f)^{-1}]^{-1}. \quad (6.49)$$

Note, that $\Sigma = \Sigma(K_i, \omega)$ and the hybridization function $\Delta_d(K_i, \omega) = \sum_k \frac{V_{i,\lambda}^2}{\omega - \epsilon_{i,\lambda}}$ are functions of ω and the cluster momentum K_i . For the sake of a less bulky expression we will not display this dependence sometimes.

In the same way, f-/d-component of the lattice Green's function $\mathbf{G}_{\text{latt}}(k, K_i, \omega)$ can be expressed as:

$$G_{f,\text{latt}}(k, K_i, \omega) = [\omega + \mu - E_f - \Sigma_f - (V + \Sigma_{df})(V + \Sigma_{fd})(\omega + \mu - \epsilon_k - \Sigma_d)^{-1}]^{-1}, \quad (6.50)$$

$$G_{d,\text{latt}}(k, K_i, \omega) = [\omega + \mu - \epsilon_k - \Sigma_d - (V + \Sigma_{df})(V + \Sigma_{fd})(\omega + \mu - E_f - \Sigma_f)^{-1}]^{-1}. \quad (6.51)$$

Case $U_{df} = 0$:

In case of no interaction between d and f electrons, d electrons can be integrated out. The corresponding cluster Hamiltonian reads:

$$H = H_{\text{cl}} + H_{\text{bath}} + H_{\text{hyb}} \quad (6.52)$$

$$H_{\text{cl}} = \sum_{i,\sigma} [\epsilon_{K_i} + E_f - \mu] f_{k_i,\sigma}^\dagger f_{K_i,\sigma} + U \sum_{i,j,l} f_{K_i+Q_l,\sigma}^\dagger f_{K_j+Q_l,\bar{\sigma}}^\dagger f_{K_j,\bar{\sigma}} f_{K_i,\sigma} \quad (6.53)$$

$$H_{\text{bath}} = \sum_{i,\lambda,\sigma} \epsilon_{i,\lambda} b_{i,\lambda,\sigma}^\dagger b_{i,\lambda,\sigma} \quad (6.54)$$

$$H_{\text{hyb}} = \sum_{i,\lambda,\sigma} V_{i,\lambda} (f_{K_i,\sigma}^\dagger b_{i,\lambda,\sigma} + h.c.), \quad (6.55)$$

$$\epsilon_{K_i} = \frac{1}{\mathcal{V}(\mathcal{P}_i)} \sum_k \chi_{\mathcal{P}_i}(k) \epsilon_{f,k}. \quad (6.56)$$

The f electron cluster Green's function is given by

$$G_{f,\text{cl}}(K_i, \omega) = [\omega + \mu - E_f - \Delta_f(K_i, \omega) - \Sigma(K_i, \omega)]^{-1}, \quad (6.57)$$

while the d- and f- lattice Green's functions can be expressed as

$$G_{f,\text{latt}}(k, K_i, \omega) = [\omega + \mu - E_f - \epsilon_{k,f} - \Sigma_f(K_i, \omega) - V^2(\omega + \mu - \epsilon_{k,d})^{-1}]^{-1}, \quad (6.58)$$

$$G_{d,\text{latt}}(k, K_i, \omega) = [\omega + \mu - \epsilon_{k,d} - V^2(\omega + \mu - E_f - \epsilon_{k,f} - \Sigma_f(K_i, \omega))^{-1}]^{-1}. \quad (6.59)$$

Self-consistency:

As described in Sec. 3.2, the self-energy $\Sigma_{\text{DCA}}(K_i, \omega)$, calculated from this cluster model, is used as an approximation for the lattice self-energy. The local lattice Green's function is obtained via numeric integration:

$$\mathbf{G}_{\text{latt}}(K_i, \omega) = \int_{\mathcal{P}_i} \frac{dk}{\mathcal{V}(\mathcal{P}_i)} \frac{1}{\mathbf{G}_0^{-1}(k, \omega) - \Sigma_{\text{DCA}}(K_i, \omega)} = \int_{\mathcal{P}_i} \frac{dk}{\mathcal{V}(\mathcal{P}_i)} \mathbf{G}(k, K_i, \omega) \quad (6.60)$$

$$= \int d\epsilon \rho_{K_i}(\epsilon) \mathbf{G}(\epsilon, K_i, \omega), \quad (6.61)$$

in which the momentum space integration is simplified to an integration over the DOS of the corresponding momentum patch denoted by $\rho_{K_i}(\epsilon)$. The self-consistency between lattice and cluster Green's function

$$\mathbf{G}_{\text{latt}}(K_i, \omega) \stackrel{!}{=} \mathbf{G}_{\text{cl}}(K_i, \omega), \quad (6.62)$$

is performed for the previously derived lattice and impurity Green's functions, from which the self-consistent hybridization is extracted each DCA iteration. In case of $t_f = 0$ the d-component of the Green's function is considered and yields the hybridization function:

$$\Delta_d(K_i, \omega) = \omega + \mu - \epsilon_{K_i} - \Sigma_d - (V + \Sigma_{df})(V + \Sigma_{fd})(\omega + \mu - E_f - \Sigma_f)^{-1} - G_{d,\text{latt}}^{-1}(K_i, \omega). \quad (6.63)$$

In contrast, for $U_{df} = 0$, the self-consistency is performed for the f-component of the Green's function and yields the hybridization function:

$$\Delta_f(K_i, \omega) = \omega + \mu - E_f - \epsilon_{K_i} - \Sigma(K_i, \omega) - G_{f,\text{latt}}^{-1}(K_i, \omega). \quad (6.64)$$

Brillouin zone patching:

In our DCA calculations, the Brillouin zone is split into $N_c = 2$ patches, which correspond to the cluster momenta K_i . To obtain the local lattice Green's function $\mathbf{G}_{\text{latt}}(K_i, \omega)$ integrations over each momentum patch are simplified into a DOS integration over the corresponding patch DOS $\rho_{K_i}(\epsilon)$. We have the freedom to choose the shape of the two patches, as long as they split the full BZ equally. We employ a cubic-shaped patch \mathcal{P}_1 , centered around the Γ -point, which we term ‘‘cubic-patching’’. The remainder of the cubic BZ forms the second patch \mathcal{P}_2 , see Fig. 6.14.

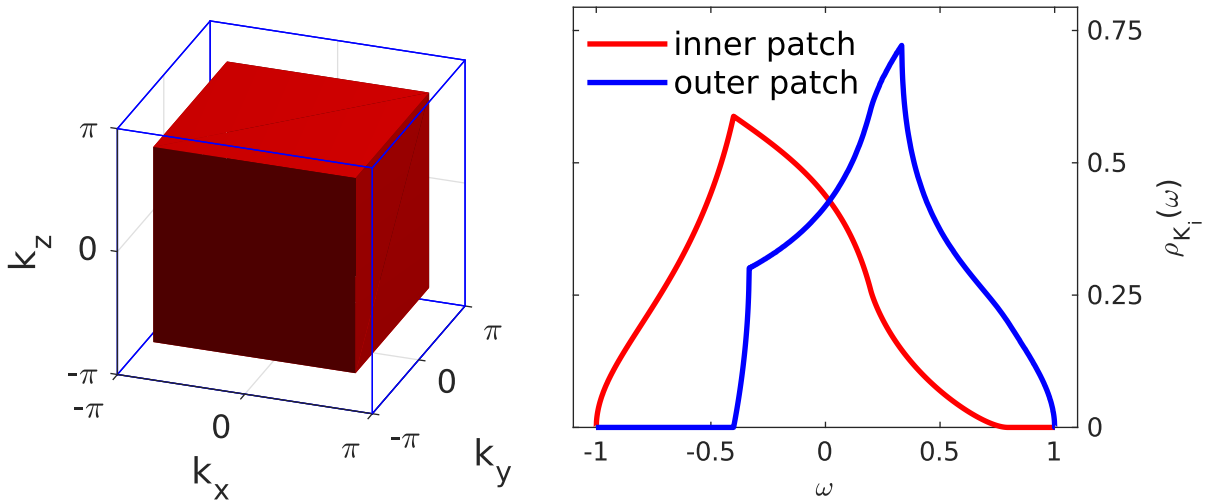


Fig. 6.14: Visualization of the cubic-patching scheme of the sc-BZ (left) and the corresponding patch DOS $\rho_{K_i}(\epsilon)$ of the inner and outer patch (right). Note, the cubic central patch (red) is centered around the Γ -point.

To calculate the patch DOS $\rho_{K_i}(\epsilon)$, the non-interacting Green's function can be numerically integrated over the momentum region of each patch. Because of symmetries, only one octant of the cubic

BZ has to be considered. In the case of cubic-patching, the central cubic patch has an edge length of $2^{2/3}\pi$, s.t. the remainder of the full cubic BZ with edge length 2π has equal volume. The patches can be tiled into rectangular shapes, which makes it possible to calculate each corresponding patch DOS ρ_{K_i} via momentum integration of the non-interacting lattice Green's function:

$$G_i(\omega) = \int_{\mathcal{P}_i} d^3k \frac{1}{\omega - \epsilon_{k,d} + i0^+}. \quad (6.65)$$

Taking spectral part then yields the patch DOS:

$$\rho_{K_i} = -\frac{1}{\pi} \text{Im}[G_i(\omega)]. \quad (6.66)$$

Numerical parameters:

For our NRG calculations, we use $\Lambda = 3$ as the discretization parameter. To reduce the computational cost we use interleaved NRG (iNRG) and keep $N_k = 8000$ multiplets at each truncation step. Standard NRG calculations were performed to verify our iNRG calculations.

6.3.2 Mixed-valence regime, $D_f = 0$

Similar to Sec. 6.2.3 we perform DCA calculations in the mixed-valence (MV) regime and check the influence of the interaction U_{df} , the difference being that we are limited to $D_f = 0$. We keep $U = 10$, $V = 0.4$ fixed and tune $U_{df} \in [0, 1]$. The chemical potential μ and f-level E_f are adjusted with U_{df} , such that $\mu - U_{df} = -0.4$ and $-\mu + E_f = -9.8$. Consequently, the occupation numbers remain in the MV-regime (n_d, n_f) $\approx (0.5, 1.5)$. From the converged DCA result $A_{f/d}(K_i, \omega)$ are obtained. We calculate the local f- and d-spectral function $A_{d/f}(\omega) = \frac{1}{2} \sum_{K_i} A_{d/f}(K_i, \omega)$, displayed in 6.15, to compare the results to our DMFT calculations.

Analogous to the discussion in Sec. 6.2.3, the interaction U_{df} shifts certain excitations like a chemical potential, which results in a shift of the side peaks of the spectral functions. The only difference here is that the spectral functions are gapped around $\omega = 0$ for $U_{df} = 0$. The reason being that $D_f = 0$ is used for the DCA calculations instead of $D_f = 0.2$, which leads to a bandgap, as discussed in Sec. 6.2.2.

Altogether, our DCA calculations reproduce spectral functions calculated via DMFT, i.e. there are no nonlocal correlations within the two-patch cluster. For further evidence, we take a look at the self-energies $\Sigma_{d/f}(K_i, \omega)$ of the different momentum patches. The imaginary parts $\text{Im}[\Sigma_{d/f}(K_i, \omega)]$ are presented in Fig. 6.16. Self-energies of different patches show similar behavior, indicating that no nonlocal correlations are present. The overall behavior is analog to the discussion of self-energies in Sec. 6.2.3. Concluding, our DCA calculations in the case $D_f = 0$, show no signs for nonlocal correlations in the mixed-valence regime. Local spectral functions and self-energies can be reproduced from DMFT calculations.

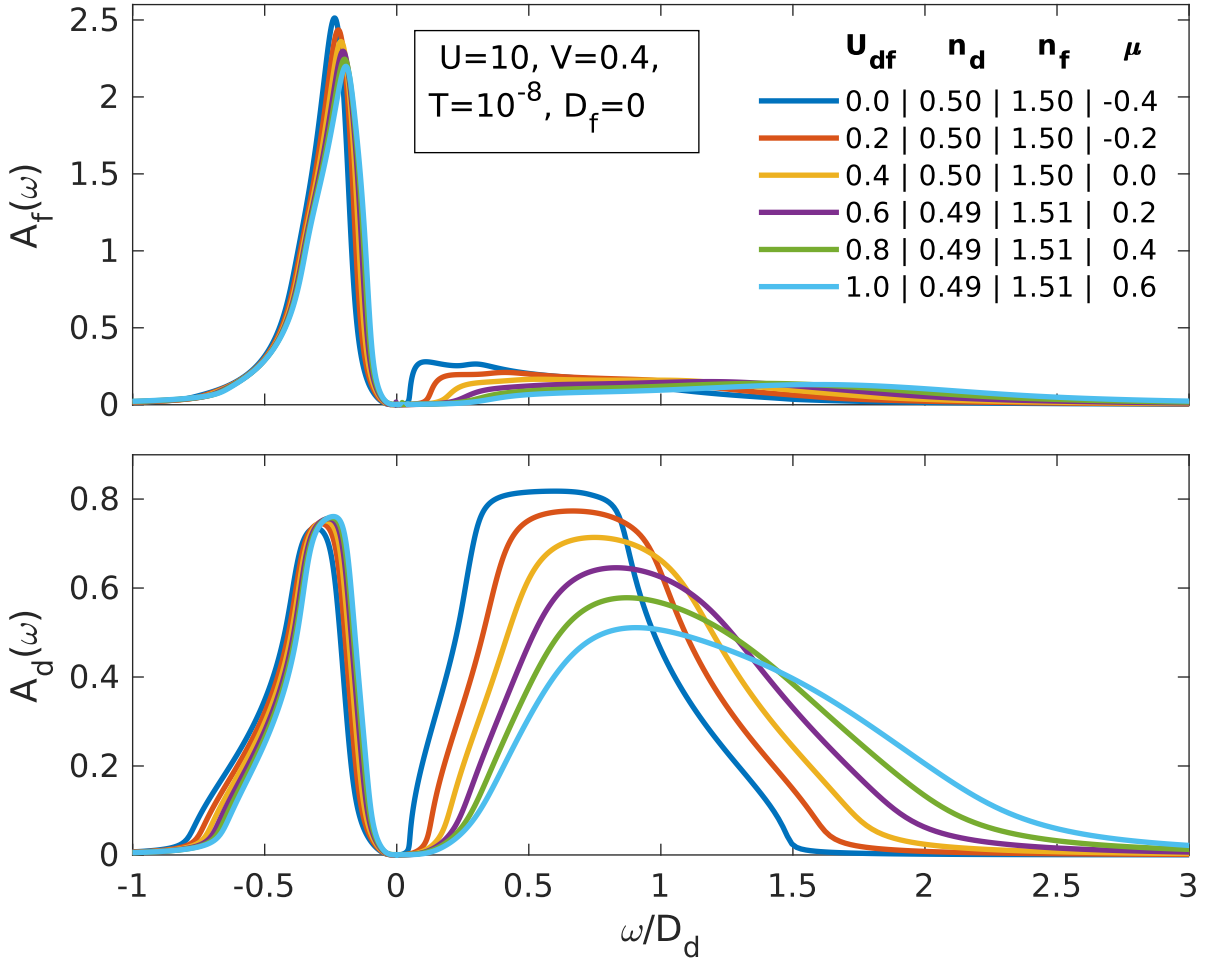


Fig. 6.15: Local spectral functions $A_d(\omega), A_f(\omega)$ for $U_{df} \in [0, 1]$. The remaining parameters are fixed to $U = 10, V = 0.4, D_f = 0, T = 10^{-8}$. In addition, the legend shows the occupancies and that the chemical potential is shifted with U_{df} . Note, we also tune E_f , s.t. $-\mu + E_f = -9.8$ is constant.

6.3.3 Mixed-valence regime, $U_{df} = 0$

DCA calculations are performed for the case $U_{df} = 0$ and finite D_f . The remaining parameters are set to $U = 10, V = 0.4$. As before the chemical potential and f-level are fixed to $\mu = -0.4, E_f = -10.2$, s.t. the mixed valence regime $(n_d, n_f) \approx (0.5, 1.5)$ is reached. Analogous to the case $D_f = 0$ and U_{df} finite, it turns out that the DCA results can be reproduced by single-site DMFT calculations. In Fig. 6.17, a direct comparison between spectral functions obtained via DCA and DMFT is shown for $D_f = 0.2$. The curves of the DMFT and DCA results lie on top of each other, making clear that no nonlocal correlations are present in the mixed-valence regime. Moreover, the self-energies of the two momentum patches coincide as well, which we spare to show.

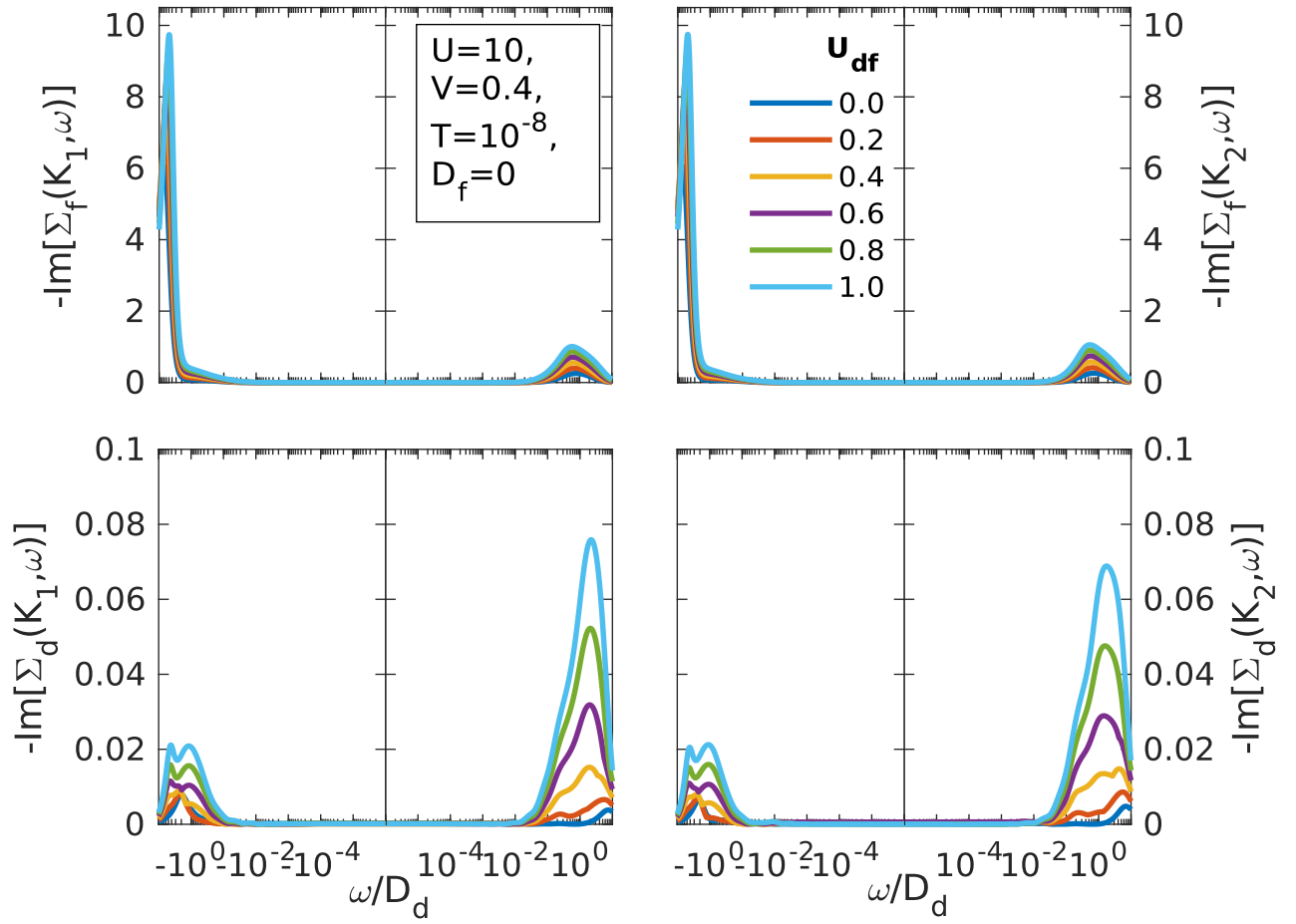


Fig. 6.16: Imaginary parts of the patch self-energies $\Sigma_{d/f}(K_i, \omega)$, corresponding to spectral functions in Fig. 6.15 for $U_{df} \in [0, 1]$. The remaining parameters are fixed to $U = 10, V = 0.4, D_f = 0, T = 10^{-8}$.

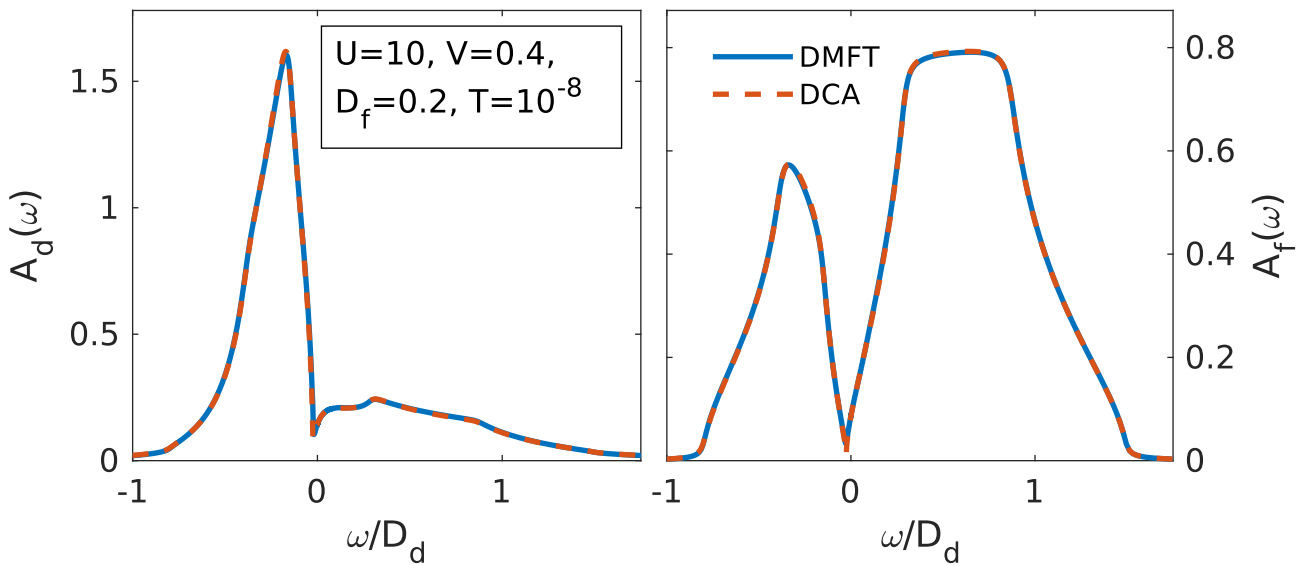


Fig. 6.17: Local spectral functions $A_f(\omega), A_d(\omega)$ obtained from DCA calculations (red) compared to DMFT results (blue).

6.3.4 Away from the mixed-valence regime

Without going into much detail, a phase diagram of the PAM is discussed to give intuition why nonlocal correlations are not present in the mixed-valence regime. The PAM around half-filling ($\langle n_f \rangle = 1$) is known to show competition between the anti-ferromagnetic RKKY [44] interaction and Kondo screening [45]. On the one hand, the non-interacting conduction electrons, here the d electrons, tend to screen the spin of the local f-moments, known as Kondo screening. On the other hand, the anti-ferromagnetic RKKY interaction between different f electrons wants to anti-align the f-moments. The relative strength of the Kondo screening and the RKKY interaction depends on the hybridization strength V . By tuning V the PAM can be tuned through a quantum critical point (QCP).

We calculate the phase diagram of the PAM on a $E_f - \mu$ -grid and fix the remaining parameters to $U = 10, V = 0.4, U_{df} = D_f = 0$. For each data point occupations of d- and f-band are determined. Moreover, we calculate the cumulant $M_f(K_i, \omega) = [\omega + \mu - E_f - \Sigma_f(K_i, \omega)]^{-1}$ for both momentum patches. The cumulant changes sign between the different momentum patches at $\omega = 0$ if nonlocal correlations are present, i.e. $\sigma = M_f(K_2, 0) \cdot M_f(K_1, 0) < 0$. This originates from the different behavior of the self-energy in the RKKY and Kondo regime. In Fig. 6.18 the phase diagram is displayed. Circles indicate phases with $\sigma < 0$, squares regions with $\sigma > 0$. The data point at $\mu = 0.2, E_f = -5.5$, has been studied extensively by Andreas Gleis and can be tuned through a quantum phase transition by tuning V . For $V = 0.4$ the state is dominated by the RKKY interaction, i.e. nonlocal interactions are present. Up to some critical E_f or μ , the RKKY interaction remains dominant, followed by a cross-over to a region dominated by local interactions.

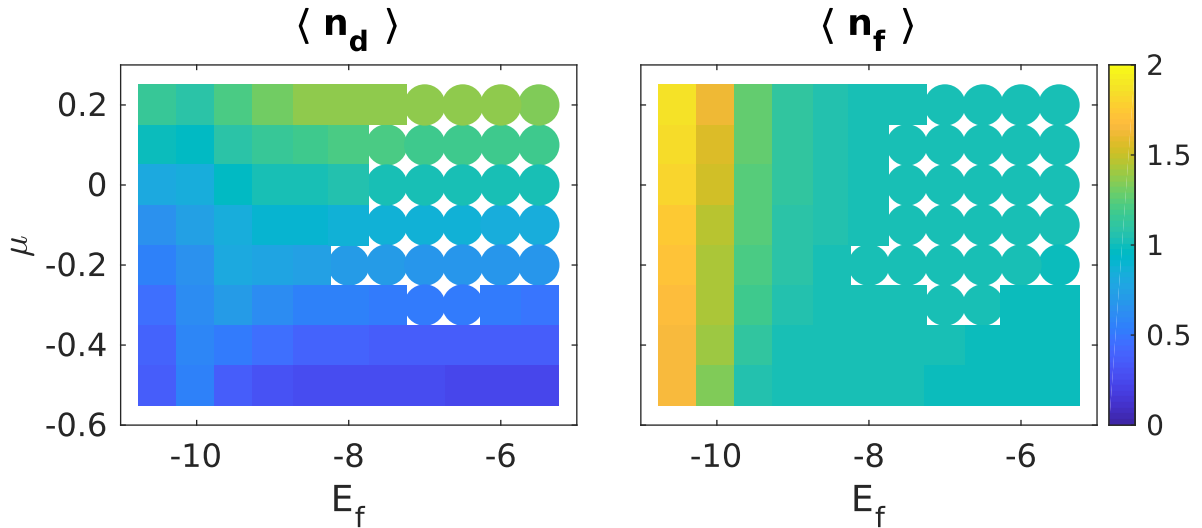


Fig. 6.18: Average occupation of d- and f electrons on a $E_f - \mu$ -grid. Circles indicates states where the cumulant changes sign between the two different momentum patches, i.e. $\sigma = M_f(K_2, 0) \cdot M_f(K_1, 0) < 0$, while squares indicate states with $\sigma > 0$.

Decreasing E_f , a transition to states dominated Kondo screening occurs. Intuitively this can be understood from the low energy limit of the Anderson model, which can be described by a Kondo

model with the anti-ferromagnetic coupling

$$J \propto V^2 \left[\frac{1}{-E_f} + \frac{1}{E_f + U} \right] \quad (6.67)$$

between f- and d electrons, as long as $\langle n_f \rangle = 1$. By decreasing E_f towards $-U$, $\frac{1}{E_f + U}$ increases and J enhances. After the transition, the f electron occupancy starts increasing, by further decreasing E_f .

Reducing μ , which suppresses the d electron occupation, also leads to a transition into a state where local correlations dominate. The RKKY interaction is known to change its sign as the d electron occupancy decreases with μ . Hence, an intuitive explanation might be that f-moments tend to align forming a spin one, which is screened by the conduction electrons.

In the mixed-valence regime, both E_f and μ are reduced. Consequently, nonlocal correlations diminish. Moreover, the f-occupancy $\langle n_f \rangle = 1.5$ is far away from half-filling, meaning that f-moments do not form at every lattice site, making an (anti-)ferromagnetic alignment between neighboring sites impossible. No transition by tuning V can be observed. Larger cluster sizes $N_c > 2$, might show correlations between next-nearest-neighbor f-moments.

6.4 Conclusion

We have studied the extended PAM in the mixed-valence regime with DMFT and DCA. The DMFT calculations show that the non-interacting band structure is renormalized by the interaction U between the f electrons. The additional repulsive interaction U_{df} between d and f electrons shifts certain excitations, similar to a chemical potential, resulting in the formation of the bandgap. Altogether, our DMFT results indicate the picture of a band insulator. Moreover, the calculation of dynamical susceptibilities does not show signs for the formation of “composite excitons” which could form a neutral Fermi surface.

Resistivity calculations show an increasing resistivity with decreasing temperature as the insulating phase is approached, saturating in a plateau. Furthermore, at low temperatures our results indicate a substantial optical conductivity at finite frequencies, much larger than the DC value. In addition a temperature dependent cross-over to a Drude-like response can be seen. Both resistivity and optical conductivity show agreement with experimental measurements on SmB_6 .

The origin of the quantum oscillations(QO) in SmB_6 remains unclear. Possibly, the two-band model does not capture all the essential effects of the full electronic bandstructure of SmB_6 or nonlocal interactions beyond the two-site cluster approximation play an important role. However, it has been pointed out that QO can occur in band insulators with narrow band gaps ([34], [35]), i.e. without the existence of a Fermi surface. In [34] a model of spin-less non-interacting fermions on a two-dimensional cubic lattice, which hybridize with a flat band, are considered. Even, in this simple setting QO in the magnetization are found, if the gap size is of the order of the cyclotron energy and the chemical potential lies close to or within the flat band. The temperature dependence of the QO amplitude shows a maximum at low temperatures, which deviates from the standard Lifshitz-Kosevich behavior. Experiments on SmB_6 [30] do also indicate an anomalous maximum in the oscillation amplitude at low temperatures, however, the magnitude and precise form is not captured by the simple model.

It would be interesting to see if such QO could be seen in the setting of DMFT as the insulating state is approached and how interactions influence them. This could agree with our results, since we

find similarities to experimental results for states which are very close to the metal-insulator transition, i.e. in our case the chemical potential is very close to the lower band or barely lies within it, and the bandgap is narrow. Furthermore, our DCA calculations do not show nonlocal correlations, which supports that the DMFT calculations capture the essential physics.

7 References

- [1] A. Georges, G. Kotliar, W. Krauth, and M. J. Rozenberg, *Rev. Mod. Phys.* **68**, 13 (1996).
- [2] T. Maier, M. Jarrell, T. Pruschke, and M. H. Hettler, *Rev. Mod. Phys.* **77**, 1027 (2005).
- [3] R. Bulla, T. Costi, and T. Pruschke, *Rev. Mod. Phys.* **80**, 395 (2008).
- [4] I. Bloch, J. Dalibard, and S. Nascimbène, *Nature Physics* **8**, 267 (2012).
- [5] D. Chowdhury, I. Sodemann, and T. Senthil, *Nature Communications* **9**, 1766 (2018).
- [6] W. Metzner and D. Vollhardt, *Phys. Rev. Lett.* **62**, 324 (1989).
- [7] P. Coleman, *Introduction to Many-Body Physics* (Cambridge University Press, Cambridge, 2015), Vol. 1, p. 234.
- [8] J. M. Luttinger and J. C. Ward, *Phys. Rev.* **118**, 1417 (1960).
- [9] G. Baym and L. P. Kadanoff, *Phys. Rev.* **123**, 287 (1961).
- [10] G. Biroli, O. Parcollet, and G. Kotliar, *Phys. Rev. B* **69**, 205108 (2004).
- [11] G. Biroli and G. Kotliar, *Phys. Rev. B* **65**, 155112 (2002).
- [12] T. D. Stanescu, M. Civelli, K. Haule, and G. Kotliar, *Annals of Physics* **321**, 1682 (2006).
- [13] T. D. Stanescu and G. Kotliar, *Phys. Rev. B* **74**, 125110 (2006).
- [14] K. G. Wilson, *Rev. Mod. Phys.* **47**, 773 (1975).
- [15] A. Weichselbaum, *Annals of Physics* **327**, 2972 (2012).
- [16] F. Anders and A. Schiller, *Phys. Rev. Lett.* **95**, 196801 (2005).
- [17] A. Weichselbaum and J. von Delft, *Phys. Rev. Lett.* **99**, 076402 (2007).
- [18] A. K. Mitchell *et al.*, *Phys. Rev. B* **89**, 121105 (2014).
- [19] K. M. Stadler, A. K. Mitchell, J. von Delft, and A. Weichselbaum, *Phys. Rev. B* **93**, 235101 (2016).
- [20] L. Riegger *et al.*, *Phys. Rev. Lett.* **120**, 143601 (2018).
- [21] H. C. Longuet-Higgins and M. D. Roberts, *Proceedings of the royal society of London Series A* **224**, 336 (1954).
- [22] M. Mizumaki, S. Tsutsui, and F. Iga, *J.Phys.: Conf. Series* **176**, 012034 (2009).
- [23] J. C. Nickerson *et al.*, *Phys. Rev. B* **3**, 2032 (1971).
- [24] B. Gorshunov *et al.*, *Phys. Rev. B* **59**, 1808 (1999).
- [25] N. J. Laurita *et al.*, *Phys. Rev. B* **94**, 165154 (2016).

-
- [26] N. F. Mott, *Phil. Mag.* **30**, 403 (1974).
- [27] R. M. Martin and J. W. Allen, *J. Appl. Phys.* **50**, 7561 (1979).
- [28] M. Dzero, K. Sun, V. Galitski, and P. Coleman, *Phys. Rev. Lett.* **104**, 106408 (2010).
- [29] D. J. Kim *et al.*, *Scientific reports* **3**, 3150 (2013).
- [30] B. S. Tan *et al.*, *Science* **349**, 287 (2015).
- [31] M. Hartstein *et al.*, *Nat. Phys.* **14**, 166 (2018).
- [32] I. Lifshitz and A. Kosevich, *JETP* **2**, 636 (1956).
- [33] P. F. S. Rosa and Z. Fisk, arXiv:2007.09137 [cond-mat.str-el] (2020).
- [34] J. Knolle and N. R. Cooper, *Phys. Rev. Lett.* **115**, 146401 (2015).
- [35] L. Zhang, X.-Y. Song, and F. Wang, *Phys. Rev. Lett.* **116**, 046404 (2016).
- [36] M. S. et al, *Phys. Rev. Lett.* **120**, 016402 (2018).
- [37] O. Jepsen and O. K. Anderson, *Solid State Communications* **9**, 1763 (1971).
- [38] G. Lehmann and M. Taut, *Phys. Stat. Sol.* **54**, 469 (1972).
- [39] P. E. Blöchl, O. Jepsen, and O. K. Andersen, *Phys. Rev. B* **49**, 16223 (1994).
- [40] A. C. Hewson, *Phys. Rev. Lett.* **70**, 4007 (1993).
- [41] A. C. Hewson, A. Oguri, and D. Meyer, *Eur. Phys. J. B* **40**, 177 (2004).
- [42] P. Voruganti, A. Golubentsev, , and S. John, *Phys. Rev. B* **45**, 13945 (1992).
- [43] E. Lange and G. Kotliar, *Phys. Rev. B* **59**, 1800 (1999).
- [44] M. A. Ruderman and C. Kittel, *Phys. Rev.* **96**, 99 (1954).
- [45] S. Doniach, *Physica B+C* **91**, 231 (1977).